

Title	Simple solvothermal synthetic approach to mixed metaloxide nanoassemblies with controlled atomic compositions, nano-structures, and morphologies
Author(s)	ELLAWALA KANKANAMGE, Chandima Pradeep
Citation	高知工科大学, 博士論文.
Date of issue	2016-03
URL	<a href="http://hdl.handle.net/10173/1383">http://hdl.handle.net/10173/1383</a>
Rights	
Text version	ETD



Kochi, JAPAN

<http://kutarr.lib.kochi-tech.ac.jp/dspace/>

# **Simple Solvothermal Synthetic Approach to Mixed Metal Oxide Nanoassemblies with Controlled Atomic Compositions, Nano-structures, and Morphologies**

Ellawala Kankanamge Chandima Pradeep

A dissertation submitted to  
Kochi University of Technology  
in partial fulfillment of the requirements  
for the degree of  
Doctor of Philosophy

Graduate School of Engineering  
Kochi University of Technology  
Kochi, Japan  
March, 2016

## TABLE OF CONTENTS

<b>Chapter 1.</b>		1
<b>General introduction</b>		
<b>1-1</b>	<b>Porous metal oxide nanomaterials</b>	1
<b>1-2</b>	<b>Synthesis of porous nanomaterials</b>	2
1-1-1	Precipitation method	2
1-1-2	Sol-gel method	3
1-1-3	Electrodeposition	3
1-1-4	Solvothermal method	4
<b>1-3</b>	<b>Frontiers of solvothermal methods in the field metal oxide nanomaterial synthesis</b>	6
1-3-1	Mixed metal oxide composite nanoassemblies	6
1-3-2	MgO ultra-fine nanocrystals	7
<b>1-4</b>	<b>Development of synthetic methods for mixed metal oxide composite nanoassemblies and MgO ultra-fine nanocrystals</b>	7
<b>Chapter 2.</b>		14
<b>A simple solvothermal approach to Al<sub>2</sub>O<sub>3</sub>-TiO<sub>2</sub> and ZnO-TiO<sub>2</sub> mesoporous hollow spherical composite nanoassemblies consisting of Al<sub>2</sub>O<sub>3</sub> or ZnO fine primary nanoparticles mixed with TiO<sub>2</sub> domains</b>		
<b>2-1</b>	<b>Introduction</b>	14
<b>2-2</b>	<b>Results and discussion</b>	17
2-2-1	Heat tolerance of hollow Al <sub>2</sub> O <sub>3</sub> -TiO <sub>2</sub> composite nanoassemblies	29
2-2-2	Band gap tuning of hollow ZnO-TiO <sub>2</sub> composite nanoassemblies	32
2-2-3	Chemical etching of hollow spherical composite nanoassemblies	34
<b>2-3</b>	<b>Conclusions</b>	34
<b>2-4</b>	<b>Experimental Section</b>	35
2-4-1	General information	35
2-4-2	Synthesis of Al <sub>2</sub> O <sub>3</sub> -TiO <sub>2</sub> and ZnO-TiO <sub>2</sub> hollow composite nanoassemblies	36
2-4-3	Calcination of hollow composite nanoassemblies	36
2-4-4	Chemical etching of hollow composite nanoassemblies	36
2-4-5	Characterization	36

<b>Chapter 3.</b>		42
<b>Ultra-simple synthetic approach to the fabrication of CeO<sub>2</sub>-ZrO<sub>2</sub> mixed nanoassemblies into homogeneous, domain, and core-shell structures in mesoporous spherical morphologies using high-temperature and high-pressure alcohols</b>		
<b>3-1</b>	<b>Introduction</b>	42
<b>3-2</b>	<b>Results and discussion</b>	43
3-2-1	Single-step one-pot synthesis of homogeneously well dispersed mesoporous spherical Ce <sub>x</sub> Zr <sub>1-x</sub> O <sub>2</sub> composite nanoassemblies and mesoporous spherical CeO <sub>2</sub> -ZrO <sub>2</sub> composite nanoassemblies with domain structures	43
3-2-2	Synthesis of ZrO <sub>2</sub> @CeO <sub>2</sub> core-shell nanoassemblies by a step-wise approach in high-temperature and high-pressure alcohols	55
<b>3-3</b>	<b>Conclusions</b>	59
<b>3-4</b>	<b>Experimental Section</b>	60
3-4-1	General information	60
3-4-2	Synthesis of mesoporous spherical composite nanoassemblies	60
3-4-3	Characterization	61
<b>Chapter 4.</b>		
<b>Synthesis of MgO ultra-fine nanocrystals by single-step solvothermal method</b>		65
<b>4-1</b>	<b>Introduction</b>	65
<b>4-2</b>	<b>Results and discussion</b>	67
<b>4-3</b>	<b>Conclusions</b>	71
<b>4-4</b>	<b>Experimental Section</b>	72
4-4-1	General information	72
4-4-2	Synthesis of MgO nanocrystals and nanoassemblies	72
4-4-3	Characterization	73
<b>Chapter 5.</b>		76
<b>Conclusions</b>		

# Chapter 1.

## General introduction

### 1-1 Porous metal oxides nanomaterials

Nanomaterials whose particle sizes are less than 100 nm show quite different chemical, physical, electronic, and magnetic properties as compared to those of corresponding bulk materials,<sup>[1]</sup> since these nano-scale particles obey the laws of quantum mechanics<sup>[2]</sup> and have huge surface area originated from their small particle size concomitant with numerous specific points, such as terraces, edges, and corners, where the atoms have lower coordination numbers and different bonding structures.<sup>[1]</sup> Much effort has been paid to utilize these unique properties of nanomaterials in many research and industrial fields.<sup>[3-8]</sup>

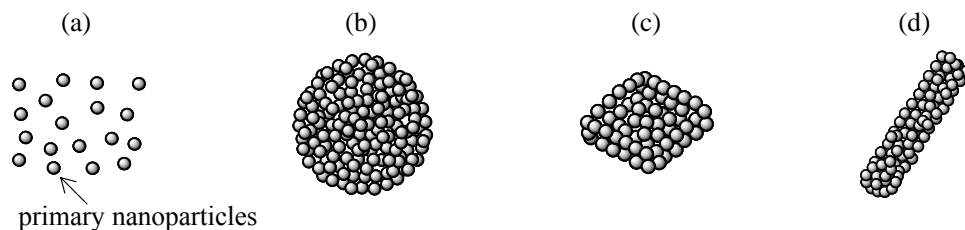


**Figure 1-1.** Schematic illustrations of (a) monodispersed nanoparticles, (b) porous spherical nanoassemblies, (c) porous nanosheets, and (d) porous nanorods.

Among many nanomaterials, metal oxides play important roles in many fields, for instance, physics, chemistry, materials science, and biology, due to their semi-conductive behaviors and catalytic activities as well as their stabilities, easiness of handling, and costs.<sup>[9,10]</sup> Large number of researches on synthesis, characterization, and application of the nanomaterials have been reported in last few decades.<sup>[11]</sup> Many kinds of metal oxide nanomaterials such as monodispersed nanoparticles, nanoassemblies with ordered secondary morphology (Figure 1-1), and thin films deposited on the substrates are widely studied.<sup>[12]</sup>

Metal oxide nanomaterials with porous ordered secondary morphology for example, sphere,<sup>[13]</sup> cube,<sup>[14]</sup> rod, tube,<sup>[15]</sup> sheet,<sup>[16]</sup> and thin film<sup>[17]</sup> also have been received much attention due to their possible applications in many fields, such as energy storage, drug delivery, catalysts, photocatalysts, catalyst supports, surface lapping and polishing materials, adsorbents, heat insulators, and material storage, due to their large surface area, rough surface, well defined pore topology, large void volume, etc.<sup>[3,12,18-20]</sup> The average size of the pores of nanomaterials, which controls the chemical, physical, and electronic properties of these porous nanomaterials, is directly proportional to the sizes of the primary nanoparticles.<sup>[2]</sup> The surface roughness, pore size distribution, and the surface area of the porous nanomaterials can be tuned by controlling the size of primary nanoparticles. Thus, in order to achieve high-performance, control of primary particle size is one of the most important factors for the nanomaterials with porous higher-ordered secondary morphology.

## **1-2 Synthesis of porous nanomaterials**

Among the various synthetic methods for the porous nanomaterials, chemical approaches, such as precipitation, sol-gel, microemulsion, electrodeposition, and solvothermal methods, have received much attention because of their simplicity, low cost, ability to make new materials from the precursors, ability of functionalization, etc.<sup>[21,22]</sup> Some of representatives are introduced below.

### **1-2-1 Precipitation method**

Precipitation method is one of the simplest techniques to obtain metal oxide nanomaterials. Usually the precipitation method is carried out by mixing a solution containing metal precursors with another solution or by slow evaporation of the solvent to produce insoluble or slightly soluble products. Some of the metal oxide nanomaterials can be

directly prepared by the precipitation, while long reaction time, multi-steps reactions including calcination, and usage of surfactants are usually required (Figure 1-2).

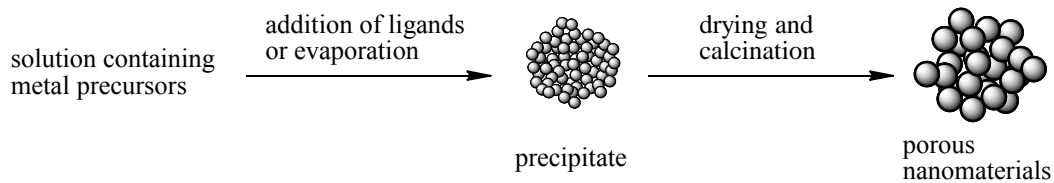


**Figure 1-2.** Schematic illustration of the synthesis of nanomaterials by precipitation method.

### 1-2-2 Sol-gel method

Sol-gel method is one of the most widely used methods.<sup>[22]</sup> Typically, metal alkoxides or metal salts are hydrolyzed to yield well dispersed fine particles called “sol” followed by the condensation process to obtain cross-linked network of partials called “gel”.<sup>[23]</sup> The gel is usually aged for several hours to several days and dried to afford desired porous nanomaterials.<sup>[23,24]</sup> Crystalline porous nanomaterials are obtained by further calcination of the obtained gels.<sup>[25]</sup> However, the calcination at high temperature sometimes leads to decrease the surface area of the nanomaterials due to the heat induced enlargement of the primary nanoparticles (Figure 1-3).

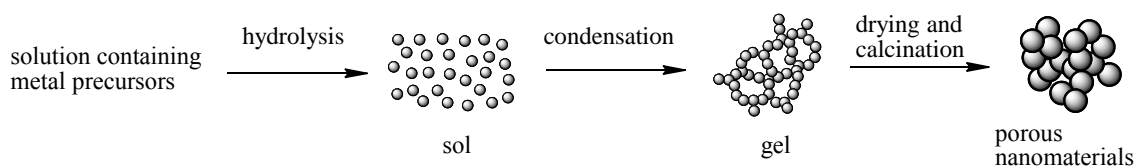


**Figure 1-3.** Schematic illustration of the synthesis of nanomaterials by sol-gel method.

### 1-2-3 Electrodeposition

Electrodeposition is known as a simple and low-cost method for the synthesis of nanomaterials.<sup>[26]</sup> In this method, the chemical species which required for the growth of the

nanomaterials are electrochemically generated by reduction or oxidation of precursors.<sup>[27]</sup> The electrodeposition method is applicable not only for the deposition of noble metal nanomaterials but also for the synthesis of metal oxide nanomaterials.<sup>[27–29]</sup> However, this method is limited for the conductive substrates.

#### 1-2-4 Solvothermal method

Solvothermal method including hydrothermal method is one of the most powerful and widely used methods to synthesize nanomaterials because of the advantages such as high reproducibility, simple procedure, and the easy scale-up, in which precursor solutions are treated in a closed reaction vessel at a high temperature being higher than the boiling point of the solvent.<sup>[30]</sup> Mass production of the nanomaterials can be possible through continuous reactors. However, the solvothermal methods generally require long reaction time ranging from several hours to days. Therefore, the development of simple and rapid synthetic approaches to afford metal oxide nanoassemblies remains important.

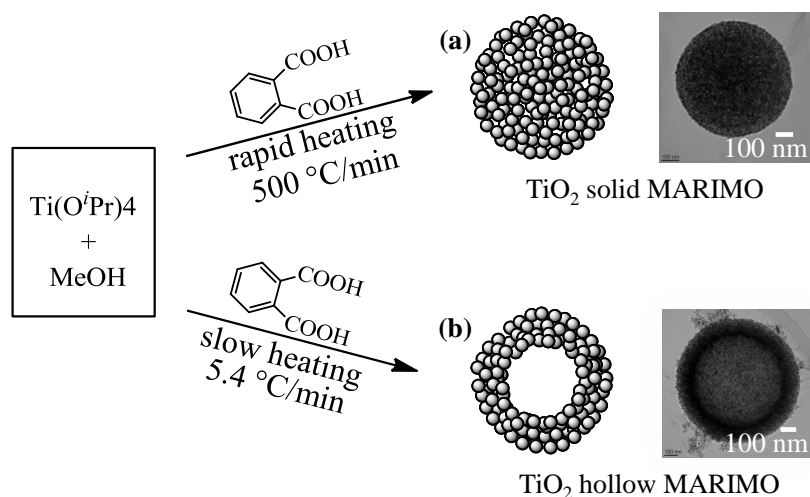


**Figure 1-4.** Schematic illustration of the synthesis of TiO<sub>2</sub> (a) solid MARIMO and (b) hollow MARIMO nanoassemblies.

To this end, Wang et al. developed a template-free, single-step, and one-pot synthetic method to obtain TiO<sub>2</sub> porous spherical nanomaterials.<sup>[31]</sup> The obtained spherical nanoassemblies were named as **mesoporously architected roundly integrated metal oxide** (MARIMO) due to their similarity in shape of *marimo* (*cladophora aegagropila*) moss balls, where numerous fine primary nanoparticles aggregate each other to form a porous spherical secondary structure. The single-step one-pot synthesis of TiO<sub>2</sub> MARIMO nanoassemblies was achieved by heating of a precursor solution containing titanium isopropoxide (Ti(O<sup>i</sup>Pr)<sub>4</sub>) and phthalic acid in methanol at an elevated temperature (300 °C).<sup>[31]</sup> In this solvothermal method, organic acid, heating rate, and reaction temperature are the critical factors controlling the morphologies of obtained MARIMO nanoassemblies (Figure 1-4). Rapid heating (500 °C/min) of the precursor solution containing Ti(O<sup>i</sup>Pr)<sub>4</sub> and phthalic acid in methanol afforded TiO<sub>2</sub> solid MARIMO nanoassemblies with individual spherical morphology (Figure 1-4a), while slow heating (5.4 °C/min) of the precursor solution resulted in TiO<sub>2</sub> hollow MARIMO nanoassemblies (Figure 1-4b). MARIMO nanoassembly families such as SiO<sub>2</sub>, ZnO, ZrO<sub>2</sub>, and CeO<sub>2</sub> were also synthesized by the similar solvothermal treatments of appropriate precursor solutions (Figure 1-5).

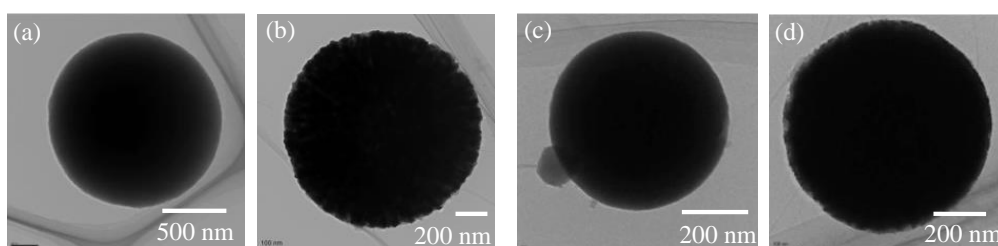


**Figure 1-5.** TEM images of (a) SiO<sub>2</sub>, (b) ZnO, (c) ZrO<sub>2</sub>, and (d) CeO<sub>2</sub> solid MARIMO nanoassemblies.

### **1-3 Frontiers of solvothermal methods in the field of metal oxide nanomaterial synthesis**

Solvothermal methods are ubiquitous approaches in the field of metal oxide nanomaterial synthesis. Simple solvothermal synthesis of SiO<sub>2</sub>, TiO<sub>2</sub>, Fe<sub>2</sub>O<sub>3</sub>, WO<sub>3</sub>, ZnO, ZrO<sub>2</sub>, CeO<sub>2</sub>, etc. nanomaterials with different morphologies has been demonstrated.<sup>[31-34]</sup> However, simple solvothermal synthesis of mixed metal oxide nanomaterials has not been widely studied. On the other hand, some of metal oxide nanomaterials are difficult to obtain by solvothermal methods. For example, solvothermal synthesis of MgO nanomaterials has not yet been reported in literature, to the best of my knowledge. To this end, the simple solvothermal method developed by Wang et al. exhibited high potential to conquer these frontiers in the field of metal oxide nanomaterial synthesis. Importance of mixed metal oxide composite nanoassemblies and MgO ultra-fine nanocrystals as well as their synthesis are briefly introduced below.

#### **1-3-1 Mixed metal oxide composite nanoassemblies**

Mixed metal oxide composite nanoassemblies have received much attention due to their enhanced physical, chemical, electronic, and magnetic properties as compared to those of single component metal oxides, since the properties of metal oxide nanoassemblies can be enhanced by mixing several metal oxides in nanoscale.<sup>[35-37]</sup> In addition, nano-structure of the composite nanoassemblies, for example homogeneous, domain, and layer, is critical to their properties, such as size of the primary nanoparticles, specific surface area, heat tolerance of the crystalline phase, band gap energy, and electric conductivity.<sup>[38-42]</sup> In order to control nano-structure of the composite nanoassemblies, several synthetic methods have been developed.<sup>[43-47]</sup> Solid state preparation methods of composite metal oxides, such as high-energy mechanical mixing and high temperature reactions, are the conventional methods, but they take relatively long reaction time and sometimes they lead to reduce their surface

area.<sup>[43,44]</sup> Instead, much attention has been paid to the synthesis of mixed metal oxide composite nanomaterials by liquid phase chemical reactions. The chemical methods such as precipitation, sol-gel, electrospinning, or calcination of metal organic frameworks are currently used to obtain mixed metal oxide composite nanoassemblies.<sup>[48-50]</sup> However, these methods also require long reaction time and multi-step reactions to obtain the products. In order to overcome this issue, I developed a simple solvothermal approach to obtain mixed metal oxide composite nanoassemblies.

### **1-3-2 MgO ultra-fine nanocrystals**

MgO ultra-fine nanocrystals are supposed to have much wide band gap energy due to the quantum confinement effect derived from ultra-fine nanosize. MgO nanomaterials are typically synthesized by calcination of solid intermediates such as Mg(OH)<sub>2</sub>, MgCO<sub>3</sub>, and Mg containing metal organic frameworks (MOFs).<sup>[51-53]</sup> However, the calcination at high temperature usually results in increase of the size of metal oxide primary nanoparticles, due to the heat induced crystal growth.<sup>[54]</sup> In order to overcome this issue, I developed a simple solvothermal synthetic approach to MgO ultra-fine nanocrystals by changing Mg salt, organic additive, solvent, and reaction temperature.

## **1-4 Development of synthetic methods for mixed metal oxide composite nanoassemblies and MgO ultra-fine nanocrystals**

In order to obtain mixed metal oxide composite nanoassemblies, I applied Wang's ultimately simple solvothermal procedure treating precursor solutions of metal salts and alkoxides. The details of my researches to synthesize mixed metal oxide composite nanoassemblies are described in chapter 2 and chapter 3. Chapter 2 deals with the development of a new synthetic method to obtain hollow spherical Al<sub>2</sub>O<sub>3</sub>-TiO<sub>2</sub> and ZnO-TiO<sub>2</sub> composite nanoassemblies to enhance thermal stability of anatase phase of TiO<sub>2</sub> and

fine-tuning of TiO<sub>2</sub> band gap energy by mixing TiO<sub>2</sub> with Al<sub>2</sub>O<sub>3</sub> and ZnO in nanolevel, respectively. Synthesis of spherical CeO<sub>2</sub>-ZrO<sub>2</sub> composite nanoassemblies with different arrangements of primary nanoparticles such as homogeneous, domain, and core-shell morphologies is discussed in Chapter 3. The details of my research to synthesize MgO ultra-fine nanocrystals are described in chapter 4. In order to obtain MgO ultra-fine nanocrystals, I applied high-temperature and high-pressure solvothermal method. Solvothermal synthesis of MgO(OH)<sub>2</sub> flower shape nanoassemblies, Mg(OH)<sub>2</sub> nanosheets, and amorphous hollow spherical nanoassemblies consisting of Mg and O atoms is also described in Chapter 4.

## References

1. W. J. Huang, R. Sun, J. Tao, L. D. Menard, R. G. Nuzzo, J. M. Zuo, Coordination-dependent surface atomic contraction in nanocrystals revealed by coherent diffraction, *Nature Materials* **2008**, *7*, 308–313.
2. R. Koole, E. Groeneveld, D. Vanmaekelbergh, A. Meijerink, C. de M. Donegá, Nanoparticles, ed. C. de M. Donegá Springer-Verlag Heidelberg, **2014**, 13–51.
3. L. F. Deravi, J. D. Swartz, D. W. Wright, Nanomaterials for the Life Sciences Vol. 2: Nanostructured Oxides, ed. C. S. S. R. Kumar, WILEY-VCH Verlag GmbH & Co. KGaA, Weinheim, **2009**, 3–21.
4. O. V. Salata, Applications of nanoparticles in biology and medicine, *J. Nanobiotechnol.* **2004**, *2*, 3.
5. I. M. Hamouda, Current perspectives of nanoparticles in medical and dental biomaterials, *J. Biomed. Res.* **2012**, *26*, 143–151.
6. D. T. Gillaspie, R. C. Tenent, A. C. Dillon, Metal-oxide films for electrochromic applications: present technology and future directions, *J. Mater. Chem.* **2010**, *20*, 9585–9592.
7. S. Lwin, I. E. Wachs, Olefin metathesis by supported metal oxide catalysts, *ACS Catal.* **2014**, *4*, 2505–2520.

8. M. M. Khin, A. S. Nair, V. J. Babu, R. Murugana, S. Ramakrishna, A review on nanomaterials for environmental remediation, *Energy Environ. Sci.* **2012**, *5*, 8075–8109.
9. M. F.-García, A. M.-Arias, J. C. Hanson, J. A. Rodriguez, Nanostructured oxides in chemistry: characterization and properties, *Chem. Rev.* **2004**, *104*, 4063–4104.
10. E. Roduner, Size matters: why nanomaterials are different, *Chem. Soc. Rev.* **2006**, *35*, 583–592.
11. M. C. Roco, The long view of nanotechnology development: the national nanotechnology initiative at 10 years, *J. Nanopart. Res.* **2011**, *13*, 427–445.
12. G. R. Patzke, Y. Zhou, R. Kotic, F. Conrad, Oxide nanomaterials: synthetic developments, mechanistic studies, and technological innovations, *Angew. Chem. Int. Ed.* **2011**, *50*, 826–859.
13. S. Y. Ho, A. S. W. Wong, G. W. Ho, Controllable porosity of monodispersed tin oxide nanospheres via an additive-free chemical route, *Cryst. Growth Des.* **2009**, *9*, 732–736.
14. V. Amoli, S. Bhat, A. Maurya, B. Banerjee, A. Bhaumik, A. K. Sinha, Tailored synthesis of porous TiO<sub>2</sub> nanocubes and nanoparallelepipeds with exposed {111} facets and mesoscopic void space: a superior candidate for efficient dye-sensitized solar cells, *ACS Appl. Mater. Interfaces* **2015**, *7*, 26022–26035.
15. Z. Zhang, J. Hao, W. Yang, B. Lu, X. Ke, B. Zhang, J. Tang, Porous Co<sub>3</sub>O<sub>4</sub> nanorods–reduced graphene oxide with intrinsic peroxidase-like activity and catalysis in the degradation of methylene blue, *ACS Appl. Mater. Interfaces* **2013**, *5*, 3809–3815.
16. J. Wang, A.-H. Lu, M. Li, W. Zhang, Y.-S. Chen, D.-X. Tian, W.-C. Li, Thin porous alumina sheets as supports for stabilizing gold nanoparticles, *ACS Nano* **2013**, *7*, 4902–4910.
17. S. Ding, Z. Liu, D. Li, W. Zhao, Y. Wang, D. Wan, F. Huang, Tunable assembly of vanadium dioxide nanoparticles to create porous film for energy-saving applications, *ACS Appl. Mater. Interfaces* **2013**, *5*, 1630–1635.

18. G. Zu, J. Shen, W. Wang, L. Zou, Y. Lian, Z. Zhang, B. Liu, F. Zhang, Robust, highly thermally stable, core–Shell nanostructured metal oxide aerogels as high-temperature thermal superinsulators, adsorbents, and catalysts, *Chem. Mater.* **2014**, *26*, 5761–5772.
19. U. V. Desai, C. Xu, J. Wu, D. Gao, Hybrid TiO<sub>2</sub>–SnO<sub>2</sub> nanotube arrays for dye-sensitized solar cells, *J. Phys. Chem. C* **2013**, *117*, 3232–3239.
20. Z. Wang, L. Zhou, X. W. Lou, Metal oxide hollow nanostructures for lithium-ion batteries, *Adv. Mater.* **2012**, *24*, 1903–1911.
21. G. M. Whitesides, Nanoscience, nanotechnology, and chemistry, *Small* **2005**, *1*, 172–179.
22. B. L. Cushing, V. L. Kolesnichenko, C. J. O’Connor, Recent advances in the liquid-phase syntheses of inorganic nanoparticles, *Chem. Rev.* **2004**, *104*, 3893–3946.
23. M. Niederberger, Nonaqueous sol–gel routes to metal oxide nanoparticles, *Acc. Chem. Res.* **2007**, *40*, 793–800.
24. T. K. Tseng, Y. S. Lin, Y. J. Chen, H. Chu, A review of photocatalysts prepared by sol-gel method for VOCs removal, *Int. J. Mol. Sci.* **2010**, *11*, 2336–2361.
25. C. Suci, A. C. Hoffmann, A. Vik, F. Goga, Effect of calcination conditions and precursor proportions on the properties of YSZ nanoparticles obtained by modified sol–gel route, *Chem. Eng. J.* **2008**, *138*, 608–615.
26. W.-Y. Ko, W.-H. Chen, C.-Y. Cheng, K.-J. Lin, Architectural growth of Cu nanoparticles through electrodeposition, *Nanoscale Res. Lett.* **2009**, *4*, 1481–1485.
27. J. Lee, Y. Tak, Electrodeposition of ZnO on ITO electrode by potential modulation method, *Electrochem. Solid-State Lett.* **2001**, *9*, C63–C65.
28. K. Wessels, M. Maekawa, J. Rathousky, T. Oekermann, One-step electrodeposition of TiO<sub>2</sub>/dye hybrid films, *Thin Solid Films* **2007**, *515*, 6497–6500.
29. A. C. Cruickshank, S. E. R. Tay, B. N. Illy, R. D. Campo, S. Schumann, T. S. Jones, S. Heutz, M. A. McLachlan, D. W. McComb, D. J. Riley, M. P. Ryan, Electrodeposition of ZnO nanostructures on molecular thin films, *Chem. Mater.* **2011**, *23*, 3863–3870.

30. G. Demazea, Solvothermal Processes: Definition, key factors governing the involved chemical reactions and new trends, *Z. Naturforsch. B* **2010**, *65*, 999–1006.
31. P. Wang, K. Kobiro, Ultimately simple one-pot synthesis of spherical mesoporous TiO<sub>2</sub> nanoparticles in supercritical methanol, *Chem. Lett.* **2012**, *41*, 264–266.
32. J. Lu, X. Jiao, D. Chen, W. Li, Solvothermal Synthesis and Characterization of Fe<sub>3</sub>O<sub>4</sub> and  $\gamma$ -Fe<sub>2</sub>O<sub>3</sub> Nanoplates, *J. Phys. Chem. C* **2009**, *113*, 4012–4017.
33. J. Ma, J. Zhang, S. Wang, T. Wang, J. Lian, X. Duan, W. Zheng, Topochemical preparation of WO<sub>3</sub> nanoplates through precursor H<sub>2</sub>WO<sub>4</sub> and their gas-sensing performances, *J. Phys. Chem. C* **2011**, *115*, 18157–18163.
34. C. Aymonier, A. L. Serani, H. Reveron, Y. Garrabos, F. Cansell, Review of supercritical fluids in inorganic materials science, *J. Supercrit Fluids* **2006**, *38*, 242–251.
35. M. B. Gawande, R. K. Pandey, R. V. Jayaram, Role of mixed metal oxides in catalysis science—versatile applications in organic synthesis, *Catal. Sci. Technol.* **2012**, *2*, 1113–1125.
36. C. Yuan, H. B. Wu, Y. Xie, X. W. Lou, Mixed transition-metal oxides: design, synthesis, and energy-related applications, *Angew. Chem. Int. Ed.* **2014**, *53*, 1488–1504.
37. I. E. Wachs, K. Routray, Catalysis science of bulk mixed oxides, *ACS Catal.* **2012**, *2*, 1235–1246.
38. S. Guo, H. Yoshioka, H. Kakehi, Y. Kato, M. Miura, N. Isu, B. Ameduri, H. Sawada, Fluoroalkyl end-capped vinyltrimethoxysilane oligomer/anatase titanium oxide nanocomposites possessing photocatalytic activity even after calcination at 1000 °C, *J. Colloid Interface Sci.* **2012**, *387*, 141–145.
39. J. Yang, J. M. F. Ferreira, Inhibitory effect of the Al<sub>2</sub>O<sub>3</sub>–SiO<sub>2</sub> mixed additives on the anatase–rutile phase transformation, *Mater. Lett.* **1998**, *36*, 320–324.
40. J. Wang, H. Sun, J. Huang, Q. Li, J. Yang, Band structure tuning of TiO<sub>2</sub> for enhanced photoelectrochemical water splitting, *J. Phys. Chem. C* **2014**, *118*, 7451–7457.

41. R. D. Monte, J. Kaspar, Nanostructured CeO<sub>2</sub>-ZrO<sub>2</sub> mixed oxides, *J. Mater. Chem.* **2005**, *15*, 633–648.
42. V. Bhosle, A. Tiwari, J. Narayan, Electrical properties of transparent and conducting Ga doped ZnO, *J. Appl. Phys.* **2006**, *100*, 033713.
43. C. Leitenburg, A. Trovarelli, F. Zamar, S. Maschio, G. Dolcetti, J. Liorca, A novel and simple route to catalysts with a high oxygen storage capacity: the direct room temperature synthesis of CeO<sub>2</sub>-ZrO<sub>2</sub> solid solutions, *J. Chem. Soc., Chem. Commun.* **1995**, 2181–2182.
44. M. Yashima, K. Marimoto, N. Ishizawa, M. Yoshimura, Zirconia-ceria solid solution synthesis and the temperature-time-transformation diagram for the 1:1 composition, *J. Am. Ceram. Soc.* **1993**, *76*, 1745–1750.
45. T. Mongstad, C. C. You, A. Thogersen, J. P. Maehlen, C. P.-Björkman, B. C. Hauback, S. Z. Karazhanov, Mg<sub>y</sub>Ni<sub>1-y</sub>(H<sub>x</sub>) thin films deposited by magnetron co-sputtering, *J. Alloys Compd.* **2012**, *527*, 76–83.
46. S. Chen, M. Xue, Y. Li, Y. Pan, L. Zhu, S. Qiu, Rational design and synthesis of Ni<sub>x</sub>Co<sub>3-x</sub>O<sub>4</sub> nanoparticles derived from multivariate MOF-74 for supercapacitors, *J. Mater. Chem. A* **2015**, *3*, 20145–20152.
47. J. Geserick, T. Froschl, N. Husing, G. Kucerova, M. Makosch, T. Diemant, S. Eckleb, R. J. Behm, Molecular approaches towards mixed metal oxides and their behaviour in mixed oxide support Au catalysts for CO oxidation, *Dalton Trans.* **2011**, *40*, 3269–3286.
48. W. Cai, Q. Zhong, W. Zhao, Y. Bu, Focus on the modified Ce<sub>x</sub>Zr<sub>1-x</sub>O<sub>2</sub> with the rigid benzene-multi-carboxylate ligands and its catalysis in oxidation of NO, *Appl. Catal., B* **2014**, *158–159*, 258–268.
49. J. Y. Kim, S. H. Kang, H. S. Kim, Y. E. Sung, Preparation of highly ordered mesoporous Al<sub>2</sub>O<sub>3</sub>/TiO<sub>2</sub> and its application in dye-sensitized solar cells, *Langmuir* **2010**, *26*, 2864–2870.

50. Z. Zhou, T. Zeng, Z. Cheng, W. Yuan, Preparation and characterization of titania–alumina mixed oxides with hierarchically macro-/mesoporous structures. *Ind. Eng. Chem. Res.* **2011**, *50*, 883–890.
51. Y. Ding, G. Zhang, H. Wu, B. Hai, L. Wang, Y. Qian, Nanoscale magnesium hydroxide and magnesium oxide powders: control over size, shape, and structure via hydrothermal synthesis, *Chem. Mater.* **2001**, *13*, 435–440.
52. N. Sutradhar, A. Sinhamahapatra, S. K. Pahari, P. Pal, H. C. Bajaj, I. Mukhopadhyay, A. B. Panda, Controlled synthesis of different morphologies of MgO and their use as solid base catalysts, *J. Phys. Chem. C* **2011**, *115*, 12308–12316.
53. B. Huang, H. Kobayashi, H. Kitagawa, Facile synthesis of small MgO nanoparticle/metal organic framework hybrid material, *Chem. Lett.* **2014**, *43*, 1459–1460.
54. Y. Li, J. Shi, Hollow-structured mesoporous materials: chemical synthesis, functionalization and applications, *Adv. Mater.* **2014**, *26*, 3176–3205.

## Chapter 2.

### **A simple solvothermal approach to Al<sub>2</sub>O<sub>3</sub>–TiO<sub>2</sub> and ZnO–TiO<sub>2</sub> mesoporous hollow spherical composite nanoassemblies consisting of Al<sub>2</sub>O<sub>3</sub> or ZnO fine primary nanoparticles mixed with TiO<sub>2</sub> domains**

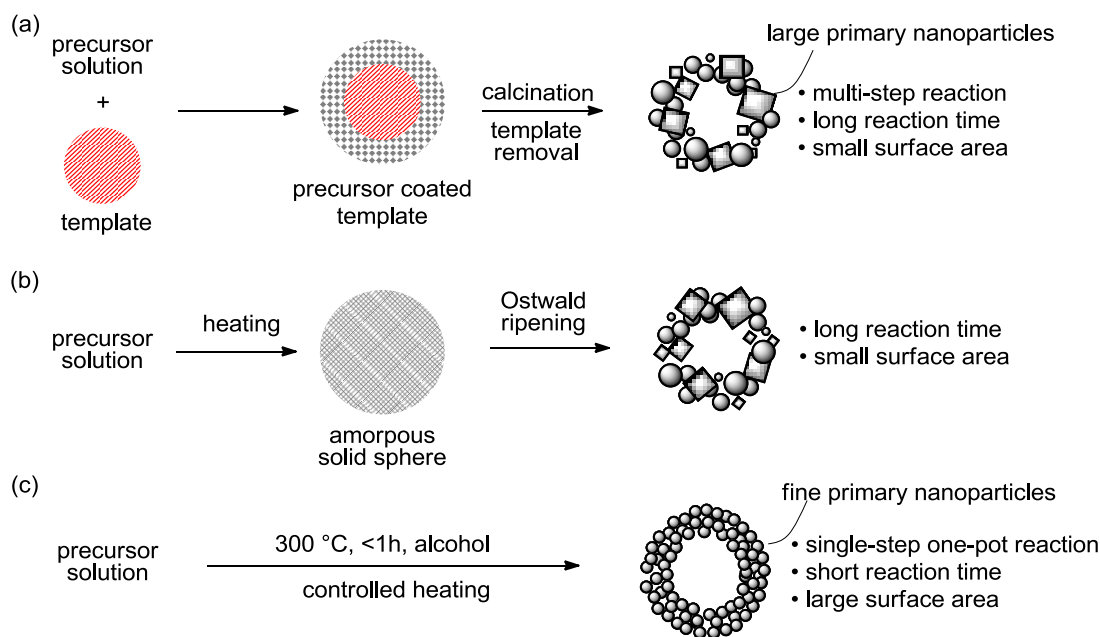
#### **2-1 Introduction**

Mesoporous nanomaterials with an internal cavity, which are known as hollow nanomaterials, have received much attention, since they have not only a large inner cavity to store materials but also numerous peripheral pores to access the inner cavity. They can be utilized as nanocontainers, drug delivery vehicles, nanoreactors, catalyst supports, electrode materials for energy storage, etc.<sup>[1–6]</sup> Mesoporous Al<sub>2</sub>O<sub>3</sub>, SiO<sub>2</sub>, TiO<sub>2</sub>, MnO<sub>2</sub>, and SnO<sub>2</sub> are examples of nanomaterials with this intriguing morphology.<sup>[7–10]</sup> In order to obtain these mesoporous hollow nanomaterials, sacrificial hard templates such as polystyrene, carbon, and SiO<sub>2</sub> are commonly used.<sup>[1,11]</sup> However, the hard template method is somewhat complicated because of the inevitable multi-step reactions, including the necessary template removal (Scheme 2-1a). Commonly used calcination of the organic or carbon templates to remove them often causes aggregation and/or agglomeration of their particles and sometimes decreases the surface area of the nanomaterials.<sup>[8]</sup> SiO<sub>2</sub> templates can be removed by chemical etching; however, the hollow morphology of nanomaterials is sometimes damaged by this treatment.<sup>[13,14]</sup> Even in the case of soft templates such as micelles and emulsions, template removal is indispensable to construct mesoporous hollow nanostructures.<sup>[1,11]</sup> Thus, template methods involve several limitations for the synthesis of mesoporous hollow materials. Instead, template-free synthesis of hollow spherical nanoassemblies has been developed by invoking Ostwald ripening in high-temperature media. For example, the synthesis of hollow spherical nanoassemblies of metal oxides such as TiO<sub>2</sub>, Fe<sub>2</sub>O<sub>3</sub>, ZnO, and

SnO<sub>2</sub> by template-free solvothermal methods has been reported.<sup>[1,10,15–17]</sup> However, the formation of the internal cavity still requires a long reaction time (of several hours to several days), which causes simultaneous enlargement of primary nanoparticles, leading to a decrease in surface area (Scheme 2-1b). Therefore, the development of simple and template-free synthetic methods for mesoporous spherical hollow nanoassemblies with large surface area still remains necessary.

Previously, Wang et al. developed a single-step, one-pot, template-free, and alcohol-based solvothermal method that yielded individual spherical mesoporous nanoassemblies of TiO<sub>2</sub>.<sup>[19,20]</sup> In this method, spherical hollow nanoassemblies with very fine primary nanoparticles (<10 nm) were synthesized in a relatively short reaction time (<1 h) by slow heating (5.4 °C min<sup>-1</sup>) up to 300 °C in the solvothermal reaction (Scheme 2-1c). The phenomenon affording hollow structure was ascribed to the Ostwald ripening, where the amorphous TiO<sub>2</sub> spherical solid nanoassemblies, afforded in the early stage of the heating process, converted to crystalline anatase TiO<sub>2</sub> with hollow morphology at high-temperature.<sup>[19,20]</sup> Phthalic acid is essential for the formation of hollow composite TiO<sub>2</sub> nanoassemblies i) through gradual water generation, being necessary for the hydrolysis of alkyl titanate, by ester formation with methanol at the elevated temperature and ii) as an acid catalyst for the hydrolysis, where the acid is incorporated at most 10% in weight on the surface of the particles.<sup>[18–20]</sup> Similarly, SiO<sub>2</sub>, ZnO, ZrO<sub>2</sub>, and CeO<sub>2</sub> solid MARIMOs were successfully synthesized.<sup>[20]</sup> The one-pot syntheses of different metal-doped MARIMOs, and a ship-in-a-bottle technique to obtain yolk-core-shell structures with inner noble metal alloy cores have also been developed.<sup>[21–22]</sup>

On the other hand, much effort has been devoted to the synthesis of TiO<sub>2</sub>-containing mixed metal oxide nanomaterials, such as MgO–TiO<sub>2</sub>, Al<sub>2</sub>O<sub>3</sub>–TiO<sub>2</sub>, SiO<sub>2</sub>–TiO<sub>2</sub>, ZnO–TiO<sub>2</sub>,



**Scheme 2-1.** Schematic of synthesis of mesoporous hollow nanomaterials by (a) the template method, (b) the typical template-free solvothermal method, and (c) our template-free alcohol-based solvothermal method.

ZrO<sub>2</sub>-TiO<sub>2</sub>, CeO<sub>2</sub>-TiO<sub>2</sub>, and In<sub>2</sub>O<sub>3</sub>-TiO<sub>2</sub>,<sup>[23-28]</sup> because advantageous synergistic effects are expected to occur. In particular, composites of TiO<sub>2</sub> with Al<sub>2</sub>O<sub>3</sub> and TiO<sub>2</sub> with ZnO are of interest among these systems, because these abundant and nontoxic metal oxides can be mixed with TiO<sub>2</sub> to improve its chemical and physical properties.<sup>[25,29,30]</sup> Al<sub>2</sub>O<sub>3</sub>-TiO<sub>2</sub> composites have been prepared by several methods, for example, solid-state hydrolysis of Al doped TiCl<sub>3</sub> precursors,<sup>[30]</sup> sol-gel reactions with self-assembly processes,<sup>[31]</sup> and precipitation methods of Al- and Ti-containing materials.<sup>[29,32]</sup> ZnO-TiO<sub>2</sub> composite nanomaterials have also been prepared by several methods, such as mixing TiO<sub>2</sub> nanoparticles with a zinc acetate solution,<sup>[33]</sup> electrospinning of titanium alkoxide/Zn acetate viscous gel,<sup>[34]</sup> electrostatic deposition of TiO<sub>2</sub> nanoparticles on ZnO,<sup>[35]</sup> and a two-step hydrothermal method producing a core-shell structure.<sup>[26]</sup> However, the synthesis of Al<sub>2</sub>O<sub>3</sub>-TiO<sub>2</sub> and ZnO-TiO<sub>2</sub> mixed composite nanoassemblies at the nano-level with hollow spherical morphologies, permitting the effective control of their atomic compositions, has not been intensively studied. In this

chapter, the one-pot, single-step, and template-free synthetic method is extended to the synthesis of hollow spherical  $\text{Al}_2\text{O}_3\text{-TiO}_2$  and  $\text{ZnO-TiO}_2$  composite nanoassemblies consisting of  $\text{Al}_2\text{O}_3$  and  $\text{ZnO}$  fine primary nanoparticles mixed with  $\text{TiO}_2$  domains, respectively.

## 2-2 Results and Discussion

$\text{Al}_2\text{O}_3\text{-TiO}_2$  composite nanoassemblies were synthesized by heating ( $5.4\text{ }^\circ\text{C min}^{-1}$ ) precursor solutions consisting of  $\text{Al}(\text{O}^i\text{Pr})_3$ ,  $\text{Ti}(\text{O}^i\text{Pr})_4$ , phthalic acid, and methanol with different Al/Ti mixing ratios (Table 2-1). The obtained hollow  $\text{Al}_2\text{O}_3\text{-TiO}_2$  composite nanoassemblies are referred to as Al/Ti-0.75, Al/Ti-0.50, Al/Ti-0.25, Al/Ti-0.20, Al/Ti-0.10, and Al/Ti-0.05, where the numbers denote the molar portion of  $\text{Al}(\text{O}^i\text{Pr})_3/(\text{Al}(\text{O}^i\text{Pr})_3 + \text{Ti}(\text{O}^i\text{Pr})_4)$  in the precursor solutions. Figure 2-1 shows transmission electron microscopy (TEM) and energy dispersive X-ray (EDX) mapping images of the  $\text{Al}_2\text{O}_3\text{-TiO}_2$  composite nanoassemblies. The morphologies of the nanoassemblies were affected by the Al/Ti ratio in the precursor solutions. Irregularly aggregated hollow  $\text{Al}_2\text{O}_3\text{-TiO}_2$  composite nanoassemblies were obtained from the precursor solution with a high Al content of 75% (Figure 2-1a). When the Al content in the precursor solutions decreased (Al = 25–50%), fused spherical hollow nanoassemblies of 3  $\mu\text{m}$  average size were produced (Figures 2-1b,c), while spherical hollow composite nanoassemblies with an average diameter of 1.1–1.3  $\mu\text{m}$  (Table 2-2) were obtained with lower Al contents (5–20%, Figures 2-1d–f). EDX mapping images (Figures 2-1a–f) indicate the even distribution of Al and Ti atoms throughout the hollow composite nanoassemblies irrespective of their Al/Ti ratios. Figure 2-2 shows the relationship between the atomic compositions of the hollow  $\text{Al}_2\text{O}_3\text{-TiO}_2$  composite nanoassemblies determined by EDX analysis on TEM and the molar ratios of the precursor solutions. A linear relationship with a slope approximately equal to 1 was observed, indicating that the composition of the

hollow Al<sub>2</sub>O<sub>3</sub>–TiO<sub>2</sub> composite nanoassemblies can be easily controlled by adjusting the Al/Ti mixing ratio in the precursor solutions. Quite broad profiles corresponding to anatase TiO<sub>2</sub> phase were obtained in X-ray diffraction (XRD) patterns (JCPDS 00–021–1272) of Al<sub>2</sub>O<sub>3</sub>–TiO<sub>2</sub> composite nanoparticles synthesized from the precursor solutions with high Al contents (50–75%) (Figures 2-3a,b). The peak shapes became sharper with increased Ti content in Al<sub>2</sub>O<sub>3</sub>–TiO<sub>2</sub> composite nanoassemblies (Figures 2-3c–f). Actually, the primary nanoparticles observed with high-resolution transmission electron microscopy (HRTEM) images (Figure 2-4) gradually changed from non-characteristic to fine nanoparticles in accordance with the Ti content in the Al<sub>2</sub>O<sub>3</sub>–TiO<sub>2</sub> composite nanoassemblies. No peak derived from Al<sub>2</sub>O<sub>3</sub> was observed in the XRD patterns, though the EDX mapping images clearly indicated the existence of Al atoms and the homogeneity of Al and Ti atoms in the Al<sub>2</sub>O<sub>3</sub>–TiO<sub>2</sub> composite nanoassemblies. This observation indicates that amorphous Al<sub>2</sub>O<sub>3</sub>, the formation of which could be ascribed to the lower reaction temperature than that required for the crystallization of Al<sub>2</sub>O<sub>3</sub>,<sup>[36]</sup> was embedded between anatase TiO<sub>2</sub> domains. The specific surface area determined by the Brunauer–Emmett–Teller (BET) method also correlated with the Al/Ti ratio and increased with Al content (Table 2-2, Figure 2-5). In particular, it is notable that the BET specific surface area of Al/Ti–0.75 and Al/Ti–0.50 exceeded 600 m<sup>2</sup> g<sup>-1</sup>.

**Table 2-1.** Al/Ti Mixing ratio in precursor solutions.

Sample name	Concentration (mol L <sup>-1</sup> )	
	Al(O <sup><i>i</i></sup> Pr) <sub>3</sub>	Ti(O <sup><i>i</i></sup> Pr) <sub>4</sub>
Al/Ti–0.75	0.075	0.025
Al/Ti –0.50	0.050	0.050
Al/Ti –0.25	0.025	0.075
Al/Ti –0.20	0.020	0.080
Al/Ti –0.10	0.010	0.090
Al/Ti –0.05	0.005	0.095

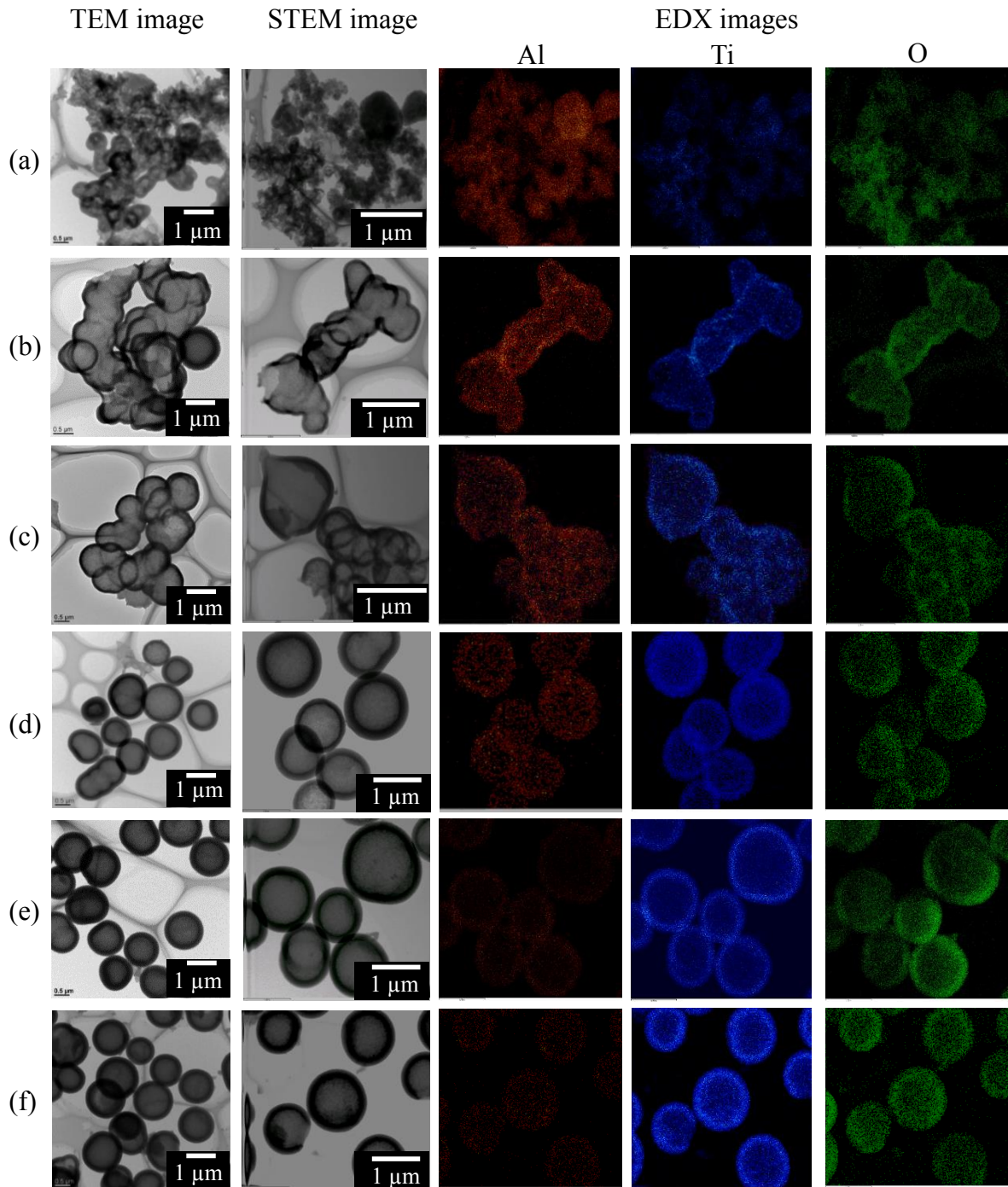


**Figure 2-1.** TEM and EDX mapping images of (a) Al/Ti-0.75, (b) Al/Ti-0.50, (c) Al/Ti-0.25, (d) Al/Ti-0.20, (e) Al/Ti-0.10, and (f) Al/Ti-0.05 hollow composite nanoassemblies.

**Table 2-2.** Particle sizes, specific surface areas, and pore diameters of Al<sub>2</sub>O<sub>3</sub>-TiO<sub>2</sub> composite nanoassemblies.

Sample name	Particle diameter (μm) <sup>a</sup>	BET-calculated specific surface area (m <sup>2</sup> g <sup>-1</sup> ) <sup>b</sup>	Pore diameter (nm) <sup>c</sup>
Al/Ti-0.75	1.4±7 <sup>d</sup>	606	2.11
Al/Ti -0.50	3±1 <sup>d</sup>	618	2.05
Al/Ti -0.25	3±2 <sup>d</sup>	431	1.87
Al/Ti -0.20	1.1±3	262	1.79
Al/Ti -0.20	1.3±2	235	2.06
Al/Ti -0.05	1.2±2	240	1.88

<sup>a</sup>Average of at least 50 nanoassemblies in TEM images, <sup>b</sup>atomic composition ratio roughly calculated by EDX analysis on TEM, <sup>c</sup>calculated by *t* method, <sup>d</sup>aggregated and/or fused nanoassemblies.

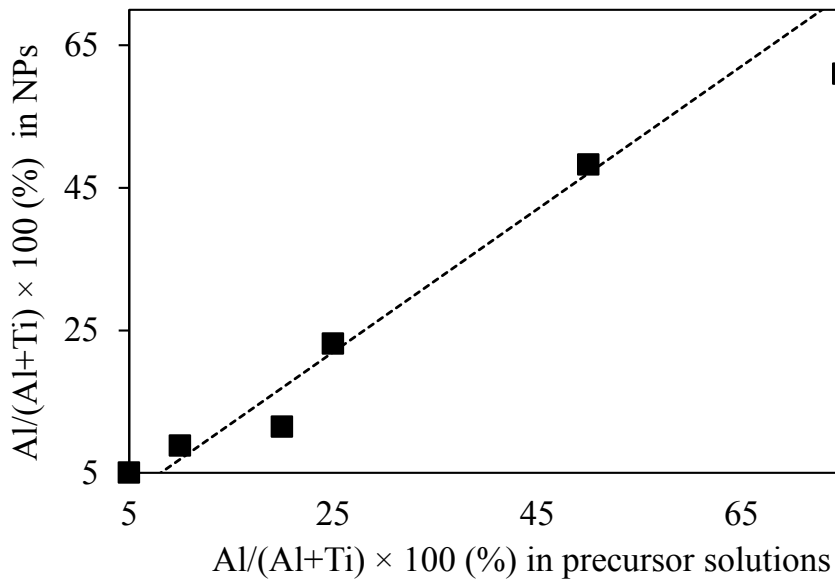


**Figure 2-2.** Plot of atomic compositions of Al<sub>2</sub>O<sub>3</sub>-TiO<sub>2</sub> hollow composite nanoassemblies (estimated by EDX) versus the initial molar fractions of Al in the precursor solutions.

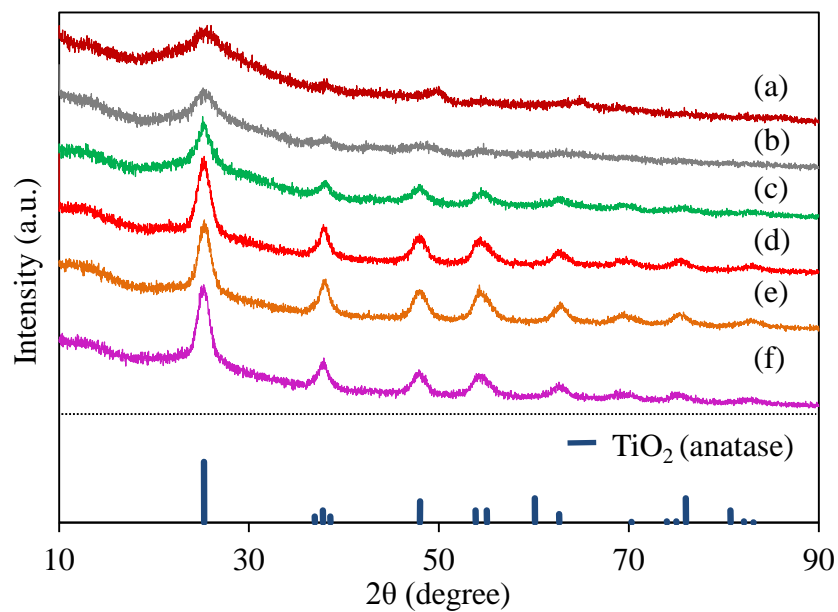


**Figure 2-3.** XRD patterns of (a) Al/Ti-0.75, (b) Al/Ti-0.50, (c) Al/Ti-0.25, (d) Al/Ti-0.20, (e) Al/Ti-0.10, and (f) Al/Ti-0.05 hollow composite nanoassemblies.

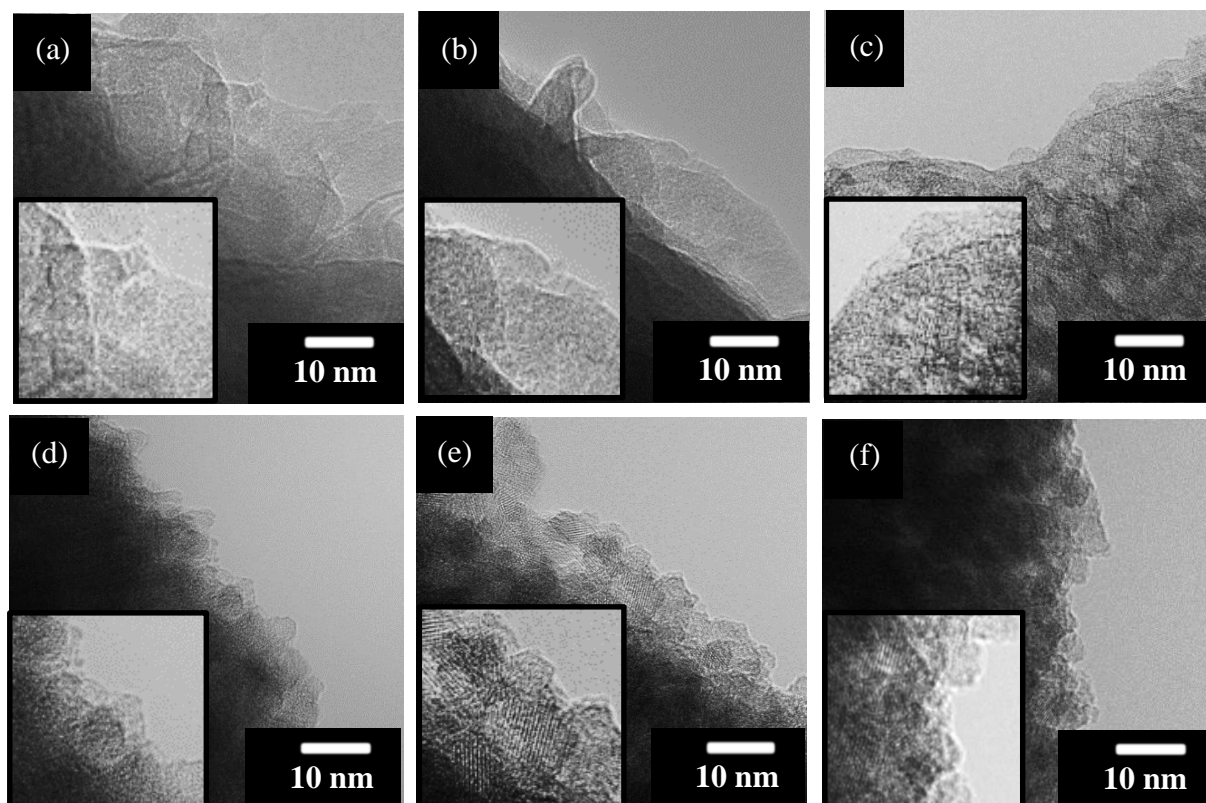


**Figure 2-4.** HRTEM images of (a) Al/Ti-0.75, (b) Al/Ti-0.50, (c) Al/Ti-0.25, (d) Al/Ti-0.20, (e) Al/Ti-0.10, and (f) Al/Ti-0.05 hollow composite nanoassemblies.

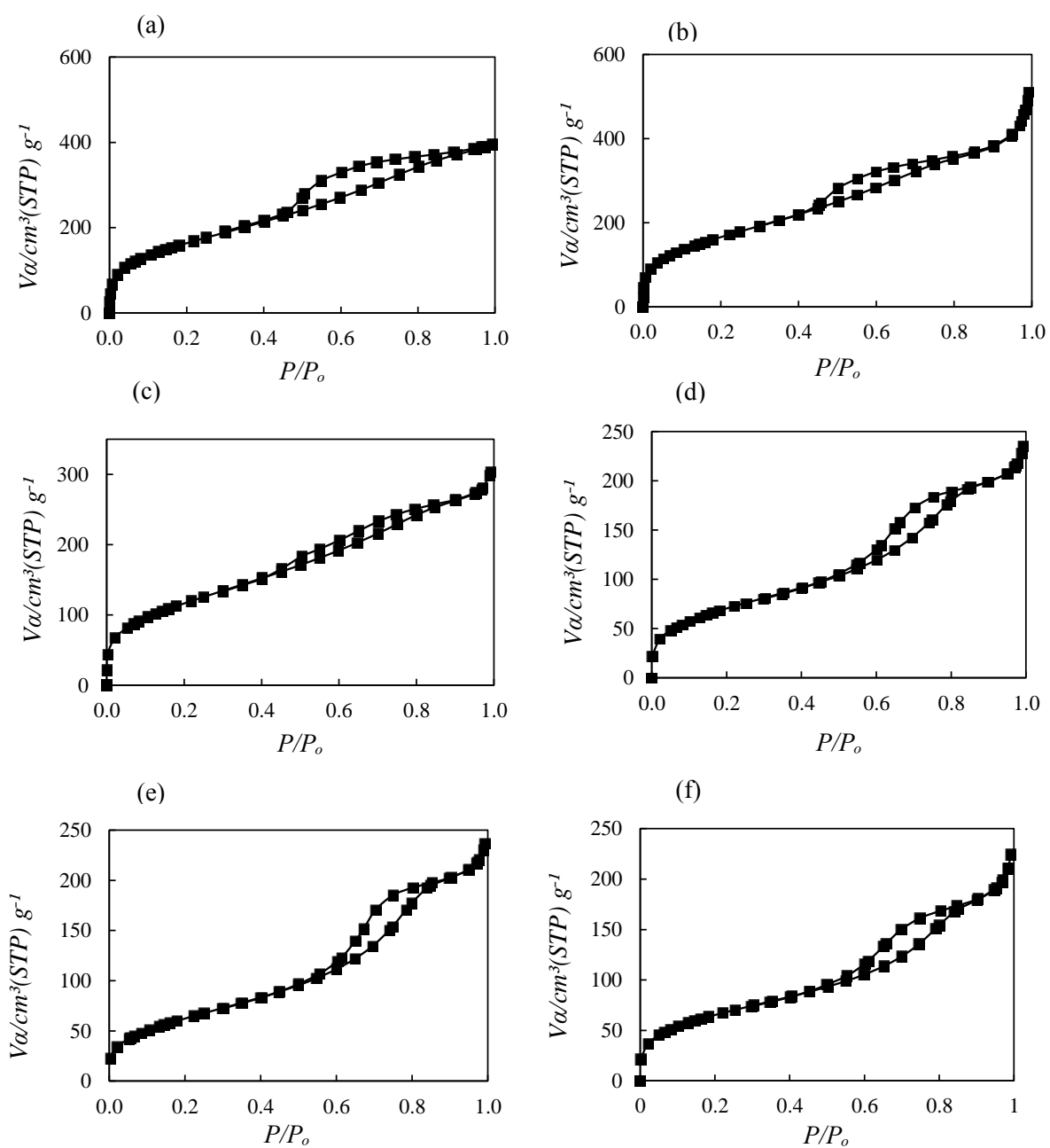


**Figure 2-5.**  $\text{N}_2$  adsorption–desorption isotherms of (a) Al/Ti–0.75, (b) Al/Ti–0.50, (c) Al/Ti–0.25, (d) Al/Ti–0.20, (e) Al/Ti–0.10, and (f) Al/Ti–0.05 hollow composite nanoassemblies.

Similarly, the ZnO–TiO<sub>2</sub> composite nanoassemblies were obtained by heating (5.4 °C min<sup>-1</sup>) Zn/Ti mixed precursor solutions in methanol with different mixing ratios (Table 2-3). These ZnO–TiO<sub>2</sub> composite nanoassemblies are referred to as Zn/Ti–0.75, Zn/Ti–0.50, Zn/Ti–0.25, Zn/Ti–0.20, Zn/Ti–0.10, and Zn/Ti–0.05, where each number denotes the molar portion of Zn(OAc)<sub>2</sub>/(Zn(OAc)<sub>2</sub> + Ti(O<sup>i</sup>Pr)<sub>4</sub>) in the precursor solution for that set of composite nanoassemblies. Figure 2-6 shows the TEM and EDX mapping images of the ZnO–TiO<sub>2</sub> composite nanoassemblies. Figure 2-7 shows the relationship between the atomic compositions of the hollow ZnO–TiO<sub>2</sub> composite nanoassemblies as determined by EDX analysis on TEM and the molar ratios of the precursor solutions. The morphology of the ZnO–TiO<sub>2</sub> nanoassemblies was clearly affected by the Zn/Ti ratio in the precursor solutions. A linear relationship similar to the case of Al<sub>2</sub>O<sub>3</sub>–TiO<sub>2</sub> was observed, indicating that the composition of the hollow ZnO–TiO<sub>2</sub> composite nanoassemblies can be easily controlled by adjusting the Al/Ti mixing ratio in the precursor solutions. A mixture of monodispersed solid spherical nanoassemblies and nanosheets was obtained by treating the precursor solution with Zn = 75% (Figure 2-6a). EDX mapping images showed the even distribution of Zn and Ti atoms throughout the solid spherical nanoassemblies, while the nanosheets contained very small amounts of Ti atoms. The XRD patterns of Zn/Ti–0.75 (Figure 2-8a) does not show diffraction peaks corresponding to either TiO<sub>2</sub> or ZnO but instead shows many complicated sharp peaks corresponding to a MOF constructed of Zn<sup>2+</sup> and phthalate anions.<sup>[37]</sup> When the Zn content decreased to 50%, the morphology of the composite nanoassemblies dramatically changed to produce fused hollow spheres (Figure 2-6b). The good dispersion of Zn and Ti in Zn/Ti–0.50 was confirmed by EDX mapping images (Figure 2-6b). However, the XRD patterns (Figure 2-8b) still showed sharp peaks ascribed to the MOF similar to Zn/Ti–0.75. For Zn = 5–25%, individual spherical hollow composite nanoassemblies with an average diameter of 0.9–1.5 μm were produced (Figures 2-6c–f), with peaks in their XRD patterns

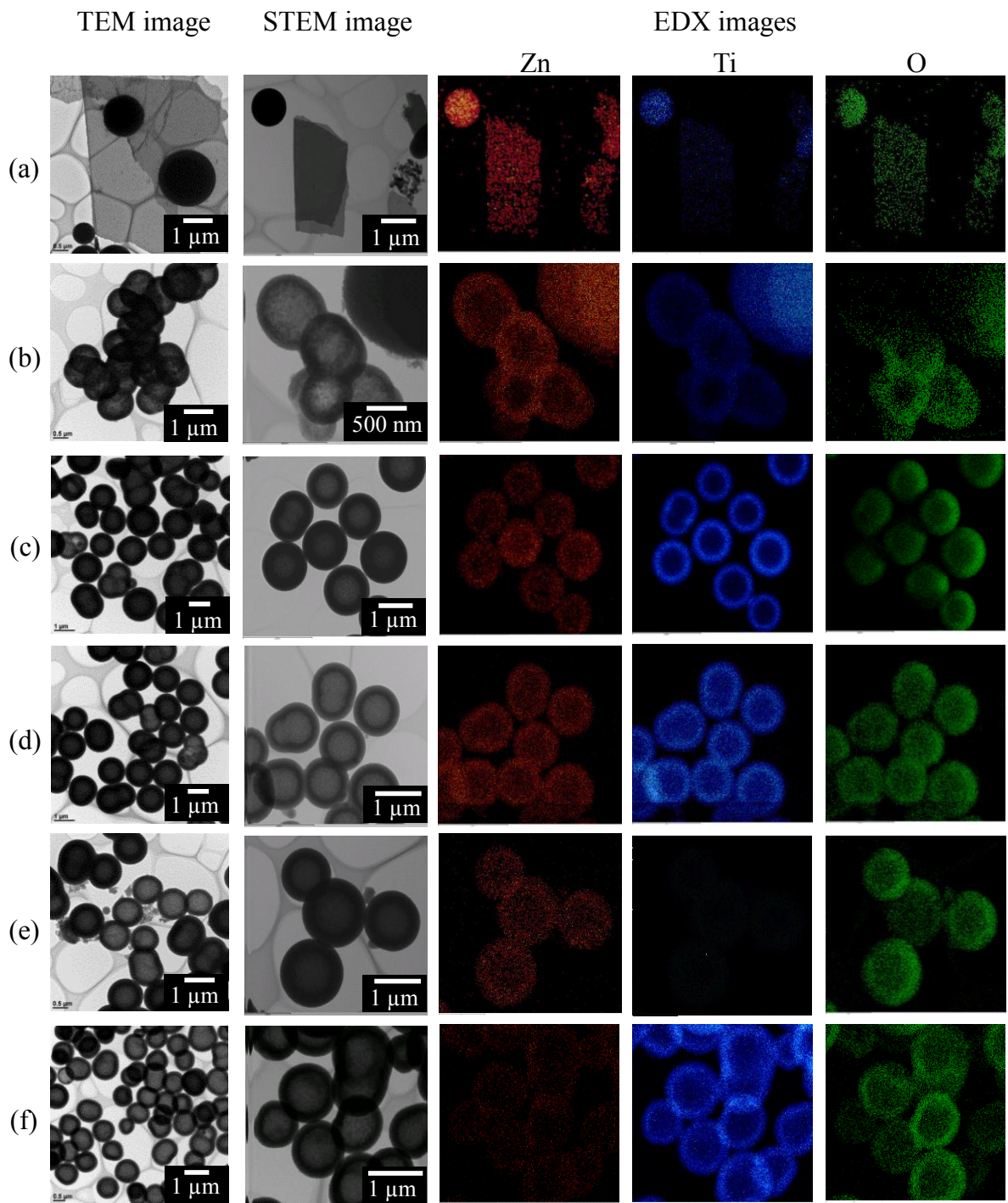


**Figure 2-6.** TEM and EDX mapping images of (a) Zn/Ti-0.75, (b) Zn/Ti-0.50, (c) Zn/Ti-0.25, (d) Zn/Ti-0.20, (e) Zn/Ti-0.10, and (f) Zn/Ti-0.05 composite nanoassemblies.

**Table 2-3.** Zn/Ti Mixing ration in precursor solutions

Sample name	Concentration (mol L <sup>-1</sup> )	
	Zn(OCOCH <sub>3</sub> ) <sub>2</sub> ·2H <sub>2</sub> O	Ti(O <sup><i>i</i></sup> Pr) <sub>4</sub>
Zn/Ti-0.75	0.075	0.025
Zn/Ti -0.50	0.050	0.050
Zn/Ti -0.25	0.025	0.075
Zn/Ti -0.20	0.020	0.080
Zn/Ti -0.20	0.010	0.090
Zn/Ti -0.05	0.005	0.095

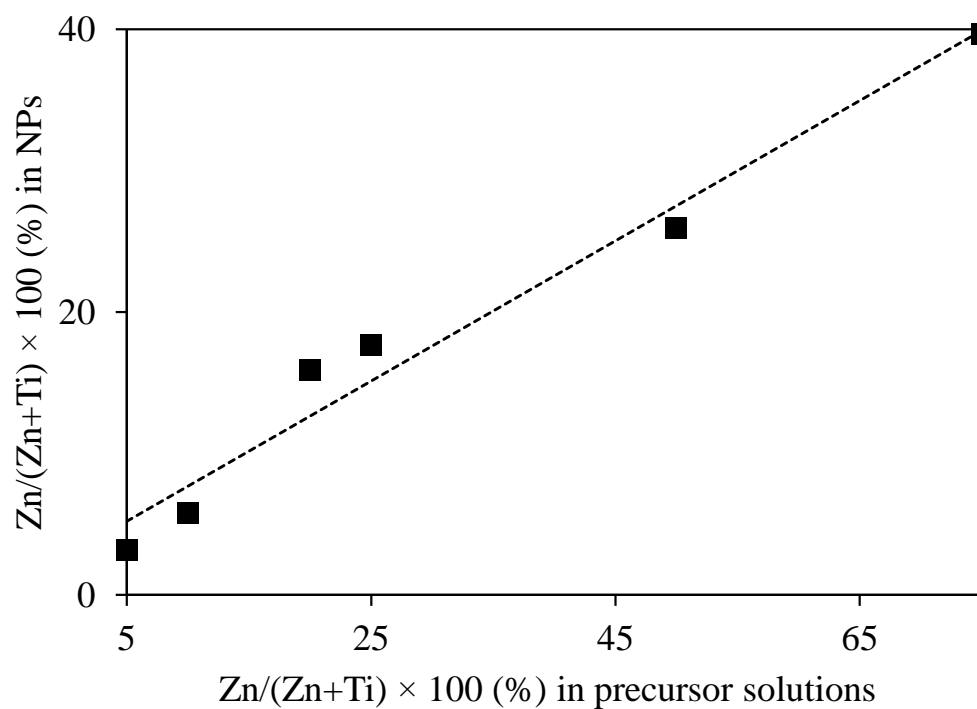


**Figure 2-7.** Plot of atomic compositions of ZnO–TiO<sub>2</sub> composite nanoassemblies (estimated by EDX) versus the initial molar fractions of Zn in the precursor solutions.

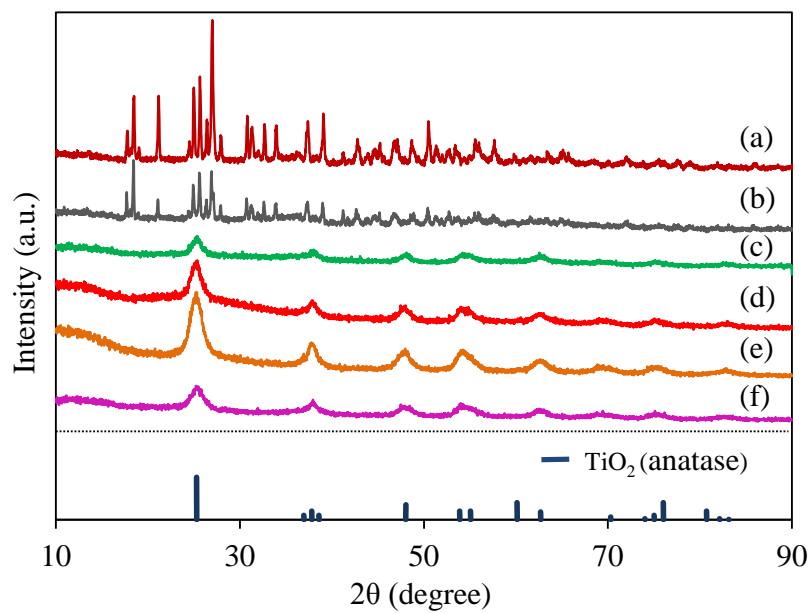


**Figure 2-8.** XRD patterns of (a) Zn/Ti-0.75, (b) Zn/Ti-0.50, (c) Zn/Ti-0.25, (d) Zn/Ti-0.20, (e) Zn/Ti-0.10, and (f) Zn/Ti-0.05 composite nanoassemblies.

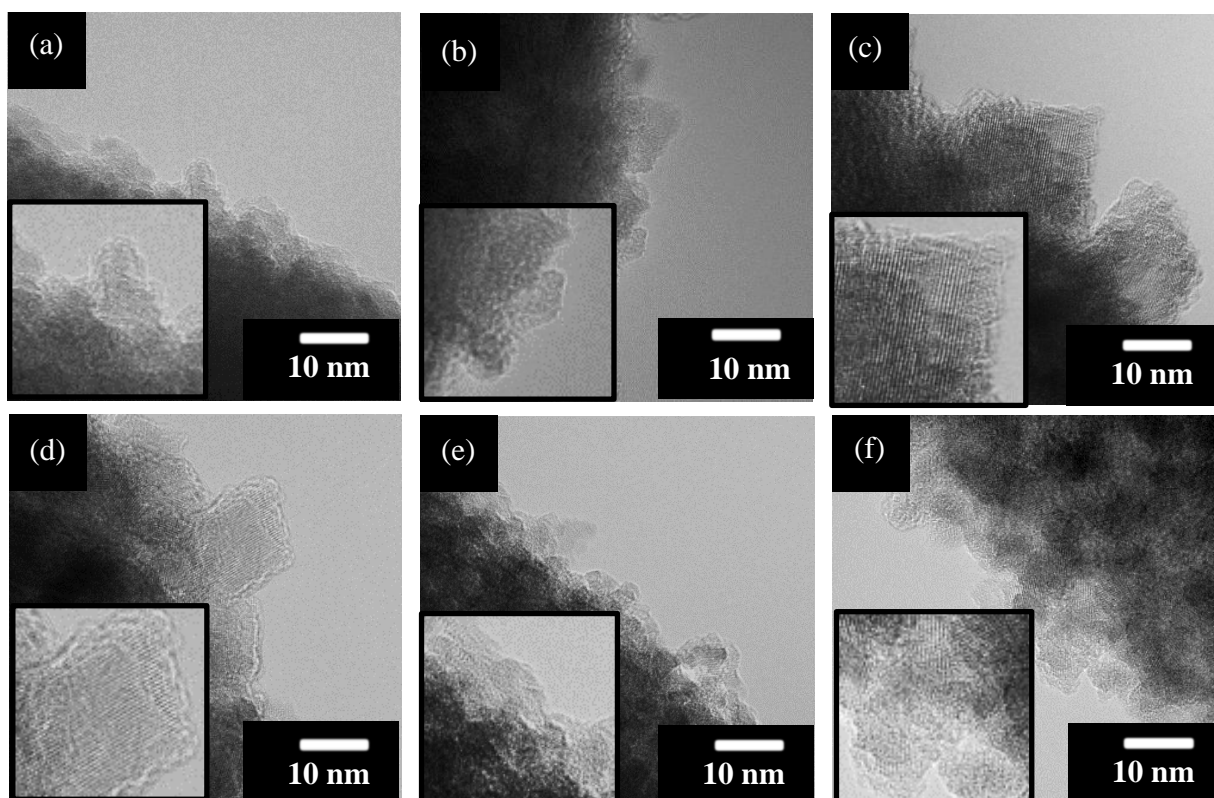


**Figure 2-9.** HRTEM images of (a) Zn/Ti-0.75, (b) Zn/Ti-0.50, (c) Zn/Ti-0.25, (d) Zn/Ti-0.20, (e) Zn/Ti-0.10, and (f) Zn/Ti-0.05 composite nanoassemblies.

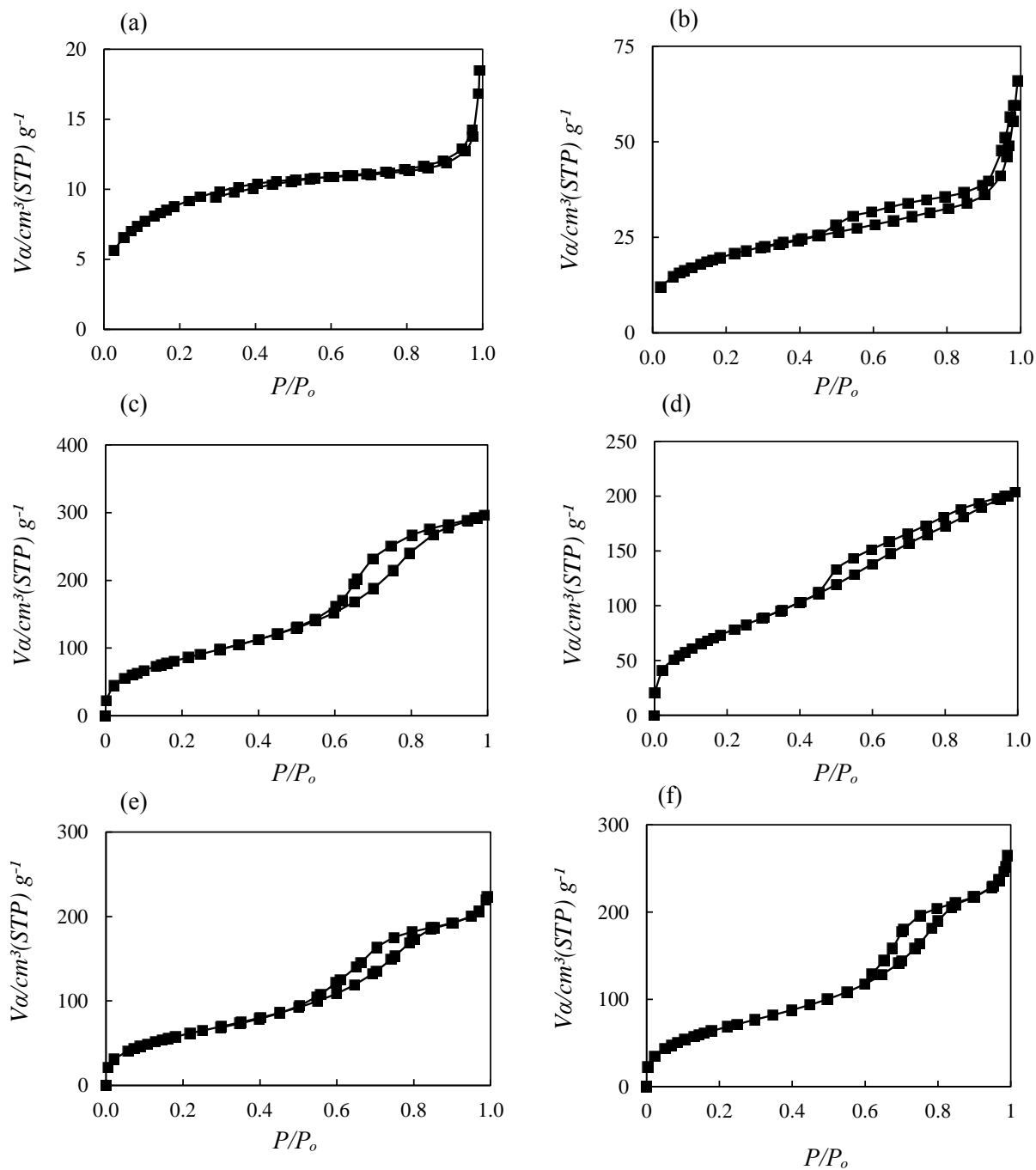


**Figure 2-10.** N<sub>2</sub> adsorption–desorption isotherms of (a) Zn/Ti–0.75, (b) Zn/Ti–0.50, (c) Zn/Ti–0.25, (d) Zn/Ti–0.20, (e) Zn/Ti–0.10, and (f) Zn/Ti–0.05 composite nanoassemblies.

**Table 2-4.** Particle sizes, specific surface areas, and pore diameters of ZnO–TiO<sub>2</sub> composite nanoassemblies.

Sample name	Particle diameter (μm) <sup>a</sup>	BET-calculated specific surface area (m <sup>2</sup> g <sup>-1</sup> ) <sup>b</sup>	Pore diameter (nm)
Ti/Zn–0.75	1.2±2	32	1.0 <sup>c</sup>
Ti/Zn–0.50	5±2 <sup>e</sup>	73	1.0 <sup>c</sup>
Ti/Zn–0.25	1.5±2	286	3.28 <sup>d</sup>
Ti/Zn–0.20	1.5±2	316	4.13 <sup>d</sup>
Ti/Zn–0.20	1.2±2	224	2.43 <sup>d</sup>
Ti/Zn–0.05	0.9±1	251	2.43 <sup>d</sup>

<sup>a</sup>Average of at least 50 nanoassemblies in TEM images, <sup>b</sup>atomic composition ratio roughly calculated by EDX analysis on TEM, <sup>c</sup>calculated by MP method, <sup>d</sup>calculated by BJH method, <sup>e</sup>fused nanoassemblies.

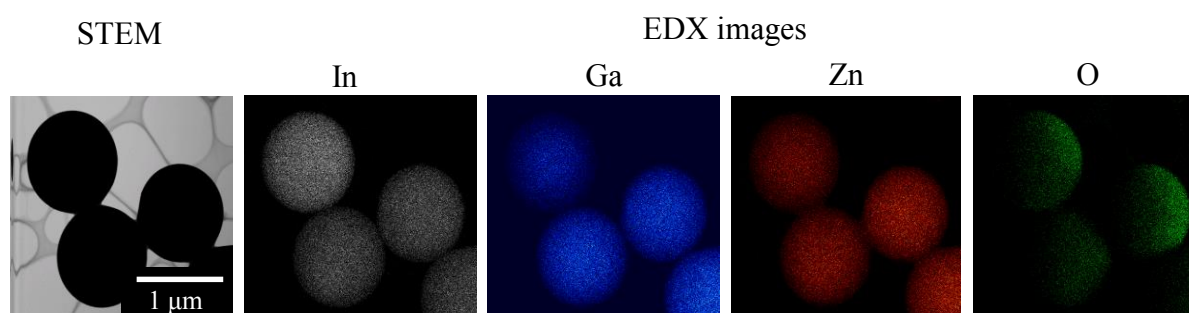


**Figure 2-11.** STEM and EDX mapping images of spherical In–Ga–Zn oxide composite nanoassemblies.

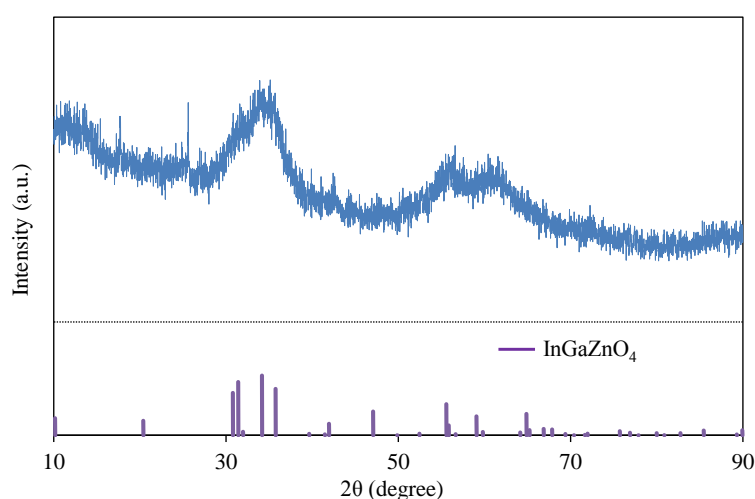


**Figure 2-12.** XRD pattern of spherical In–Ga–Zn oxide composite nanoassemblies (peak positions of one of the examples (JCPDS 01–070–3625) are shown with purple lines).

corresponding to the anatase  $\text{TiO}_2$  phase (Figures 2-8c–f). These peaks changed in breadth with the Ti content in the precursor solutions. Clear HRTEM images of the primary nanoparticles in the Zn/Ti–0.75 and Zn/Ti–0.50 nanoassemblies could not be obtained, possibly as a result of the large organic content of their MOF structures (Figures 2-9a,b). However, for other hollow ZnO– $\text{TiO}_2$  composite nanoassemblies (Zn = 5–25%), fine nanoparticles were observed in the HRTEM images (Figures 2-9c–f). The BET specific surface area of the MOFs containing Zn/Ti–0.75 and Zn/Ti–0.50 composite nanoassemblies are much lower than those of the other hollow ZnO– $\text{TiO}_2$  composite nanoassemblies, despite their micropores (Table 2-4, Figure 2-10). Thus, morphology-, size-, and pore-controlled hollow composite nanoassemblies of  $\text{Al}_2\text{O}_3$ – $\text{TiO}_2$  and ZnO– $\text{TiO}_2$  were successfully synthesized. Furthermore,  $\text{InGaZnO}_4$  (IGZO) were easily synthesized by a similar approach (Figures 2-11 and 2-12).

### 2-2-1 Heat tolerance of hollow $\text{Al}_2\text{O}_3$ – $\text{TiO}_2$ composite nanoassemblies

Anatase phase  $\text{TiO}_2$  is used in many photochemical applications.<sup>[38–40]</sup> The irreversible anatase-to-rutile phase transition often occurs upon heating  $\text{TiO}_2$  to temperatures of 600–750 °C, which restricts the high-temperature applications of anatase  $\text{TiO}_2$ .<sup>[41,42]</sup> Li et al. proposed that the anatase-to-rutile phase transition is initiated by the nucleation of rutile on the surface of fine primary nanoparticles of anatase  $\text{TiO}_2$  at elevated temperatures.<sup>[43]</sup> Pillai et al. reported that the starting temperature of the phase transition slightly increased to 800 °C by increasing the porosity of  $\text{TiO}_2$  nanomaterials through decreasing the number of anatase/anatase contact points.<sup>[44]</sup> The  $\text{TiO}_2$  hollow MARIMOs<sup>[14]</sup> also showed stability of both the anatase phase and the spherical hollow morphology at 800 °C, however the transition to the rutile phase and the collapse of the spherical hollow morphology occurred with calcination at 1000 °C (Figures 2-13 and 2-14). Further elevation of the anatase to rutile phase transition starting temperature to 1000 °C was accomplished by mixing  $\text{TiO}_2$  with other

metal oxides such as  $\text{SiO}_2$  and  $\text{Al}_2\text{O}_3$ .<sup>[42,45]</sup> These studies suggest that examining the heat properties of those hollow  $\text{Al}_2\text{O}_3$ - $\text{TiO}_2$  composite nanoassemblies is worthwhile.

The hollow  $\text{Al}_2\text{O}_3$ - $\text{TiO}_2$  composite nanoassemblies with Al = 5% clearly showed the anatase-to-rutile phase transition ( $\text{TiO}_2$  (rutile): JCPDS 00-021-1276) after calcination at 1000 °C for 1 h (Figure 2-15c). Al/Ti-0.25 experienced the partial formation of the rutile phase under similar conditions, while the anatase phase still remained (Figure 2-15b). However, with Al/Ti-0.50, the anatase phase survived completely with no rutile phase formation (Figure 2-15a). In addition, TEM images of the hollow composite nanoassemblies calcinated at 1000 °C clearly indicate that the hollow spherical morphology of composite nanoassemblies with Al = 25–50% remains intact (Figures 2-15a,b). Thus, high-temperature stability of anatase phase and hollow spherical morphology of  $\text{TiO}_2$  MARIMOs were demonstrated by mixing of  $\text{Al}_2\text{O}_3$  with  $\text{TiO}_2$  in nanoscopic level.

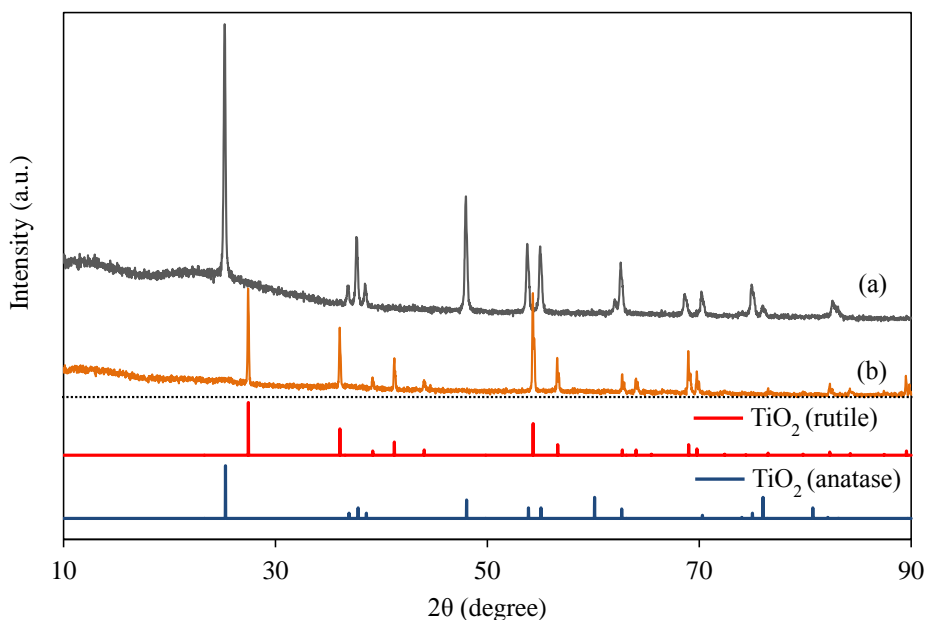


**Figure 2-13.** XRD patterns of  $\text{TiO}_2$  hollow MARIMO after calcination at (a) 800 °C and (b) 1000 °C for 1h.

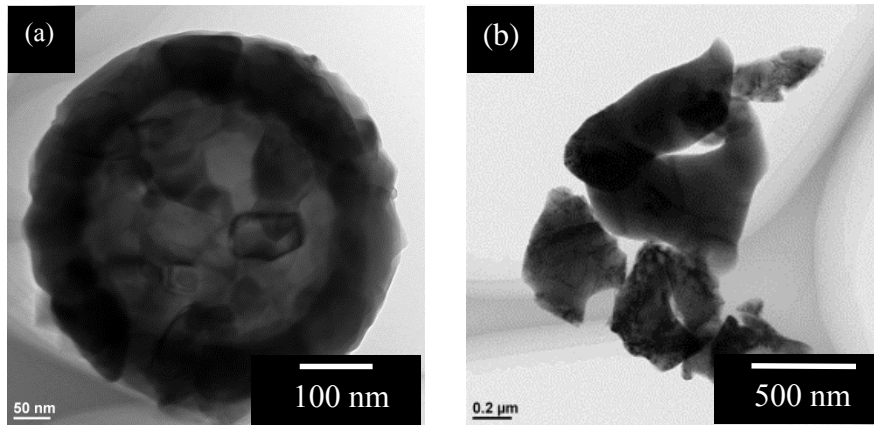


**Figure 2-14.** TEM images of TiO<sub>2</sub> hollow MARIMO after calcination at (a) 800 °C and (b) 1000 °C for 1h.

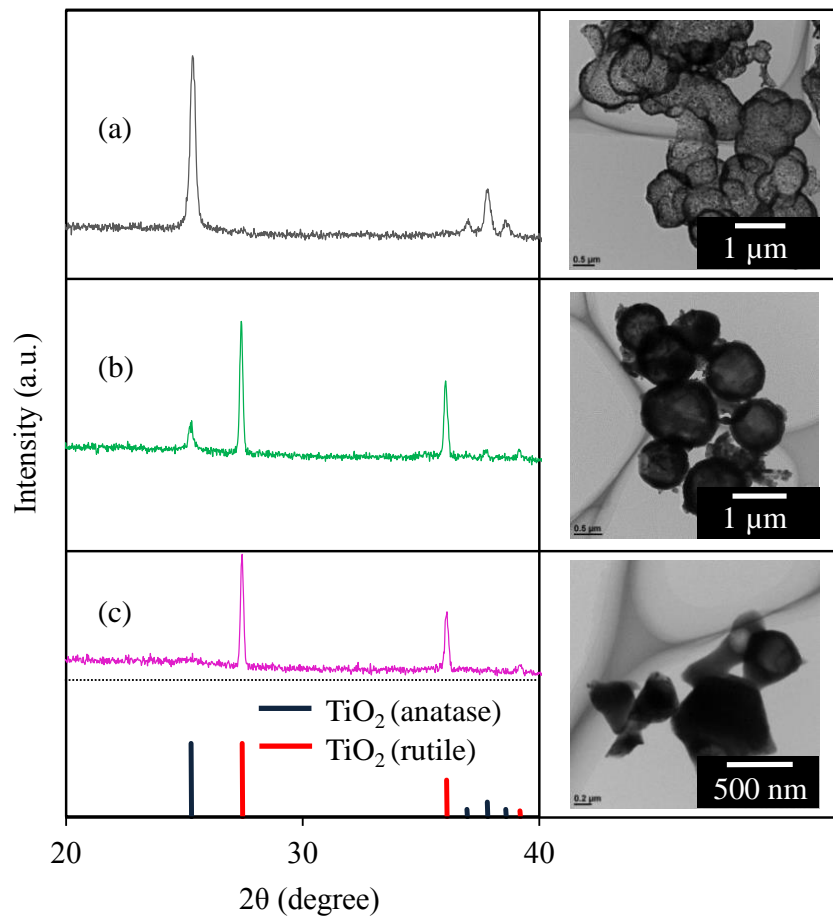


**Figure 2-15.** XRD patterns (left) and TEM images (right) of (a) Al/Ti-0.50, (b) Al/Ti-0.25, and (c) Al/Ti-0.05 hollow composite nanoassemblies after calcination at 1000 °C.

### 2-2-2 Band gap tuning of hollow ZnO–TiO<sub>2</sub> composite nanoassemblies

The band gap energy of TiO<sub>2</sub> has been tuned to adjust its photochemical properties.<sup>[46]</sup> ZnO–TiO<sub>2</sub> composites, for example, have been used for this purpose in thin films.<sup>[47]</sup> Therefore, the band gap energies of those hollow spherical ZnO–TiO<sub>2</sub> composite nanoassemblies should also be tunable by changing the ZnO/TiO<sub>2</sub> mixing ratio in the nanoassemblies. Band gap energies calculated by the Tauc plot method through ultraviolet-visible (UV-Vis) spectroscopy<sup>[48]</sup> are shown in Figure 2-16. Similar band gap energies of ca. 3.3 eV were observed for the as-prepared hollow spherical composite nanoassemblies despite different ZnO–TiO<sub>2</sub> mixing ratios, while calcination at 500 °C for 1 h caused relatively large shifts in band gap energies to lower values of 3.12–3.21 eV. The band gap energy shifts are usually explained by the quantum confinement effect of primary nanoparticles, in which the

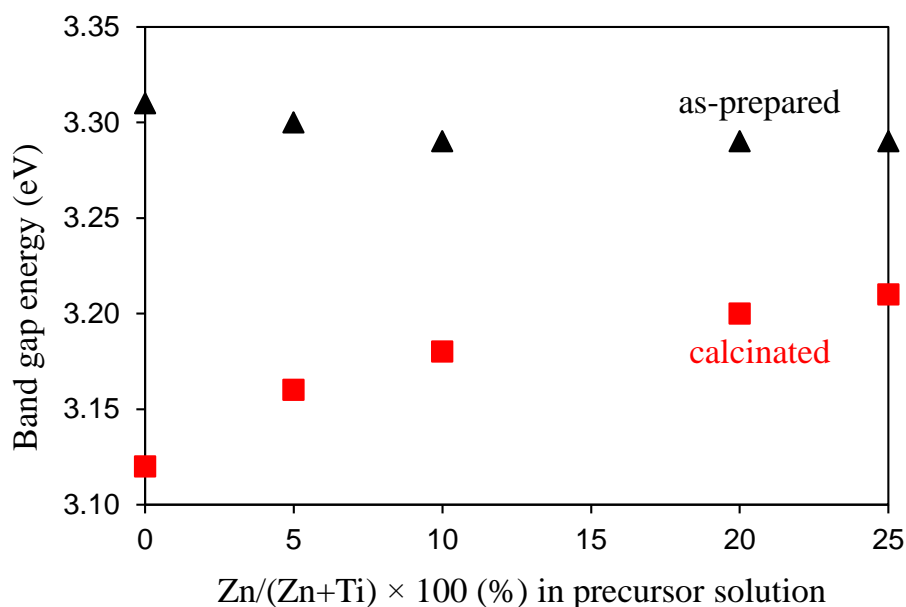


**Figure 2-16.** Plots of band gap energies of hollow spherical ZnO–TiO<sub>2</sub> composite nanoassemblies versus the initial molar fractions of Zn in precursor solutions.

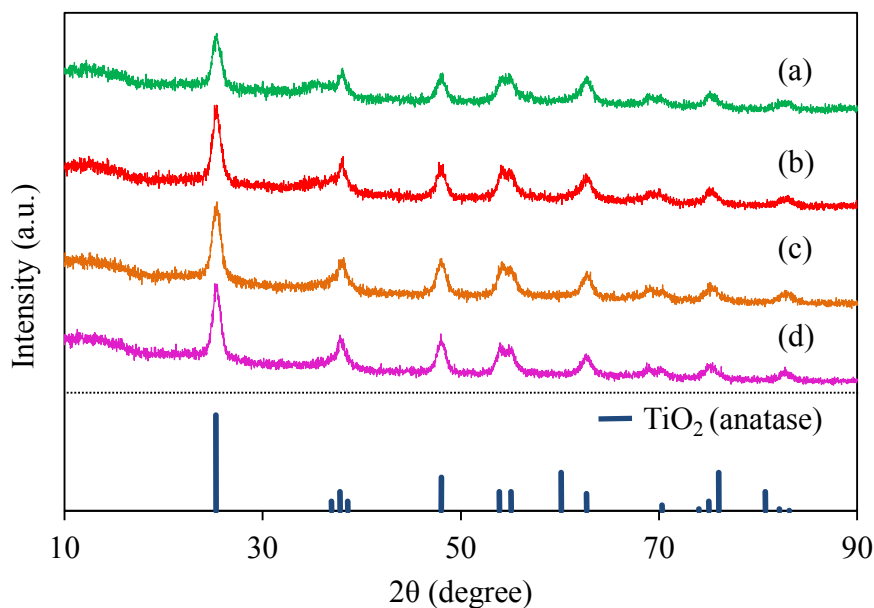


**Figure 2-17.** XRD patterns of (a) Zn/Ti–0.25, (b) Zn/Ti–0.20, (c) Zn/Ti–0.10, and (d) Zn/Ti–0.05 hollow composite nanoassemblies after calcination at 500 °C for 1 h.

smaller nano-crystals exhibit higher band gap energies.<sup>[49]</sup> However, in the hollow spherical ZnO–TiO<sub>2</sub> composite nanoassemblies, clear size growth of the primary crystals was not observed even after calcination at 500 °C for 1 h, judging from the peak width in the XRD data (Figures 2-8 and 2-17). In the case of the higher contents of Zn, the hollow spherical ZnO–TiO<sub>2</sub> composite nanoassemblies resulted in larger band gap energy values with smaller shifts (Figure 2-16), suggesting that the amorphous ZnO included in the nanoassemblies can suppress the crystal size growth of TiO<sub>2</sub> even at levels undetectable by XRD. Thus, the band gap energy tuning of TiO<sub>2</sub> nanoassemblies was simply accomplished through the primary nanoparticle size control by mixing with ZnO followed by calcination, without damaging their mesoporous hollow spherical morphologies.

### 2-2-3 Chemical etching of hollow spherical composite nanoassemblies

The obtained hollow  $\text{Al}_2\text{O}_3\text{-TiO}_2$  and  $\text{ZnO-TiO}_2$  composite nanoassemblies have enough physical strength to tolerate magnetic stirring in suspensions. On the other hand, chemical treatment with a strong base of  $1 \text{ mol L}^{-1}$  KOH solution at  $60 \text{ }^\circ\text{C}$  for 6 h decreased the Al/Ti atomic ratio in the Al/Ti-0.20 hollow spherical composite nanoassemblies from 13/100 to 4/100 without changing their morphology (Figure 2-18a). However, treatment with the  $1 \text{ mol L}^{-1}$  KOH solution for 24 h at  $25 \text{ }^\circ\text{C}$  completely destroyed the secondary structure of the hollow spherical composite nanoassemblies to permit the dispersion of the fine nanoparticles (Figure 2-18b). Interestingly, treatment with a  $0.5 \text{ mol L}^{-1}$  KOH solution for 24 h at  $25 \text{ }^\circ\text{C}$  opened the shells of the hollow nanoassemblies (Figure 2-18c), which could be used as a nanocontainer with a cap.

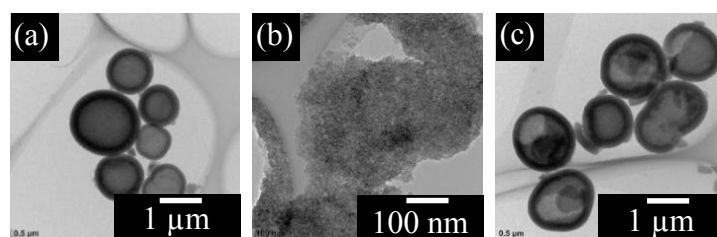


**Figure 2-18.** TEM images of Al/Ti-0.20 hollow spherical composite nanoassemblies etched in (a)  $1 \text{ mol L}^{-1}$  KOH at  $60 \text{ }^\circ\text{C}$  for 6 h, (b)  $1 \text{ mol L}^{-1}$  KOH at  $25 \text{ }^\circ\text{C}$  for 24 h, and (c)  $0.5 \text{ mol L}^{-1}$  KOH at  $25 \text{ }^\circ\text{C}$  for 24 h.

## 2-3 Conclusions

Hollow  $\text{Al}_2\text{O}_3\text{-TiO}_2$  and  $\text{ZnO-TiO}_2$  composite nanoassemblies were synthesized by a simple, single-step, one-pot, and template-free synthetic method.  $\text{Al}_2\text{O}_3\text{-TiO}_2$  composite nanoassemblies with aggregate (Al = 75%), fused hollow spherical (Al = 25–50%), and hollow spherical (Al = 5–20%) morphologies having a large specific surface area ( $240\text{--}600 \text{ m}^2 \text{ g}^{-1}$ ) were produced depending on the Al content in the precursor solutions. In the case of

ZnO–TiO<sub>2</sub>, solid spherical nanoassemblies and nanosheets mixtures (Zn = 75%), fused hollow spherical nanoassemblies (Zn = 50%), and hollow spherical nanoassemblies (Zn = 5–20%) were produced for different Zn contents in the precursor solutions. The atomic compositions of Al<sub>2</sub>O<sub>3</sub>–TiO<sub>2</sub> and ZnO–TiO<sub>2</sub> composites were effectively controlled by changing the mixing ratio of Al/Ti and Zn/Ti, respectively, in the precursor solutions. Hollow Al<sub>2</sub>O<sub>3</sub>–TiO<sub>2</sub> composite nanoassemblies with Al = 50% showed resistance to the anatase to rutile TiO<sub>2</sub> phase transition even at 1000 °C. Calcination at 1000 °C did not affect the hollow spherical morphology of the Al<sub>2</sub>O<sub>3</sub>–TiO<sub>2</sub> composite nanoassemblies with Al = 25–50%. The band gap energies of the calcinated hollow spherical ZnO–TiO<sub>2</sub> composite nanoassemblies were easily tuned by changing their Zn/Ti ratios. The alkaline etching of hollow spherical Al<sub>2</sub>O<sub>3</sub>–TiO<sub>2</sub> composite nanoassemblies resulted in the opening of their shells. Thus, mixing Al<sub>2</sub>O<sub>3</sub> or ZnO with TiO<sub>2</sub> at the nanoscopic level is a straightforward and sure approach to improve the inherent properties of TiO<sub>2</sub>, such as heat tolerance and band gap energy.

## **2-4 Experimental Section**

### **2-4-1 General information**

Methanol, phthalic acid, acetic acid, titanium tetraisopropoxide, zinc acetate dihydrate, and potassium hydroxide were purchased from Wako Pure Chemical Industries Co. Ltd. Aluminum triisopropoxide was purchased from Tokyo Chemical Industry Co. Ltd. These were used as received, without further purification.

### **2-4-2 Synthesis of Al<sub>2</sub>O<sub>3</sub>–TiO<sub>2</sub> and ZnO–TiO<sub>2</sub> composite nanoassemblies**

A portion of 3.5 mL of precursor solutions containing either Al(O<sup>i</sup>Pr)<sub>3</sub>/Ti(O<sup>i</sup>Pr)<sub>4</sub> or Zn(OAc)<sub>2</sub>·2H<sub>2</sub>O/Ti(O<sup>i</sup>Pr)<sub>4</sub> with 0.5 mol L<sup>-1</sup> phthalic acid (Tables 2-1 and 2-3) in methanol was transferred to a 10 mL-capacity SUS-316 stainless steel tubular reactor. The reactor was

sealed with a screw cap, placed in an electric oven, and heated to 300 °C at the rate of 5.4 °C min<sup>-1</sup>. The temperature was maintained at 300 °C for 10 min.<sup>[13–15]</sup> The reaction was quenched by placing the reactor in an ice-water bath. The resulting powdery products were centrifuged at 6600 rpm for 30 minutes, washed with methanol three times, and dried in vacuum.

### **2-4-3 Calcination of hollow composite nanoassemblies**

The hollow Al<sub>2</sub>O<sub>3</sub>–TiO<sub>2</sub> and ZnO–TiO<sub>2</sub> composite nanoassemblies were calcinated in a Yamato FO200 electric furnace at 500–1000 °C for 1 h with a heating rate of 10 °C min<sup>-1</sup>.

### **2-4-4 Chemical etching of hollow composite nanoassemblies**

A 20 mg amount of hollow Al<sub>2</sub>O<sub>3</sub>–TiO<sub>2</sub> composite assembly was suspended in 20 mL solution of 0.5 mol L<sup>-1</sup> KOH or 1 mol L<sup>-1</sup> KOH in a mixed solvent of 1:1 (v/v) methanol and deionized water at either 25 °C or 60 °C for 6–24 h. The suspension was centrifuged and the obtained precipitate was washed with a 1:1 (v/v) mixture of methanol and water three times, and dried in vacuum.

### **2-4-5 Characterization**

XRD patterns were obtained using a Rigaku SmartLab diffractometer with graphite-monochromated Cu K $\alpha$  radiation (X-ray wavelength: 0.15418 nm) in steps of 0.02° over the 2 $\theta$  range of 10–90°. TEM images and HRTEM images were measured on a JEOL JEM–2100F microscope. EDX mapping images were obtained from an Oxford INCA Energy TEM250. Nitrogen adsorption-desorption isotherms were obtained using a BEL Japan INC Belsorp Mini (II). UV-Vis absorption spectra (diffusion reflectance method) were obtained by JASCO UV-650 spectrophotometer equipped with an ISV-722 integration sphere.

## References

1. J. Hu, M. Chen, X. Fang, L. Wu, Fabrication and application of inorganic hollow spheres, *Chem. Soc. Rev.* **2011**, *40*, 5472–5491.
2. J. Lee, S. M. Kim, I. S. Lee, Functionalization of hollow nanoparticles for nanoreactor applications, *Nano Today* **2014**, *9*, 631–667.
3. H. Hu, L. Yu, X. Gao, Z. Lin, X. W. Lou, Hierarchical tubular structures constructed from ultrathin TiO<sub>2</sub>(B) nanosheets for highly reversible lithium storage, *Energy Environ. Sci.* **2015**, *8*, 1480–1483.
4. X.-Y. Yu, H. B. Wu, L. Yu, F.-X. Ma, X. W. Lou, Rutile TiO<sub>2</sub> submicroboxes with superior lithium storage properties, *Angew. Chem., Int. Ed.* **2015**, *54*, 4001–4004.
5. J. Jiang, Y. LI, J. Liu, X. Huang, C. Yuan, X. W. Lou, Recent advances in metal oxide-based electrode architecture design for electrochemical energy storage, *Adv. Mater.* **2012**, *24*, 5166–5180.
6. X. W. Lou, L. A. Archer, Z. Yang, Hollow micro-/nanostructures: synthesis and applications, *Adv. Mater.* **2008**, *20*, 3987–4019.
7. G. Xue, X. Huang, N. Zhao, F. Xiao, W. Wei, Hollow Al<sub>2</sub>O<sub>3</sub> spheres prepared by a simple and tunable hydrothermal method, *RSC Adv.* **2015**, *5*, 13385–13391.
8. Y. Li, J. Shi, Hollow-structured mesoporous materials: chemical synthesis, functionalization and applications, *Adv. Mater.* **2014**, *26*, 3176–3205.
9. R. Huang, Y. Liu, Z. Chen, D. Pan, Z. Li, M. Wu, C.-H. Shek, C. M. L. Wu, J. K. L. Lai, Fe-species-loaded mesoporous MnO<sub>2</sub> superstructural requirements for enhanced catalysis, *ACS Appl. Mater. Interfaces* **2015**, *7*, 3949–3959.
10. A. Bhaskar, M. Deepa, T. N. Rao, Size-controlled SnO<sub>2</sub> hollow spheres via a template free approach as anodes for lithium ion batteries, *Nanoscale* **2014**, *6*, 10762–10771.
11. Y. Liu, J. Goebel, Y. Yin, Templated synthesis of nanostructured materials, *Chem. Soc. Rev.* **2013**, *42*, 2610–2653.

12. S.-Y. Ryu, D. S. Kim, S.-D. Jeon, S.-Y. Kwak, Pore size distribution analysis of mesoporous TiO<sub>2</sub> spheres by <sup>1</sup>H nuclear magnetic resonance (NMR) cryoporometry, *J. Phys. Chem. C* **2010**, *114*, 17440–17445.
13. J. H. Bang, R. J. Helmich, K. S. Suslick, Nanostructured ZnS:Ni<sup>2+</sup> photocatalysts prepared by ultrasonic spray pyrolysis, *Adv. Mater.* **2008**, *20*, 2599–2603.
14. J. B. Joo, Q. Zhang, I. Lee, M. Dahl, F. Zaera, Y. Yin, Mesoporous anatase titania hollow nanostructures through silica-protected calcination, *Adv. Funct. Mater.* **2012**, *22*, 166–174.
15. J. Yu, J. Zhang, A simple template-free approach to TiO<sub>2</sub> hollow spheres with enhanced photocatalytic activity, *Dalton Trans.* **2010**, *39*, 5860–5867.
16. D. Li, Q. Qin, X. Duan, J. Yang, W. Guo, W. Zheng, General one-pot template-free hydrothermal method to metal oxide hollow spheres and their photocatalytic activities and lithium storage properties, *ACS Appl. Mater. Interfaces* **2013**, *5*, 9095–9100.
17. T. Ihara, H. Wagata, T. Kogure, K. Katsumata, K. Okada, N. Matsushita, Template-free solvothermal preparation of ZnO hollow microspheres covered with c planes, *RSC Adv.* **2014**, *4*, 25148–25154.
18. P. Wang, K. Kobihiro, Ultimately simple one-pot synthesis of spherical mesoporous TiO<sub>2</sub> nanoparticles in supercritical methanol, *Chem. Lett.* **2012**, *41*, 264–266.
19. P. Wang, K. Kobihiro, Synthetic versatility of nanoparticles: a new, rapid, one-pot, single-step synthetic approach to spherical mesoporous (metal) oxide nanoparticles using supercritical alcohols, *Pure Appl. Chem.* **2014**, *86*, 785–800.
20. P. Wang, K. Ueno, H. Takigawa, K. Kobihiro, Versatility of one-pot, single-step synthetic approach for spherical porous(metal) oxide nanoparticles using supercritical alcohols, *J. Supercrit. Fluids* **2013**, *78*, 124–131.
21. P. Wang, K. Yokoyama, T. Konishi, N. Nishiwaki, K. Kobihiro, Ultimately simple one-pot single-step synthesis of rare earth doped spherical mesoporous metal oxide nanospheres with upconversion emission ability in supercritical methanol, *J. Supercrit. Fluids* **2013**, *80*, 71–77.

22. P. Wang, H. Tooriyama, K. Yokoyama, M. Ohtani, H. Asahara, T. Konishi, N. Nishiwaki, M. Shimoda, Y. Yamashita, H. Yoshikawa, K. Kobiro, Smart decoration of mesoporous TiO<sub>2</sub> nanospheres with noble metal alloy nanoparticles into core–shell, yolk–core–shell, and surface-dispersion morphologies, *Eur. J. Inorg. Chem.* **2014**, *26*, 4254–4257.
23. N. Bayal, P. Jeevanandam, Smart decoration of mesoporous TiO<sub>2</sub> nanospheres with noble metal alloy nanoparticles into core–shell, yolk–core–shell, and surface-dispersion morphologies, *Ceram. Int.* **2014**, *40*, 15463–15477.
24. N. Dejang, A. Watcharapasorn, S. Wirojupatump, P. Niranatlumpong, S. Jiansirisomboon, Fabrication and properties of plasma-sprayed Al<sub>2</sub>O<sub>3</sub>/TiO<sub>2</sub> composite coatings: A role of nano-sized TiO<sub>2</sub> addition, *Surf. Coat. Technol.* **2010**, *204*, 1651–1657.
25. M. Agrawal, S. Gupta, A. Pich, N. E. Zafeiropoulos, M. Stamm, A facile approach to fabrication of ZnO–TiO<sub>2</sub> hollow spheres, *Chem. Mater.* **2009**, *21*, 5343–5348.
26. P. Vlazan, D. H. Ursu, C. I. Moisescu, I. Miron, P. Sfirloaga, E. Rusu, Structural and electrical properties of TiO<sub>2</sub>/ZnO core–shell nanoparticles synthesized by hydrothermal method, *Mater. Charact.* **2015**, *101*, 153–158.
27. S. T. Wang, M. Y. Wang, X. Su, B. F. Yuan, Y. Q. Feng, Facile preparation of SiO<sub>2</sub>/TiO<sub>2</sub> composite monolithic capillary column and its application in enrichment of phosphopeptides, *Anal. Chem.* **2012**, *84*, 7763–7770.
28. S. Luo, T.-D. N.-Phan, A. C. J.-Peck, L. Barrio, S. Sallis, D. A. Arena, S. Kundu, W. Xu, L. F. J. Piper, E. A. Stach, D. E. Polyansky, E. Fujita, J. A. Rodriguez, S. D. Senanayake, Hierarchical heterogeneity at the CeO<sub>x</sub>–TiO<sub>2</sub> interface: electronic and geometric structural influence on the photocatalytic activity of oxide on oxide nanostructures, *J. Phys. Chem. C* **2015**, *119*, 2669–2679.
29. A. Attia, M. Zulkalová, J. Rathouský, A. Zukal, L. Kavan. Mesoporous electrode material from alumina-stabilized anatase TiO<sub>2</sub> for lithium ion batteries, *J. Solid State Electrochem.* **2005**, *9*, 138–145.
30. S. Perera, G. E. Gillan, High-temperature stabilized anatase TiO<sub>2</sub> from an aluminum-doped TiCl<sub>3</sub> precursor, *Chem. Commun.* **2005**, 5988–5990.

31. J. Y. Kim, S. H. Kang, H. S. Kim, Y. E. Sung, Preparation of highly ordered mesoporous Al<sub>2</sub>O<sub>3</sub>/TiO<sub>2</sub> and its application in dye-sensitized solar cells, *Langmuir* **2010**, *26*, 2864–2870.
32. Z. Zhou, T. Zeng, Z. Cheng, W. Yuan, Preparation of highly ordered mesoporous Al<sub>2</sub>O<sub>3</sub>/TiO<sub>2</sub> and its application in dye-sensitized solar cells, *Ind. Eng. Chem. Res.* **2011**, *50*, 883–890.
33. R. Vyas, S. Sharma, P. Gupta, Y. K. Vijay, A. K. Prasad, A. K. Tyagi, K. Sachdev, S. K. Sharma, Enhanced NO<sub>2</sub> sensing using ZnO–TiO<sub>2</sub> nanocomposite thin films, *J. Alloys Compd.* **2013**, *554*, 59–63.
34. T. A. Arun, A. A. Madhavan, D. K. Chacko, G. S. Anjusree, T. G. Deepak, S. Thomas, S. V. Nair, A. S. Nair, Preparation of highly ordered mesoporous Al<sub>2</sub>O<sub>3</sub>/TiO<sub>2</sub> and its application in dye-sensitized solar cells, *Dalton Trans.* **2014**, *43*, 4830–4837.
35. V. Manthina, J. P. C. Baena, G. Liu, A. G. Agrios, ZnO–TiO<sub>2</sub> nanocomposite films for high light harvesting efficiency and fast electron transport in dye-sensitized solar cells, *J. Phys. Chem. C* **2012**, *116*, 23864–23870.
36. C. Bousquet, C. Elissalde, C. Aymonier, M. Maglione, F. Cansell, J. M. Heintz, Tuning Al<sub>2</sub>O<sub>3</sub> crystallinity under supercritical fluid conditions: effect on sintering, *J. Eur. Ceram. Soc.* **2008**, *28*, 223–228.
37. W.-L. Xiong, Q.-Y. Liu, N. Zhang, L. Wang, A two-dimensional coordination polymer containing a two-dimensional zinc–carboxylate layer constructed from helical chains: poly[(μ<sup>4</sup>-benzene-1,2-dicarboxylato)zinc(II)], *Acta. Cryst. C* **2012**, *C68*, m235–m237.
38. M. Dahl, Y. Liu, Y. Yin, Composite titanium dioxide nanomaterials, *Chem. Rev.* **2014**, *114*, 9853–9889.
39. X. Yan, L. Feng, J. Jia, X. Zhou, Y. Lin, Controllable synthesis of anatase TiO<sub>2</sub> crystals for high-performance dye-sensitized solar cells, *J. Mater. Chem. A* **2013**, *1*, 5347–5352.

40. K. Lee, D. Kim, P. Roy, I. Paramasivam, B. I. Birajdar, E. Spiecker, P. Schmuki, Anodic formation of thick anatase TiO<sub>2</sub> mesosponge layers for high-efficiency photocatalysis, *J. Am. Chem. Soc.* **2010**, *132*, 1478–1479.
41. D. A. H. Hanaor, C. C. Sorell, Review of the anatase to rutile phase transformation, *J. Mater. Sci.* **2011**, *46*, 855–874.
42. S. Guo, H. Yoshioka, H. Kakehi, Y. Kato, M. Miura, N. Isu, B. Ameduri, H. Sawada, Fluoroalkyl end-capped vinyltrimethoxysilane oligomer/anatase titanium oxide nanocomposites possessing photocatalytic activity even after calcination at 1000 °C, *J. Colloid Interface Sci.* **2012**, *387*, 141–145.
43. W. Li, C. Ni, H. Lin, C. P. Huang, S. I. Shah, Size dependence of thermal stability of TiO<sub>2</sub> nanoparticles, *J. Appl. Phys.* **2004**, *96*, 6663–6668.
44. S. C. Pillai, P. Periyat, R. George, D. E. McCormack, M. K. Seery, H. Hayden, J. Colreavy, D. Corr, S. J. Hinder, Synthesis of high-temperature stable anatase TiO<sub>2</sub> photocatalyst, *J. Phys. Chem. C* **2007**, *111*, 1605–1611.
45. J. Yang, J. M. F. Ferreira, Synthesis of high-temperature stable anatase TiO<sub>2</sub> photocatalyst, *Mater. Lett.* **1998**, *36*, 320–324.
46. J. Wang, H. Sun, J. Huang, Q. Li, J. Yang, Band structure tuning of TiO<sub>2</sub> for enhanced photoelectrochemical water splitting, *J. Phys. Chem. C* **2014**, *118*, 7451–7457.
47. A. Arunachalam, S. Dhanapandian, C. Manoharan, G. Sivakumar, Physical properties of Zn doped TiO<sub>2</sub> thin films with spray pyrolysis technique and its effects in antibacterial activity, *Spectrochim. Acta, Part A* **2012**, *138*, 105–112.
48. J. Tauc, R. Grigorovici, A. Vancu, Optical properties and electronic structure of amorphous germanium, *Phys. Status Solidi* **1966**, 627–637.
49. T. G. Pedersen, Quantum size effects in ZnO nanowires, *Phys. Status Solidi C* **2005**, *2*, 4026–4030.

## Chapter 3.

# Ultra-simple synthetic approach to the fabrication of CeO<sub>2</sub>–ZrO<sub>2</sub> mixed nanoassemblies into homogeneous, domain, and core-shell structures in mesoporous spherical morphologies using high-temperature and high-pressure alcohols

### 3-1 Introduction

Much attention has been paid to CeO<sub>2</sub> nanomaterials for their many practical uses, such as three-way catalysts for exhaust gas treatment,<sup>[1,2]</sup> noble metal catalyst supports,<sup>[3,4]</sup> and surface lapping and polishing materials.<sup>[5,6]</sup> However, decreasing the required amount of the rare earth metal Ce without losing the performance of the material has become a crucial aspect of current research because of resource limitations.<sup>[6–8]</sup> As a practical approach for minimizing Ce loading on nanomaterials, CeO<sub>2</sub>–ZrO<sub>2</sub> composites can be used as a substitute because of their chemical, mechanical, and thermal stability. Moreover, some of CeO<sub>2</sub>–ZrO<sub>2</sub> mixed oxides have been reported to show better catalytic performance compared to CeO<sub>2</sub> itself.<sup>[9]</sup> Previously, fabrication of CeO<sub>2</sub>, ZrO<sub>2</sub>, and CeO<sub>2</sub>–ZrO<sub>2</sub> composites has been accomplished through several techniques, for example by using sacrificial templates such as polymers,<sup>[10]</sup> colloidal carbon,<sup>[11]</sup> and silica<sup>[12]</sup> and by calcination of MOFs,<sup>[13,14]</sup> to yield higher-order spherical, core-shell, tube, and cubic morphologies. In order to achieve high performance, controlling the composition, topology, and morphology of CeO<sub>2</sub>–ZrO<sub>2</sub> composites at the nano level is very important. To this end, much effort has been applied towards the development of synthetic methodologies to control their structures and morphologies; these include sol-gel,<sup>[15,16]</sup> precipitation,<sup>[17,18]</sup> microemulsion,<sup>[19]</sup> hydrothermal,<sup>[20,21]</sup> supercritical solvent,<sup>[22]</sup> high-temperature solid state reaction,<sup>[23]</sup> high-energy mechanical mixing,<sup>[24]</sup> and flame spray<sup>[25]</sup> methods. However, multi-step reactions

that include calcination, as well as a long reaction time, are usually required to obtain higher-ordered nanomaterials such as spherical, cubic, and multi-layered structures.

Well-defined porous nanomaterials are also essential for practical applications including high-throughput catalysis,<sup>[26]</sup> high performance lapping and polishing,<sup>[7]</sup> and excellent ion conduction.<sup>[27]</sup> To this end, MARIMO nanoassemblies synthesized by Wang's ultimately simple method show almost complete spherical morphology in solid and hollow structures, well-defined pore topology, large surface area, mono-dispersion ability, excellent thermal stability, and easy manipulation,<sup>[28]</sup> which would be promising functional materials for many applications, such as catalysis, lapping and polishing, material storage and slow release, drug and gene delivery, and solar energy conversion, etc.

Given the importance of  $\text{CeO}_2\text{-ZrO}_2$  as a functional material and our rapid synthetic approach to MARIMO nanoassemblies using high-temperature and high-pressure alcohols as the reaction media, high-temperature and high-pressure alcohol based, ultra-simple, and rapid synthetic approach to  $\text{CeO}_2\text{-ZrO}_2$  composites nanoassemblies with homogeneously mixed, domain, and double-layered core-shell structures with mesoporous spherical morphologies is reported in this chapter (Figure 3-1).

## **3-2 Results and discussion**

### **3-2-1 Single-step one-pot synthesis of homogeneously well dispersed mesoporous spherical $\text{Ce}_x\text{Zr}_{1-x}\text{O}_2$ composite nanoassemblies and mesoporous spherical $\text{CeO}_2\text{-ZrO}_2$ composite nanoassemblies with domain structures**

Recently, an ultimately simple, rapid, and template-free fabrication strategy for  $\text{CeO}_2$  MARIMO nanoassemblies and  $\text{ZrO}_2$  MARIMO nanoassemblies was developed, in which a precursor solution of  $\text{Ce}(\text{NO}_3)_3$  or  $\text{ZrO}(\text{NO}_3)_2$  and formic acid in methanol was rapidly heated (at a rate of  $500\text{ }^\circ\text{C}/\text{min}$ ) to  $300\text{ }^\circ\text{C}$  in a sealed SUS-316 tubular reactor and maintained at the temperature only for 10 min.<sup>[28]</sup> It is noteworthy that the recently developed strategy did not

require calcination to obtain MARIMO nanoassemblies. In this chapter, the synthesis of mesoporous spherical  $\text{CeO}_2\text{-ZrO}_2$  composite nanoassemblies by a similar approach with precursor solutions containing a mixture of Ce and Zr salts is described.

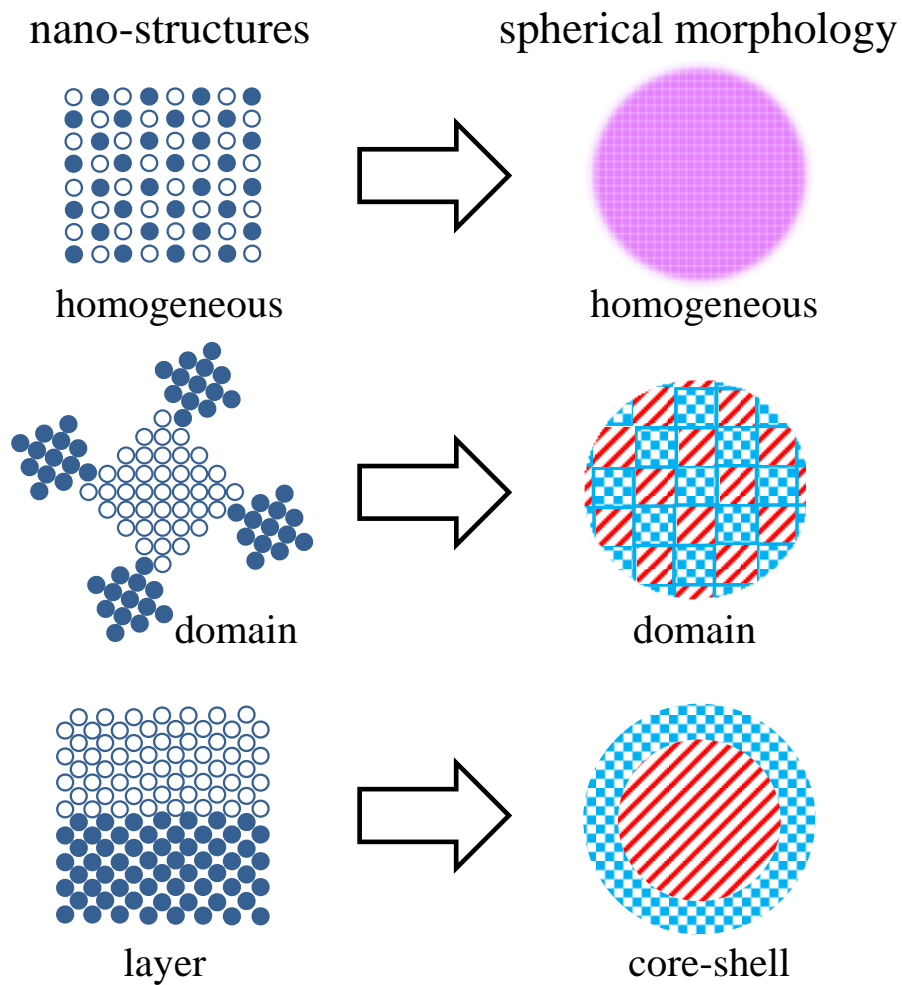


**Figure 3-1.** Schematic of material design structures of composite metal oxides nanoassemblies (● and ○ represent different primary nanoparticles).

**Table 3-1.** Molarity and molar portion of Ce and Zr species in precursor solutions.

Sample name <sup>a</sup>	Precursor solution (mol L <sup>-1</sup> )		
	Ce(NO <sub>3</sub> ) <sub>3</sub>	ZrO(NO <sub>3</sub> ) <sub>2</sub>	Ce/Zr ratio
ZrO <sub>2</sub>	-	0.05	0
Ce/ZrO <sub>2</sub> -0.25	0.05	0.15	0.25/0.75
Ce/ZrO <sub>2</sub> -0.33	0.05	0.10	0.33/0.66
Ce/ZrO <sub>2</sub> -0.50	0.05	0.05	0.50/0.50
Ce/ZrO <sub>2</sub> -0.66	0.10	0.05	0.66/0.33
CeO <sub>2</sub>	0.05	-	1

<sup>a</sup> The numbers 0.25, 0.33, 0.50, and 0.66 designate molar portion of  $[\text{Ce}^{3+}]/([\text{Ce}^{3+}] + [\text{Zr}^{4+}])$

in the precursor solution.

**Table 3-2.** BET specific surface area and BJH pore diameter of mesoporous spherical Ce/ZrO<sub>2</sub> composite nanoassemblies.

Sample name	Particle diameter (nm) <sup>a</sup>	BET specific surface area (m <sup>2</sup> g <sup>-1</sup> )	BJH pore diameter (nm)
ZrO <sub>2</sub>	360±115	118	0.4 <sup>b</sup>
CeZrO <sub>2</sub> -0.25	350±161	152	4.7
CeZrO <sub>2</sub> -0.33	340±157	134	4.2
CeZrO <sub>2</sub> -0.50	290±104	103	4.8
CeZrO <sub>2</sub> -0.66	210±52	92	4.4
CeO <sub>2</sub>	245±134	32	4.8

<sup>a</sup> Average of at least randomly chosen 50 nanoassemblies in a SEM image.

<sup>b</sup> Calculated by *t*-method.

Indeed, upon rapid heating of the precursor solutions containing Ce(NO<sub>3</sub>)<sub>3</sub> and ZrO(NO<sub>3</sub>)<sub>2</sub> in different molar ratios (Table 3-1) with formic acid in methanol at 300 °C, beautiful spherical porous nanoassemblies were obtained (Figure 3-2), in which many small primary particles assembled to give a secondary spherical structure with a large amount of pores, as shown in TEM and scanning electron microscopy (SEM) images. These spherical composite nanoassemblies referred to as Ce/ZrO<sub>2</sub>-0.25, Ce/ZrO<sub>2</sub>-0.33, Ce/ZrO<sub>2</sub>-0.50, Ce/ZrO<sub>2</sub>-0.66, where the number designates the molar portion  $[\text{Ce}^{3+}]/([\text{Ce}^{3+}] + [\text{Zr}^{4+}])$  in the precursor solution. The average diameters of the spherical composite nanoassemblies were similar, ranging from 200 to 350 nm, irrespective of the molar ratio of Ce and Zr in the

precursor solution (Table 3-2). However, the size of the primary nanoparticles varied with the molar ratio of Ce and Zr, from 3–10 nm as can be seen in TEM and HRTEM images in Figure 3-2. EDX analyses on TEM clearly indicate that Ce, Zr, and O atoms are evenly distributed in spherical composite nanoassemblies (Figure 3-3). Specific surface areas and pore sizes of the spherical composite nanoassemblies were evaluated by nitrogen adsorption-desorption isotherms (Table 3-2 and Figure 3-4). The ZrO<sub>2</sub> MARIMO nanoassemblies produced a type I isotherm, indicating the existence of micropores (<2 nm), while the isotherms of Ce/ZrO<sub>2</sub> spherical composite nanoassemblies and CeO<sub>2</sub> itself belong to the type IV category, indicating the existence of mesoporous (2–50 nm). Moreover, pure ZrO<sub>2</sub>, Ce/ZrO<sub>2</sub>-0.25, Ce/ZrO<sub>2</sub>-0.33, and Ce/ZrO<sub>2</sub>-0.50 showed similar specific surface areas of around 100 m<sup>2</sup> g<sup>-1</sup>, though Ce/ZrO<sub>2</sub>-0.66 with its higher Ce content and CeO<sub>2</sub> itself had smaller specific areas of 91 and 32 m<sup>2</sup> g<sup>-1</sup> respectively, whose results are consistent with those of the HRTEM images (Figure 3-2).

In order to obtain information of the crystal systems, XRD patterns of 1:2 (w/w) mixture of CeO<sub>2</sub> MARIMO and ZrO<sub>2</sub> MARIMO (Figure 3-5), pure CeO<sub>2</sub> MARIMO, pure ZrO<sub>2</sub> MARIMO, and the spherical CeO<sub>2</sub>-ZrO<sub>2</sub> composite nanoassemblies (Figure 3-6) were recorded. The pure CeO<sub>2</sub> MARIMO nanoassemblies exhibited the cubic phase. Although states of tetragonal and monoclinic phases are quite usual in ZrO<sub>2</sub>,<sup>[29–31]</sup> it is noteworthy that our ZrO<sub>2</sub> MARIMO nanoassemblies exhibited only the tetragonal phase. In the case of the 1:2 simple mixtures of CeO<sub>2</sub> MARIMO nanoassemblies and ZrO<sub>2</sub> MARIMO nanoassemblies, a mixed profile derived from those of pure CeO<sub>2</sub> and ZrO<sub>2</sub> was obtained, while the intensity ratio between CeO<sub>2</sub> and ZrO<sub>2</sub> did not reflect the original ratio of 2:1, but rather roughly estimated as 10:1. This provides an important indication of XRD response factors of CeO<sub>2</sub> MARIMO nanoassemblies and ZrO<sub>2</sub> MARIMO nanoassemblies in a mixture. Broad peaks

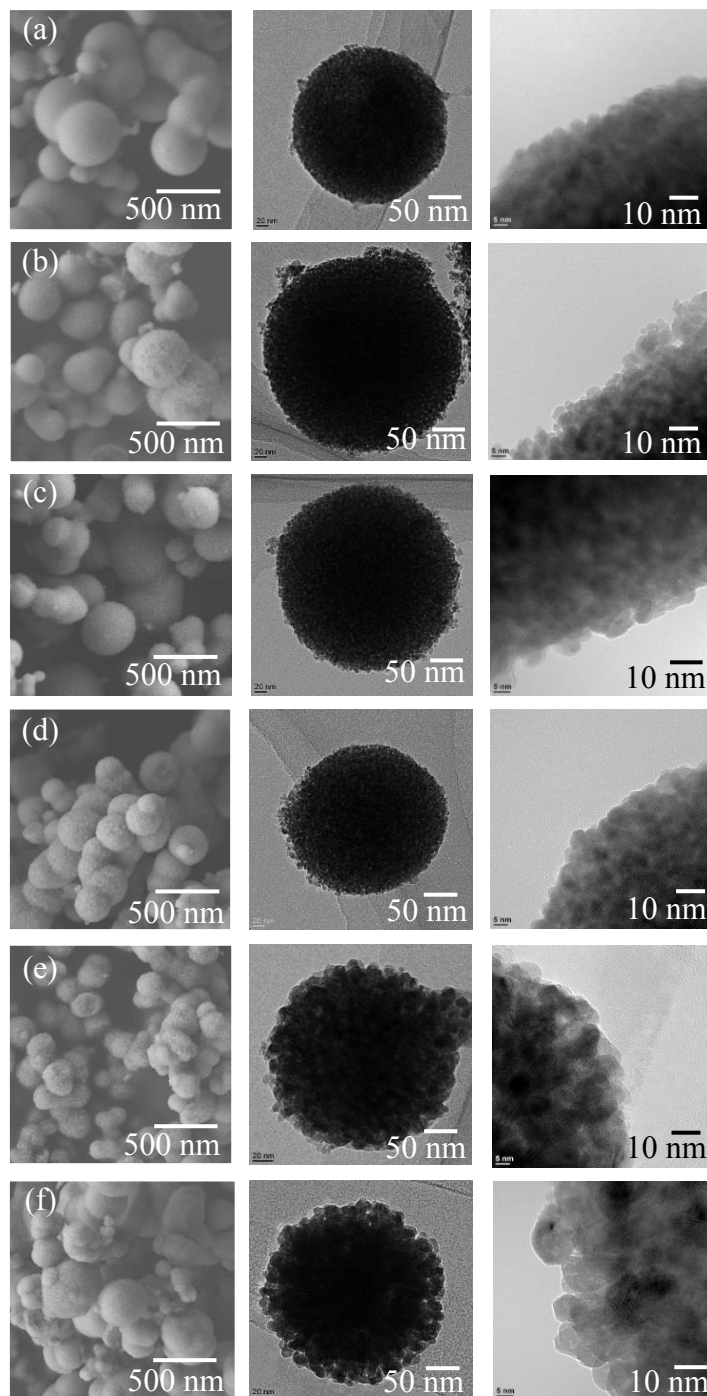


**Figure 3-2.** SEM (left), TEM (center) and HRTEM (right) images of spherical nanoassemblies: (a)  $\text{ZrO}_2$ , (b)  $\text{Ce}/\text{ZrO}_2\text{-}0.25$ , (c)  $\text{Ce}/\text{ZrO}_2\text{-}0.33$ , (d)  $\text{Ce}/\text{ZrO}_2\text{-}0.50$ , (e)  $\text{CeZrO}_2\text{-}0.66$ , and (f)  $\text{CeO}_2$ .

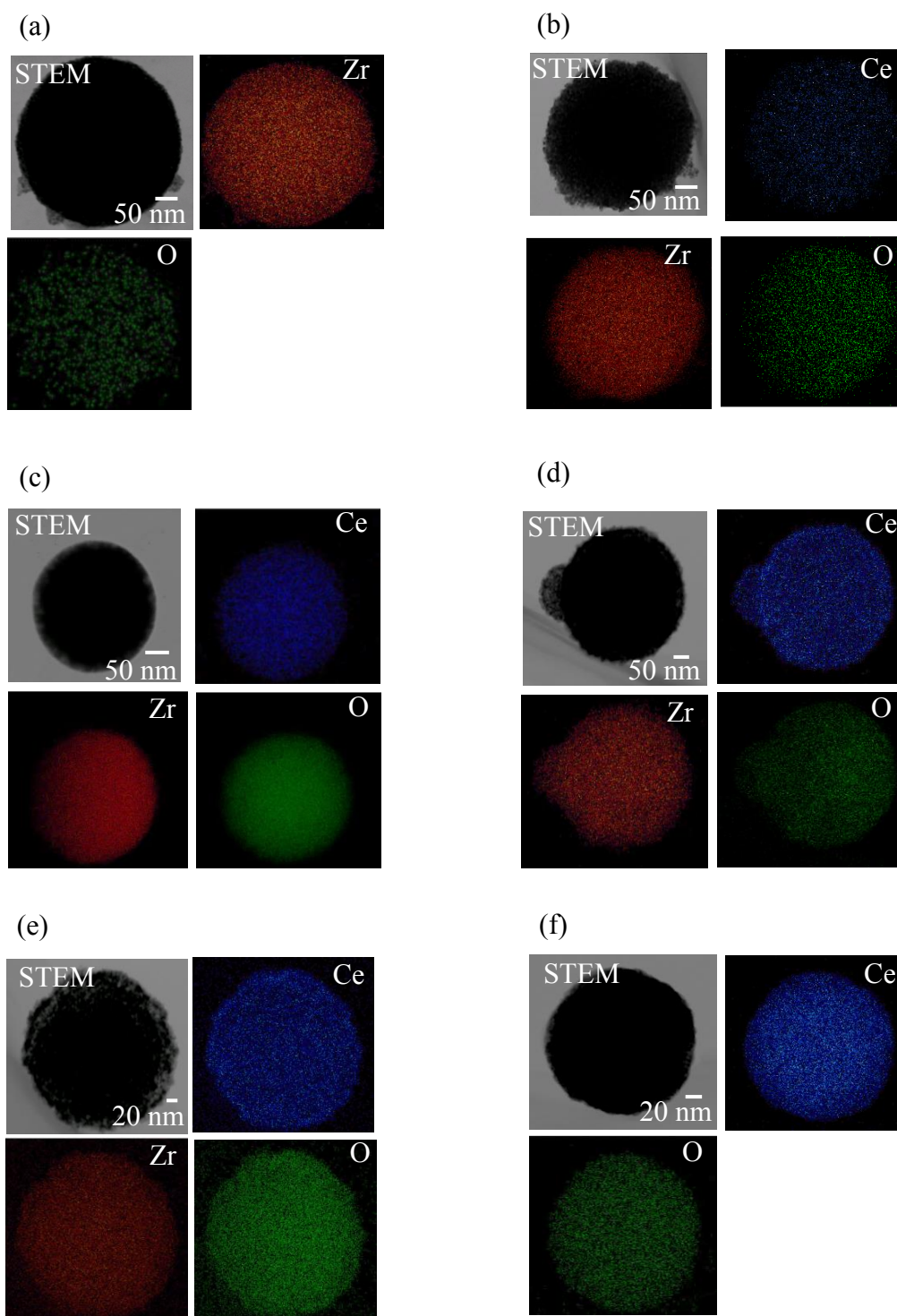


**Figure 3-3.** STEM and EDX mapping images of spherical nanoassemblies: (a)  $\text{ZrO}_2$ , (b)  $\text{Ce/ZrO}_2\text{-}0.25$  (c)  $\text{Ce/ZrO}_2\text{-}0.33$ , (d)  $\text{Ce/ZrO}_2\text{-}0.50$ , (e)  $\text{Ce/ZrO}_2\text{-}0.66$ , and (f)  $\text{CeO}_2$ .

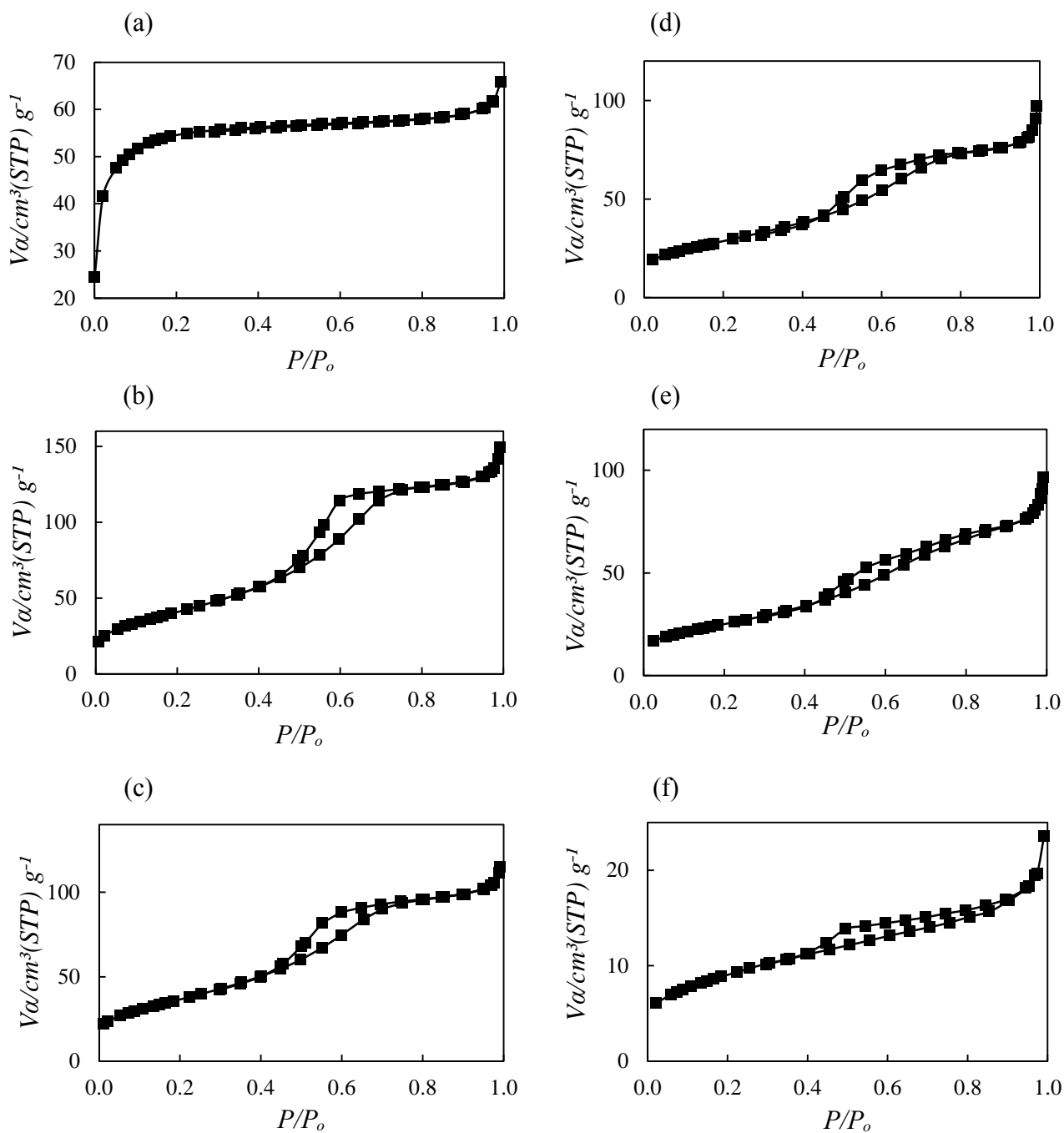


**Figure 3-4.** Nitrogen adsorption-desorption isotherms of spherical nanonanoassemblies: (a)  $\text{ZrO}_2$ , (b)  $\text{Ce/ZrO}_2\text{-0.25}$  (c)  $\text{Ce/ZrO}_2\text{-0.33}$ , (d)  $\text{Ce/ZrO}_2\text{-0.50}$ , (e)  $\text{Ce/ZrO}_2\text{-0.66}$ , and (f)  $\text{CeO}_2$ .

which appeared in the XRD of ZrO<sub>2</sub> MARIMO nanoassemblies (Figure 3-6a) clearly indicate that the primary particle size of the ZrO<sub>2</sub> MARIMO nanoassemblies should be small, a result which is also supported by the pore size as determined by their nitrogen absorption-desorption isotherms (Table 3-2). XRD patterns of spherical Ce/ZrO<sub>2</sub> composite nanoassemblies did not show diffraction peaks corresponding to either cubic CeO<sub>2</sub> or tetragonal ZrO<sub>2</sub>, instead diffraction peaks positions of Ce/ZrO<sub>2</sub> composites were situated between those of cubic CeO<sub>2</sub> and tetragonal ZrO<sub>2</sub> (Figure 3-6) indicating the formation of homogeneously mixed Ce<sub>x</sub>Zr<sub>1-x</sub>O<sub>2</sub>. It is remarkable that XRD peak positions and lattice parameters of Ce/ZrO<sub>2</sub> composite nanoassemblies were continuously shifted from

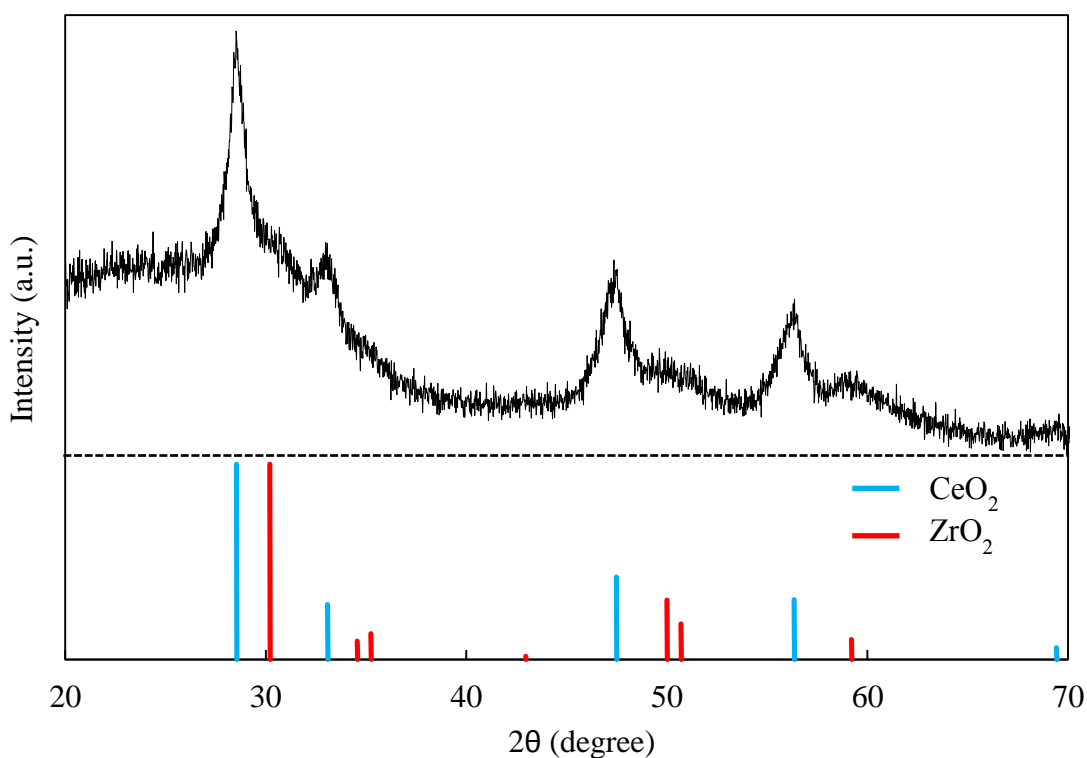


**Figure 3-5.** XRD patterns of 1:2 (*w/w*) mixture of CeO<sub>2</sub> MARIMO and ZrO<sub>2</sub> MARIMO nanoassemblies (peak positions of cubic CeO<sub>2</sub> and tetragonal ZrO<sub>2</sub> are shown with blue and red lines, respectively).

those of  $\text{CeO}_2$  to  $\text{ZrO}_2$ , depending on the Ce/Zr ratio in the precursor solution (Figure 3-6 and 3-7), which is the well-known phenomenon described by Vegard's law.<sup>[32]</sup> Judging from the results of the XRD,  $\text{CeO}_2$  and  $\text{ZrO}_2$ , whose crystal sizes would be quite small, were homogeneously mixed in XRD detection level. However, spherical  $\text{CeO}_2$ - $\text{ZrO}_2$ -SH (where SH denotes Slow Heating) composite nanoassemblies which were synthesized by a slow heating approach exhibited a mixed profile of cubic  $\text{CeO}_2$  and tetragonal  $\text{ZrO}_2$  phases on the XRD patterns (Figure 3-8), while Ce, Zr, and O atoms were evenly distributed on EDX images (Figure 3-9). The results clearly indicate that the obtained spherical composite nanoassemblies consisting of domain structure with cubic  $\text{CeO}_2$  and tetragonal  $\text{ZrO}_2$ . The difference in the structures is explained as follows: in the case of rapid heating, almost all of the precursor Ce and Zr salts are hydrolyzed very quickly as to afford large amount of nascent nanoparticles of  $\text{CeO}_2$  and  $\text{ZrO}_2$  to be present at same time. However, the nascent nanoparticles have no chance to grow up to an appreciable size, since almost all starting materials have been already consumed at the high temperature through rapid heating; instead the nascent nanoparticles of  $\text{CeO}_2$  and  $\text{ZrO}_2$  mix together to yield homogeneously mixed mesoporous spherical  $\text{Ce}_x\text{Zr}_{1-x}\text{O}_2$  composite nanoassemblies (Figure 3-10). On the other hand, in the case of slow heating, the  $\text{CeO}_2$  and  $\text{ZrO}_2$  nascent nanoparticles yielded at the early stage of heating individually grow up to an appropriate crystal size, since there is a continuous supply of the  $\text{Ce}^{3+}$  and  $\text{Zr}^{4+}$  ions from the remaining starting materials (Figure 3-10). Thus, we succeeded in synthesizing homogeneously mixed mesoporous spherical  $\text{Ce}_x\text{Zr}_{1-x}\text{O}_2$  composite nanoassemblies as well as mesoporous spherical  $\text{CeO}_2$ - $\text{ZrO}_2$  composite nanoassemblies with domain structures using our ultimately simple one-pot synthesis with high-temperature and high-pressure methanol, employing different heating rates, and without calcination.

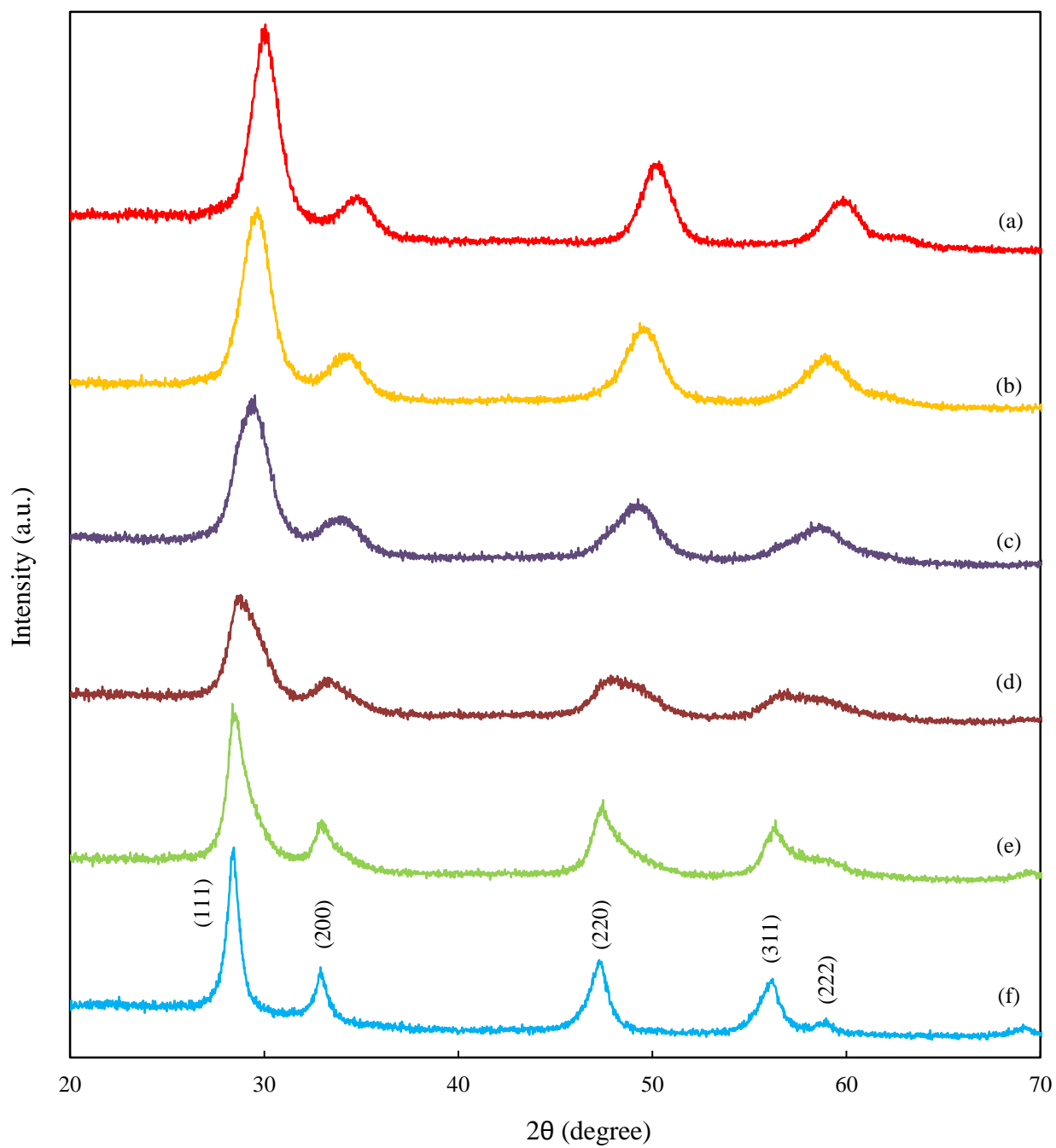


**Figure 3-6.** XRD patterns of spherical nanoassemblies: (a)  $\text{ZrO}_2$ , (b)  $\text{Ce/ZrO}_2\text{-}0.25$ , (c)  $\text{Ce/ZrO}_2\text{-}0.33$ , (d)  $\text{Ce/ZrO}_2\text{-}0.50$ , (e)  $\text{Ce/ZrO}_2\text{-}0.66$ , and (f)  $\text{CeO}_2$ .

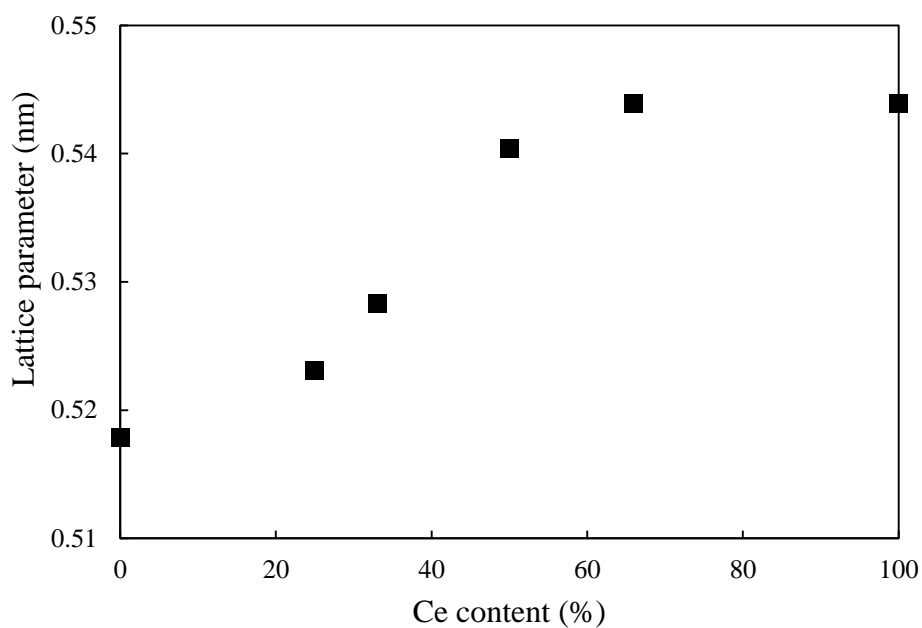


**Figure 3-7.** Lattice parameter versus Ce content in precursor solution.

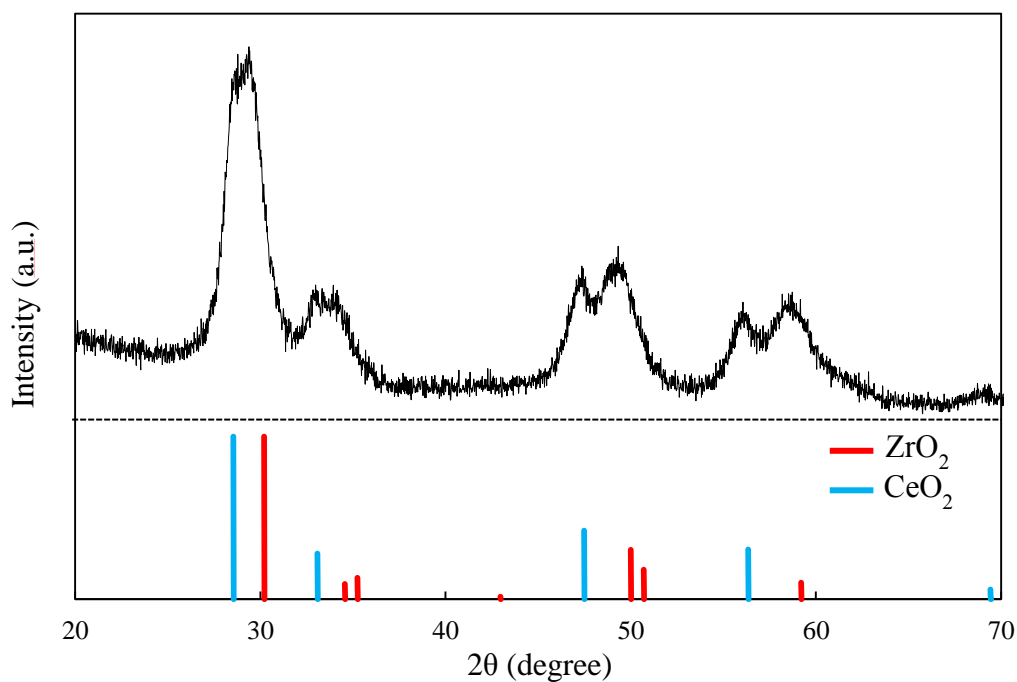


**Figure 3-8.** XRD patterns of spherical  $\text{CeO}_2\text{-ZrO}_2\text{-SH}$  composite nanoassemblies (peak positions of cubic  $\text{CeO}_2$  and tetragonal  $\text{ZrO}_2$  are shown with blue and red lines, respectively).

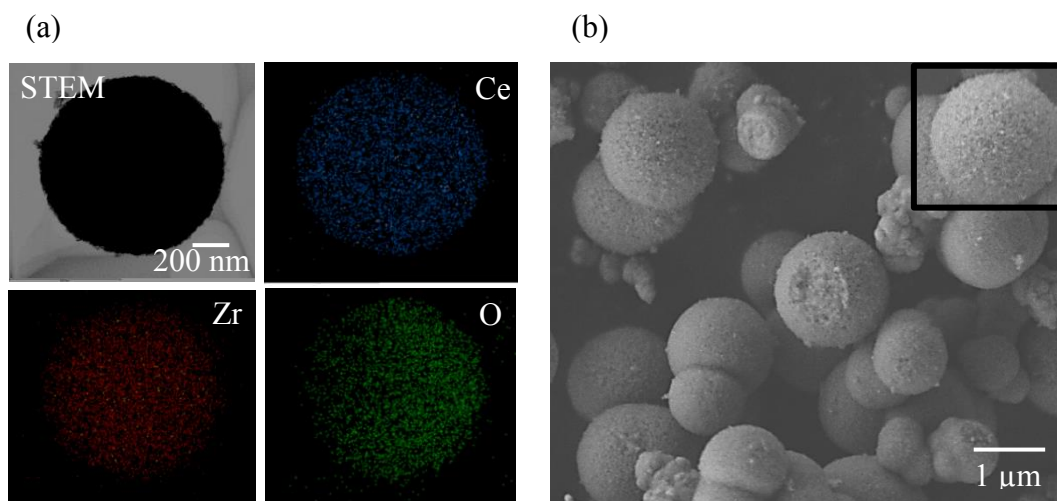


**Figure 3-9.** STEM and EDX mapping images (a) and SEM image (b) of spherical CeO<sub>2</sub>-ZrO<sub>2</sub>-SH composite nanoassemblies.

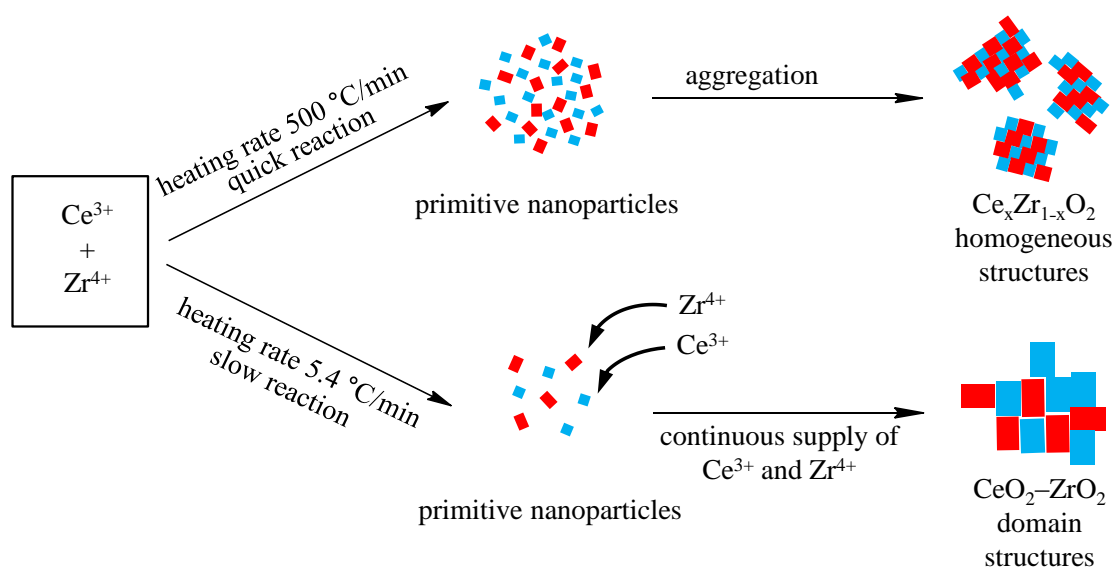


**Figure 3-10.** Schematic illustration of the reaction mechanism leading to homogeneously mixed Ce<sub>x</sub>Zr<sub>1-x</sub>O<sub>2</sub> composite nanoassemblies and CeO<sub>2</sub>-ZrO<sub>2</sub> composite nanoassemblies with domain structures (■ and ■ represent primitive nanoparticles of CeO<sub>2</sub> and ZrO<sub>2</sub>, respectively).

### 3-2-2 Synthesis of $\text{ZrO}_2@\text{CeO}_2$ core-shell nanoassemblies by a step-wise approach in high-temperature and high-pressure alcohols

A step-wise synthetic approach was applied to obtain  $\text{ZrO}_2@\text{CeO}_2$  core-shell nanoassemblies with a  $\text{ZrO}_2$  core and a  $\text{CeO}_2$  shell (Figure 3-1). Treatment of mesoporous spherical  $\text{ZrO}_2$  nanoassemblies with  $\text{Ce}(\text{NO}_3)_3$  in supercritical methanol at 300 °C for 10 min under  $0.28 \text{ g mL}^{-1}$  methanol density yielded a powdery product (referred to as  $\text{ZrO}_2@\text{CeO}_2\text{-MeOH}$ ). The XRD diffraction pattern of the obtained material revealed broad peaks with mixed profiles of  $\text{ZrO}_2$  tetragonal and  $\text{CeO}_2$  cubic phases, indicating they are not homogeneously mixed, but rather a mixture of  $\text{ZrO}_2$  and  $\text{CeO}_2$  with tetragonal and cubic phases, respectively (Figure 3-11). EDX mappings images clearly show that two types of spherical composite nanoassemblies were included, i.e. (i) spherical composite nanoassemblies consisting of Zr, O, and a small amount of Ce atoms ( $\text{ZrO}_2@\text{CeO}_2$  with thin-shell, Figure 3-12a) and (ii) core-shell type spherical composite nanoassemblies ( $\text{ZrO}_2@\text{CeO}_2$  with thick-shell Figure 3-12b) with  $\text{ZrO}_2$  core and  $\text{CeO}_2$  shell; the ratio (i) : (ii) is roughly estimated to be 10:1 by counting the numbers of the particles on the EDX images. In case (i), judging from the fact that  $\text{ZrO}_2$  MARIMO nanoassemblies show relatively weak intensities on the XRD patterns as mention above, we concluded that starting microporous  $\text{ZrO}_2$  MARIMO nanoassemblies in the tetragonal phase are covered by very thin shell of  $\text{CeO}_2$  in the cubic phase as schematically illustrated in Figure 3-13. Interestingly, when formic acid was used as an additive in this reaction, a mixture of independent spherical  $\text{ZrO}_2$  nanoassemblies covered by a very thin  $\text{CeO}_2$  shell and spherical  $\text{CeO}_2$  nanoassemblies themselves was obtained.

Then the solvent was changed as an attempt to produce a thicker outer-shell of cubic  $\text{CeO}_2$ , since some of secondary alcohols are reported to yield larger size crystalline  $\text{CeO}_2$  particles.<sup>[33]</sup> Indeed, when the reaction was performed in 2-propanol instead of methanol, the

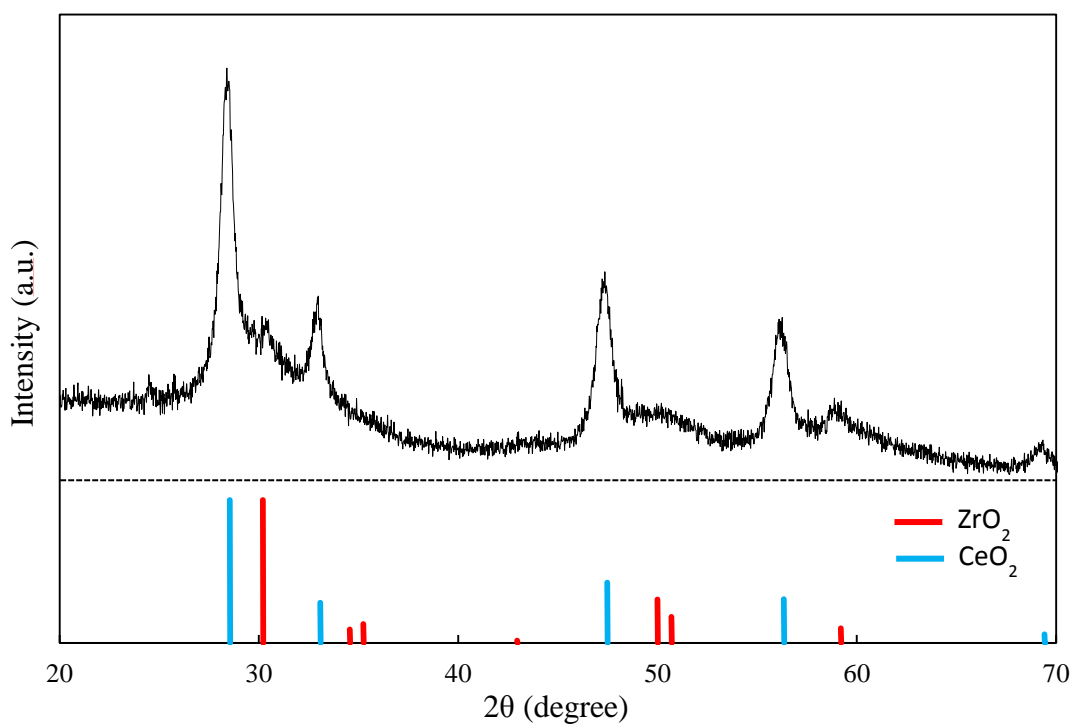


**Figure 3-11.** XRD patterns of  $\text{ZrO}_2@\text{CeO}_2\text{-MeOH}$  core-shell nanoassemblies (peak positions of cubic  $\text{CeO}_2$  and tetragonal  $\text{ZrO}_2$  are shown with blue and red lines, respectively).

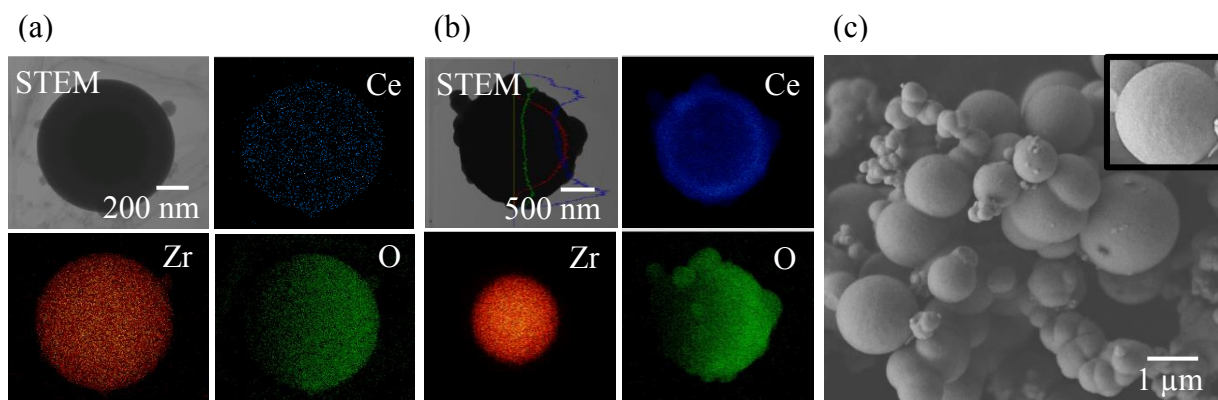


**Figure 3-12.** STEM and EDX mapping images of  $\text{ZrO}_2@\text{CeO}_2$  (a) with thin-shell structure, (b) with  $\text{ZrO}_2@\text{CeO}_2$  with thick-shell structure, and (c) SEM image of  $\text{ZrO}_2@\text{CeO}_2\text{-MeOH}$  composite nanoassemblies.

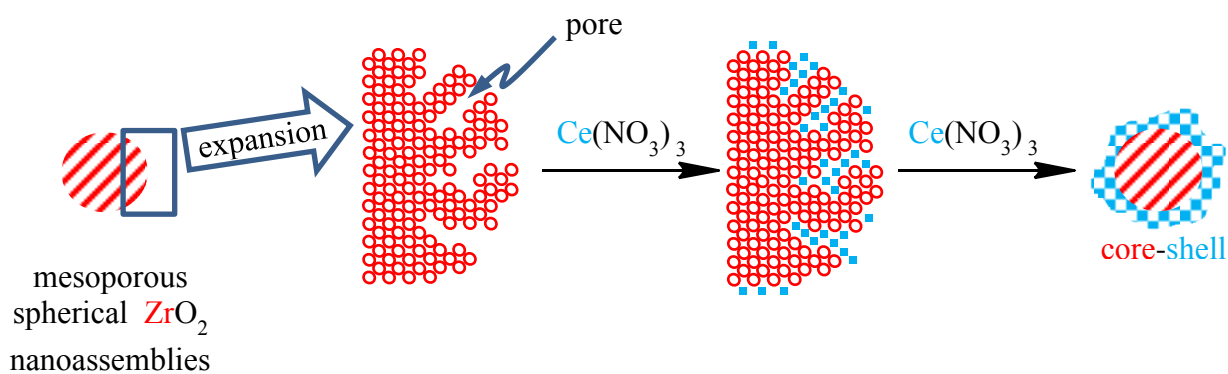


**Figure 3-13.** Schematic illustration of a possible formation mechanism for the  $\text{ZrO}_2@ \text{CeO}_2$  core-shell structure (■ and ○ represent  $\text{CeO}_2$  and  $\text{ZrO}_2$  primary nanoparticles respectively).

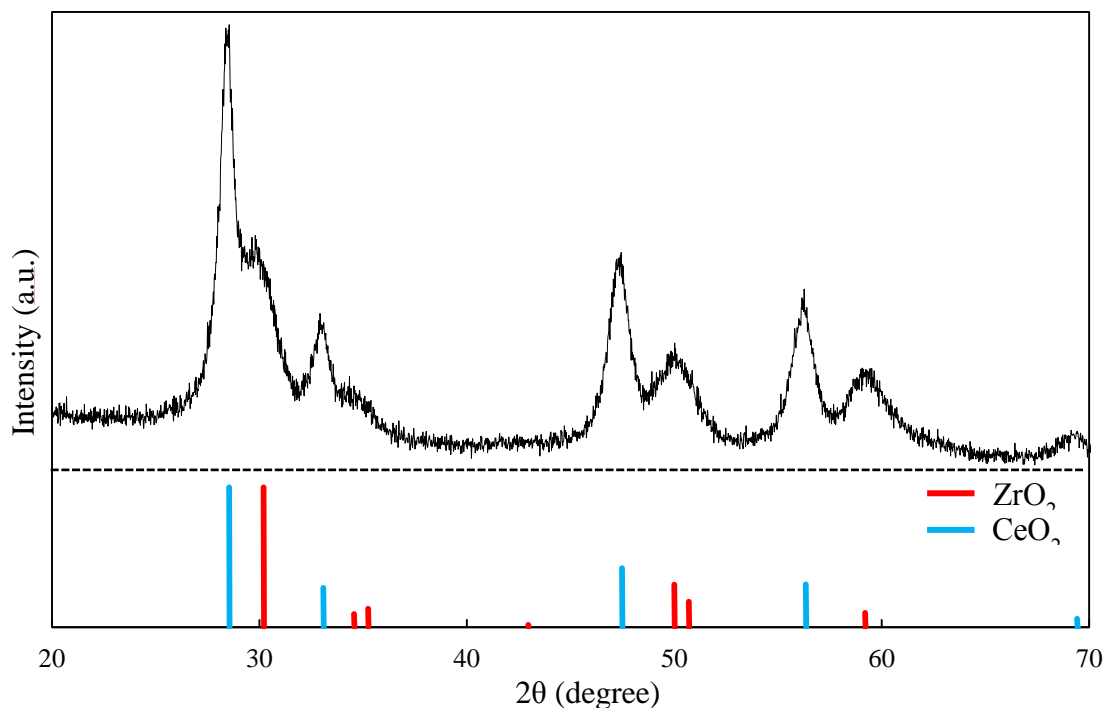


**Figure 3-14.** XRD patterns of  $\text{ZrO}_2@ \text{CeO}_2$ -*i*PrOH core-shell nanoassemblies (peak positions of cubic  $\text{CeO}_2$  and tetragonal  $\text{ZrO}_2$  are shown with blue and red lines, respectively).

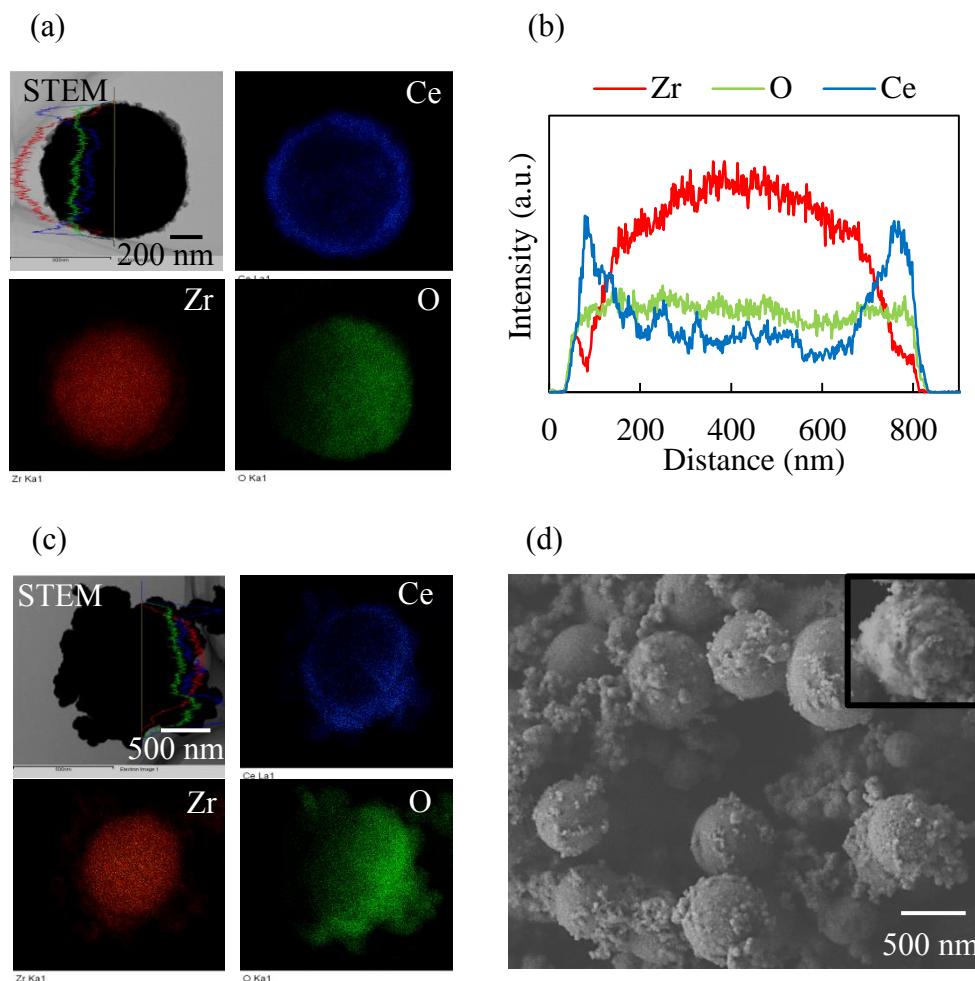


**Figure 3-15.** (a) STEM and EDX mapping images of perfect core-shell structure, (b) line scans of perfect core-shell structure, (c) STEM and EDX mapping images of rugged core-shell structure, and (d) SEM image of  $\text{ZrO}_2@ \text{CeO}_2\text{-}i\text{PrOH}$  core-shell nanoassemblies.

products obtained (referred as  $\text{ZrO}_2@ \text{CeO}_2\text{-}i\text{PrOH}$ ) showed similar XRD patterns (Figure 3-14) to  $\text{ZrO}_2@ \text{CeO}_2\text{-MeOH}$ . However, the results changed drastically to yield mainly  $\text{ZrO}_2@ \text{CeO}_2$  core-shell nanoassemblies with thick-shell where the Ce atoms situated on the edge of the nanoassemblies and Zr at their cores. EDX line scan analysis clearly evidence that the atom density of Ce is higher at the edge than in the core, while those of Zr atoms are higher in the core (Figures 3-15a and b). The ratio of thin-shelled core-shell to thick-shelled

core-shell nanoassemblies is roughly estimated to be 1:10. Not all of the particles exhibited a perfect core-shell structure (Figure 3-15a), but some with rugged structures were also observed (Figure 3-15c); the ratio of the nanoassemblies with perfect core-shell structure to those with rugged structures was approximately 1:25. Similarly,  $\text{TiO}_2@ \text{CeO}_2$  core-shell nanoassemblies were also easily synthesized (Figure 3-16).

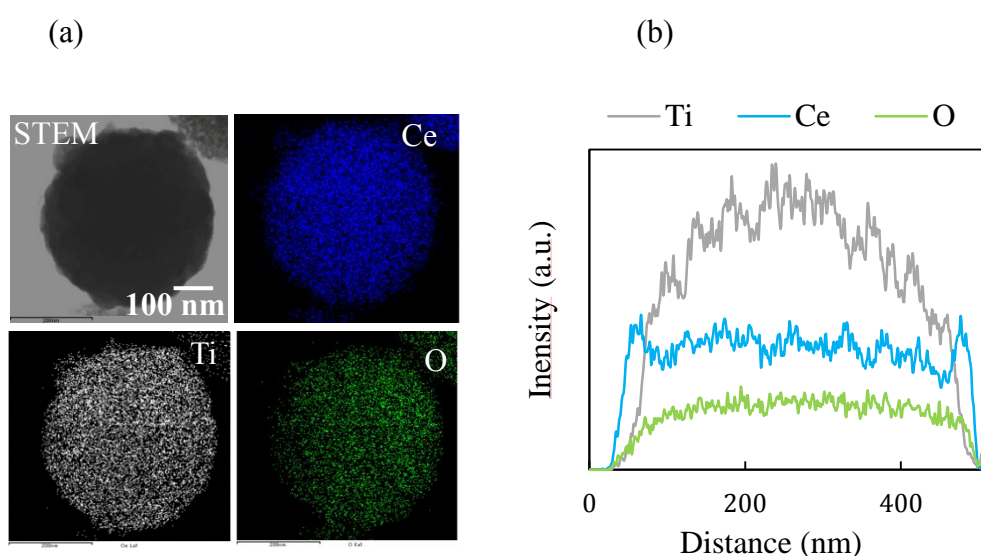


**Figure 3-16.** (a) STEM and EDX mapping images and (b) line scans of  $\text{TiO}_2@ \text{CeO}_2$  core-shell nanoassemblies.

### 3-3 conclusions

An ultimately simple treatment of precursor solutions consisting of  $\text{Ce}^{3+}$ ,  $\text{Zr}^{4+}$ , microporous spherical  $\text{ZrO}_2$  nanoassemblies, and/or formic acid in methanol under supercritical conditions enabled us to synthesize  $\text{CeO}_2\text{-ZrO}_2$  composite nanoassemblies with mesoporous and spherical morphologies into homogeneously mixed, domain, and core-shell structures by changing the reaction conditions such as heating rate, acid, and solvent. Mesoporous spherical  $\text{Ce}_x\text{Zr}_{1-x}\text{O}_2$  composite nanoassemblies with homogeneously mixed structures were prepared from  $\text{Ce}(\text{NO}_3)_3$  and  $\text{ZrO}(\text{NO}_3)_2$  in the presence of formic acid in

methanol by rapid heating (500 °C/min), while mesoporous spherical CeO<sub>2</sub>–ZrO<sub>2</sub> composite nanoassemblies with domain structure were obtained by heating the solution slowly (5.4 °C/min). The atomic compositions of homogeneously mixed Ce<sub>x</sub>Zr<sub>1-x</sub>O<sub>2</sub> were tuned by adjusting the Ce/Zr mixing ration in the precursor solution. Treatment of mesoporous spherical ZrO<sub>2</sub> nanoassemblies with Ce(NO<sub>3</sub>)<sub>3</sub> yielded CeO<sub>2</sub>@ZrO<sub>2</sub> composite nanoassemblies with core-shell structures, where the choice of the solvent played a key role in controlling the thickness of the outer shell. Methanol gave a very thin outer shell of cubic CeO<sub>2</sub>, while a thick shell formed when 2-propanol was used. Thus, the atomic compositions, nano-structures, and morphologies of mesoporous spherical CeO<sub>2</sub>–ZrO<sub>2</sub> nanoassemblies were successfully controlled by a simple solvothermal synthetic method .

### **3-4 Experimental section**

#### **3-4-1 General information**

Methanol, 2-propanol (isopropyl alcohol), formic acid, cerium (III) nitrate hexahydrate, titanium tetraisopropoxide, and zirconium (IV) oxynitrate dihydrate were purchased from Wako Pure Chemical Industries Co. Ltd. These were used as received without further purification.

#### **3-4-2 Synthesis of mesoporous spherical composite nanoassemblies**

CeO<sub>2</sub> MARIMO nanoassemblies and ZrO<sub>2</sub> MARIMO nanoassemblies were prepared according to the method previously reported.<sup>[34,35]</sup> Homogeneously mixed mesoporous spherical Ce<sub>x</sub>Zr<sub>1-x</sub>O<sub>2</sub> (Ce/ZrO<sub>2</sub>) composite nanoassemblies were synthesized by using mixtures of Ce(NO<sub>3</sub>)<sub>3</sub>·6H<sub>2</sub>O (0.25-0.50 mmol), ZrO(NO<sub>3</sub>)<sub>2</sub>·2H<sub>2</sub>O (0.25-0.75 mmol), and formic acid (2.5 mmol) in methanol (5 mL) as precursors. CeO<sub>2</sub>-ZrO<sub>2</sub>-SH was prepared by using equimolar amounts of Ce(NO<sub>3</sub>)<sub>3</sub>·6H<sub>2</sub>O and ZrO(NO<sub>3</sub>)<sub>2</sub>·2H<sub>2</sub>O (0.25 mmol) and formic acid (2.5 mmol) in methanol (5mL) according to the previously reported slow heating method

(5.4 °C/min) up to 400 °C.<sup>[24]</sup> ZrO<sub>2</sub>@CeO<sub>2</sub> core-shell nanoassemblies were synthesized as follows: 30 mg of mesoporous spherical ZrO<sub>2</sub> nanoassemblies and 0.125 mmol of Ce(NO<sub>3</sub>)<sub>3</sub>·6H<sub>2</sub>O were vigorously mixed and dispersed in either 5 mL methanol or 2-propanol. A 3.5 mL portion of the suspension was transferred to an SUS-316 stainless steel tubular reactor of 10 mL inner volume. The reactor was sealed with a screw cap and placed for 10 min in a molten-salt bath which was heated to and maintained at 300 °C. The reaction was quenched by placing the reactor in an ice water bath. The obtained reaction mixture was centrifuged, washed with methanol, and dried under vacuum to give a powdery product.

### 3-4-3 Characterization

XRD patterns were obtained using a Rigaku SmartLab diffractometer with graphite-monochromatized Cu K $\alpha$  radiation (X-ray wavelength: 0.15418 nm) in steps of 0.02 ° over the 2 $\theta$  range of 20–70 °. TEM images and HRTEM images were measured on a JEOL JEM-2100F microscope. EDX mappings and line scan spectra were obtained from Oxford INCA Energy TEM250. SEM images were taken on a JEOL JSM-7300F microscope. Nitrogen adsorption–desorption isotherms were obtained using a BEL Japan INC Belsorp Mini (II).

## References

1. J. Kašpar, P. Fornasiero, M. Graziani, Use of CeO<sub>2</sub>-based oxides in the three-way catalysis, *Catal. Today* **1999**, *50*, 285–298.
2. Y. Nagai, T. Nonaka, A. Suda, M. Sugiura, Structure analysis of CeO<sub>2</sub>-ZrO<sub>2</sub> mixed oxides as oxygen storage promoters in automotive catalysts, *R&D Rev. Toyota CRDL* **2002**, *37*, 20–27.
3. C. Zhang, A. Michaelides, S. J. Jenkins, Theory of gold on ceria, *Phys. Chem. Chem. Phys.* **2011**, *13*, 22–33.

4. H. P. Zhou , H. S. Wu , J. Shen, A. X. Yin , L. D. Sun, C. H. Yan, Thermally stable Pt/CeO<sub>2</sub> hetero-nanocomposites with high catalytic activity, *J. Am. Chem. Soc.* **2010**, *132*, 4998–4999.
5. M. S. Tsai, Powder synthesis of nano grade cerium oxide via homogenous precipitation and its polishing performance, *Mater. Sci. Eng., B* **2004**, *110*, 132–134.
6. S. Armini, J. De Messemaeker, C. M. Whelan, M. Moinpour K. Maex, Composite polymer core-ceria shell abrasive particles during oxide CMP: A Defectivity Study, *J. Electrochem. Soc.* **2008**, *161*, H653–H660.
7. M. P. Yeste, J. C. H. Garrido, D. C. Arias, G. Blanco, J. M. R. Lzquierdo, J. M. Pintado, S. Bernal, J. A. P. Omil, J. J. Calvino, Rational design of nanostructured, noble metal free ceria-zirconia catalysts with outstanding low temperature oxygen storage capacity, *J. Mater. Chem. A* **2013**, *1*, 4836–4844.
8. H. Abe, Current states and Future of the car exhaust catalyst, *Science and Technology Trends, Quarterly Review* **2011**, *39*, 21–31.
9. R. O. Fuentes, L. M. Acuna, M. G. Zimicz, D. G. Lamas, J. G. Sacanell, A. G. Leyva, R. T. Baker, Formation and structural properties of Ce-Zr mixed oxide nanotubes, *Chem. Mater.* **2008**, *20*, 7356–7363.
10. Y. Chen, J. Lu, Facile fabrication of porous hollow CeO<sub>2</sub> microspheres using polystyrene spheres as templates, *J. Porous Mater.* **2012**, *19*, 289–294.
11. L. Zeng, D. Chen, F. Huang, A. Yang, L. Lei, Y. Wang, Uniform Eu<sup>3+</sup>:CeO<sub>2</sub> hollow microspheres formation mechanism and optical performance, *J. Alloys Compd.* **2012**, *534*, 64–69.
12. Y. Wang, Y. Wang, J. Ren, Y. Mi, F. Zhang, C. Li, X. Liu, Y. Guo, Y. Guo, G. Lu, Synthesis of morphology-controllable mesoporous Co<sub>3</sub>O<sub>4</sub> and CeO<sub>2</sub>, *J. Solid State Chem.* **2010**, *183*, 277–284.
13. C. R. Michel, A. H. M. Preciado, CO sensor based on thick films of 3D hierarchical CeO<sub>2</sub> architectures, *Sens. Actuators, B* **2014**, *197*, 177–184.

14. J. Wei, Z. Yang, H. Yang, T. Sun and Y. Yang, A mild solution strategy for the synthesis of mesoporous CeO<sub>2</sub> nanoflowers derived from Ce(HCOO)<sub>3</sub>, *CrystEngComm* **2011**, *13*, 4950–4955.
15. N. S. Priya, C. Somayaji, S. Kanagaraj, Optimization of ceria-zirconia solid solution based on OSC measurement by cyclic heating process, *Procedia Eng.* **2013**, *64*, 1235–1241.
16. H. Xiao, Z. Ai and L. Zhang, Nonaqueous sol–gel synthesized hierarchical CeO<sub>2</sub> nanocrystal microspheres as novel adsorbents for wastewater treatment, *J. Phys. Chem. C* **2009**, *133*, 16625–16630.
17. W. Cai, Q. Zhong, W. Zhao, Y. Bu, Focus on the modified Ce<sub>x</sub>Zr<sub>1-x</sub>O<sub>2</sub> with the rigid benzene-multi-carboxylate ligands and its catalysis in oxidation of NO, *Appl. Catal., B* **2014**, *158-159*, 258–268.
18. R. C. R. Neto, M. Schmal, Synthesis of CeO<sub>2</sub> and CeZrO<sub>2</sub> mixed oxide nanostructured catalysts for the iso-syntheses reaction, *Appl. Catal., A* **2013**, *450*, 131–142.
19. L. C. Yi, W. J. Jyun, T. S. Wen, W. J. J. Jyun, T. T. Chang, Catalysis of Ce<sub>x</sub>Zr<sub>1-x</sub>O<sub>2</sub> for di-iso-propyl-ether hydration, *J. Rare Earths* **2014**, *32*, 860–866.
20. A. Ahniyaz, T. Watanabe, M. Yoshimura, Tetragonal nanocrystals from the Zr<sub>0.5</sub>Ce<sub>0.5</sub>O<sub>2</sub> solid solution by hydrothermal method, *J. Phys. Chem. B* **2005**, *109*, 6136–6139.
21. C. Tyrsted, J. Becker, P. Hald, M. Bremholm, J. Pedersen, J. Chevallier, Y. Cerenius, S. B. Iversen, B. B. Iversen, In-situ synchrotron radiation study of formation and growth of crystalline Ce<sub>x</sub>Zr<sub>1-x</sub>O<sub>2</sub> nanoparticles synthesized in supercritical water, *Chem. Mater.* **2010**, *22*, 1814–1820.
22. C. Hu, Q. Zhu, Z. Jiang, Nanosized CuO-Zr<sub>x</sub>Ce<sub>1-x</sub>O<sub>y</sub> aerogel catalysts prepared by ethanol supercritical drying for catalytic deep oxidation of benzene, *Powder Technol.* **2009**, *194*, 109–114.

23. M. Yashima, K. Marimoto, N. Ishizawa, M. Yoshimura, Zirconia-Ceria solid solution synthesis and the temperature-time-transformation diagram for the 1:1 composition, *J. Am. Ceram. Soc.* **1993**, *76*, 1745–1750.
24. C. Leitenburg, A. Trovarelli, F. Zamar, S. Maschio, G. Dolcetti, J. Liorca, A novel and simple route to catalysts with a high oxygen storage capacity: the direct room temperature synthesis of CeO<sub>2</sub>-ZrO<sub>2</sub> solid solutions, *J. Chem. Soc., Chem. Commun.* **1995**, 2181–2182.
25. T. Yoshioka, K. Dosaka, T. Sato, A. Okuwaki, S. Tanno, T. Miura, Preparation of spherical ceria-doped tetragonal zirconia by the spray-pyrolysis method, *J. Mater. Sci. Lett.* **1992**, *11*, 51–55.
26. X. Liang, J. Xiao, B. Chen, Y. Li, Catalytically Stable and Active CeO<sub>2</sub> Mesoporous Spheres, *Inorg. Chem.* **2010**, *49*, 8188–8190.
27. C. Sun, H. Li, L. Chen, Nanostructured ceria-based materials: synthesis, properties, and applications, *Energy Environ. Sci.* **2012**, *5*, 8475–8505.
28. P. Wang, K. Kobiro, Synthetic versatility of nanoparticles: A new, rapid, one-pot, single-step synthetic approach to spherical mesoporous (metal) oxide nanoparticles using supercritical alcohols, *Pure Appl. Chem.* **2014**, *86*, 785–800.
29. W. Hertl, Surface chemistry of zirconia polymorphs, *Langmuir* **1989**, *5*, 96–100.
30. A. Adamski, P. Jakubus, Z. Sojka, Structural and textural evolution of zirconia nanocrystals induced by thermal treatment, *Mater. Sci.-Pol.* **2008**, *26* 373–380.
31. P. Duran, M. Gonzalez, C. Moure, J. R. Jurado, C. Pascual, A new tentative phase equilibrium diagram for the ZrO<sub>2</sub>-CeO<sub>2</sub> system in air, *J. Mater. Sci.* **1990**, *25*, 5001–5006.
32. A. Suda, Y. Kae, A. Morikawa, Y. Nagai, H. Sobukawa, Y. Ukyo, H. Shinjo, Atmospheric pressure solvothermal synthesis of ceria-zirconia solid solutions and their large oxygen storage capacity, *J. Mater. Sci.* **2008**, *43*, 2258–2262.
33. C. Slostowski, S. Marre, O. Babot, T. Toupance, C. Aymonier, Near-and supercritical alcohols as solvents and surface modifiers for the continuous synthesis of cerium oxide nanoparticles, *Langmuir* **2012**, *28* 16656–16663.

## Chapter 4.

# Synthesis of MgO ultra-fine nanocrystals by single-step solvothermal method

### 4-1 Introduction

MgO is an insulating material with wide band gap energy (7.5 eV) which would be a key material for deep ultraviolet (UV) light emitting devices.<sup>[1]</sup> Nano-size MgO is usually synthesized by calcination of nano-size solid intermediates such as Mg(OH)<sub>2</sub>,<sup>[2]</sup> MgCO<sub>3</sub>,<sup>[3]</sup> and magnesium containing MOFs.<sup>[4,5]</sup> Synthesis of Mg(OH)<sub>2</sub> solid intermediates by several methods such as precipitation, sol-gel, and electrodeposition were reported.<sup>[6-8]</sup> In addition, the hydrothermal treatment of Mg salts or Mg powder itself in an autoclave reported to afford Mg(OH)<sub>2</sub> nanoassemblies, where the morphologies of the Mg(OH)<sub>2</sub> nanoassemblies controlled by changing the form of magnesium, solvents, and bases.<sup>[2]</sup> Also, morphology control of Mg(OH)<sub>2</sub> nanoassemblies by using some additives such as neutral ligands, polymeric capping agents, and surfactants was also reported.<sup>[2,9,10]</sup> On the other hand, nano-size MgCO<sub>3</sub> as a solid intermediate product of MgO nanomaterials was prepared by precipitation, hydrothermal, two-step solvothermal methods, etc.<sup>[3,11-14]</sup> Morphologies of the basic MgCO<sub>3</sub> solid precursors were controlled by changing pH, solvent, and reaction temperature in their syntheses.<sup>[3,11,12]</sup> Few examples on calcination of Mg containing MOFs were also reported to afford MgO nanomaterials.<sup>[4,5]</sup> Thus, the synthesis of MgO nanomaterials by high temperature calcination of solid intermediates is one of the simplest methods, while the calcination usually results in increase of their primary nanocrystal size,<sup>[15]</sup> which eventually becomes a barrier to realize deep UV light emitting materials. Therefore,

the development of synthetic methods to obtain MgO ultra-fine nanocrystals without calcination is of quite importance.

Some of single-step solvothermal synthesis of ultra-fine nanoparticles of various metal oxides without calcination are reported in the literatures, which indicate the possibility of solvothermal method to yield MgO ultra-fine nanoparticles.<sup>[16-19]</sup> However, attempted synthesis of MgO nanomaterials by solvothermal methods resulted in Mg(OH)<sub>2</sub> instead of MgO.<sup>[2,9,20]</sup> Dehydration of the obtained Mg(OH)<sub>2</sub> nanomaterials did not occur in typical solvothermal methods due to their chemical and physical stability.<sup>[9]</sup> Therefore, it is required to use much drastic conditions to afford MgO nanocrystals through solvothermal synthesis.

As mentioned in former chapters, Wang et al. developed high-temperature and high-pressure alcohol based single-step one-pot simple solvothermal method to obtain several kinds of MARIMO nanoassemblies, such as SiO<sub>2</sub>, TiO<sub>2</sub>, ZnO, ZrO<sub>2</sub>, and CeO<sub>2</sub>.<sup>[16]</sup> The morphologies of the MARIMO nanoassemblies were easily controlled by changing the reaction parameters such as metal salts or alkoxides, heating rate, and reaction temperature.<sup>[16,21]</sup> On the other hand, coordination atmosphere of the metal cation would be an important factor to control the hydrolysis of metal salts or alkoxides in the solvothermal reactions. Then, I supposed our solvothermal method would afford MgO ultra-fine nanocrystals through controlling of coordination atmosphere of the Mg<sup>2+</sup> cation and reaction temperature.

## 4-2 Results and discussion

First, direct synthesis of MgO ultra-fine nanocrystals was attempted through the above mentioned alcohol based solvothermal method. Upon treatment of a solution of Mg(NO<sub>3</sub>)<sub>2</sub> in methanol with no additive at 300 °C, a powdery product was obtained. TEM images (Figure 4-1a) and XRD patterns (Figure 4-2a) showed that the obtained flower shape nanoassemblies

plausibly consisting of  $\text{Mg}_2\text{O}(\text{OH})_2$  (JCPDS 01-070-9187). In order to accelerate the hydrolysis of  $\text{Mg}(\text{NO}_3)_2$  in the solvothermal reactions, five times excess amount of formic acid was added to the precursor solution and reaction was performed at 300 °C. However, TEM image (Figure 4-1b) and XRD patterns (Figure 4-2b) of obtained nanoassemblies revealed that the shape of nanoassemblies was quite similar to that of  $\text{Mg}_2\text{O}(\text{OH})_2$  obtained without formic acid.

On the other hand, the hydrolysis of Mg salts can be controlled through tuning of coordination atmosphere by changing the anion of the Mg salt. The synthesis of nanomaterials *via* decomposition of metal acetylacetonate (acac) is a well-known approach to obtain nano-size metal oxides, such as  $\text{TiO}_2$ ,  $\text{V}_2\text{O}_3$ ,  $\text{Fe}_2\text{O}_3$ ,  $\text{ZnO}$ ,  $\text{In}_2\text{O}_3$ ,  $\text{SnO}_2$ ,  $\text{Ga}_2\text{O}_3$ ,  $\text{Nb}_2\text{O}_5$ ,  $\text{Ta}_2\text{O}_5$ , and  $\text{HfO}_2$ .<sup>[22]</sup> Then, solvothermal treatment of  $\text{Mg}(\text{acac})_2$  in high-temperature and high-pressure methanol was investigated in expectation of one-step synthesis of the desired MgO nanocrystals. Treatment of  $\text{Mg}(\text{acac})_2$  solution in methanol at 300 °C afforded beautiful hexagonal nanosheets (Figure 4-1c). However, they were not desired MgO but  $\text{Mg}(\text{OH})_2$  (brucite: JCPDS 01-071-5972) judging from XRD analysis (Figure 4-2c).

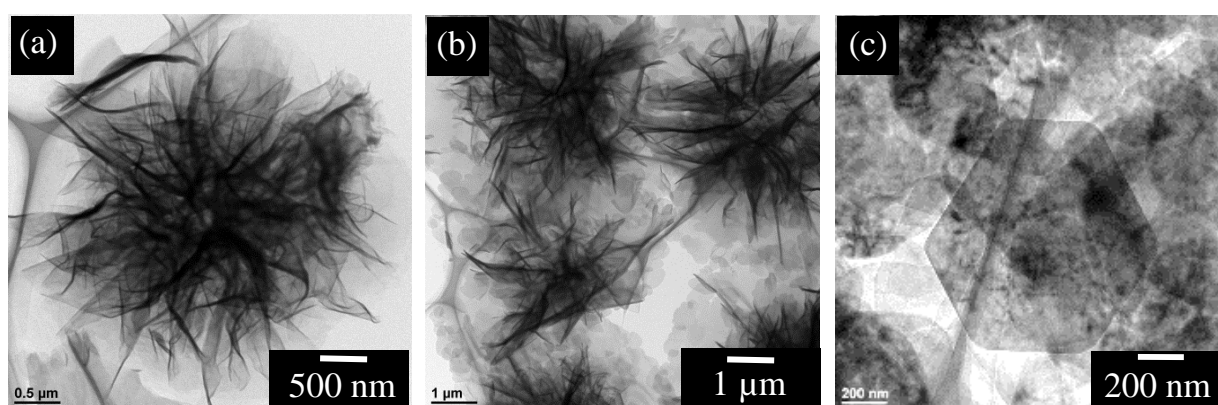


**Figure 4-1.** TEM images of nanomaterials synthesized by solvothermal treatments of (a)  $\text{Mg}(\text{NO}_3)_2$  in methanol at 300 °C; (b) a mixture of  $\text{Mg}(\text{NO}_3)_2$  and  $\text{HCOOH}$  in methanol at 300 °C; and (c)  $\text{Mg}(\text{acac})_2$  in methanol at 300 °C.

Mg(OH)<sub>2</sub> is usually calcinated at 400–600 °C to yield MgO because dehydration of Mg(OH)<sub>2</sub> requires high temperature such as over 290 °C.<sup>[23]</sup> Then, the solution of Mg(NO<sub>3</sub>)<sub>2</sub> in methanol was treated at higher temperature of 400 °C in expectation of *in situ* MgO nanocrystals formation under the solvothermal conditions. However, the resulting flower shape nanoassemblies (Figure 4-3a) plausibly consisting of Mg<sub>2</sub>O(OH)<sub>2</sub> judging from their XRD patterns (Figure 4-4a) even though the reaction was performed at higher temperature of 400 °C.

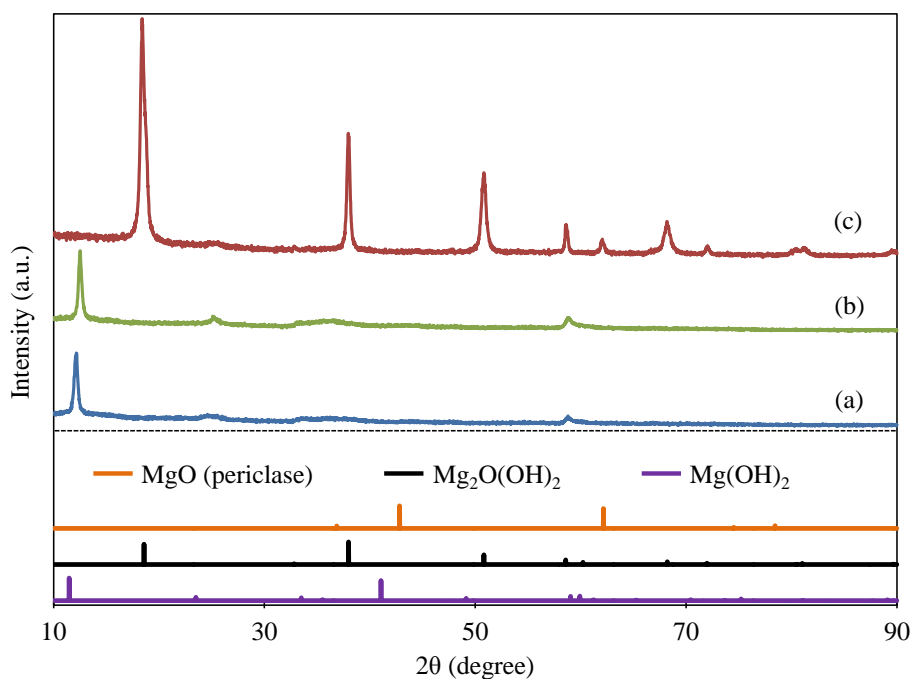


**Figure 4-2.** XRD patterns of nanomaterials synthesized by solvothermal treatments of (a) Mg(NO<sub>3</sub>)<sub>2</sub> in methanol at 300 °C; (b) a mixture of Mg(NO<sub>3</sub>)<sub>2</sub> and HCOOH in methanol at 300 °C; and (c) Mg(acac)<sub>2</sub> in methanol at 300 °C.

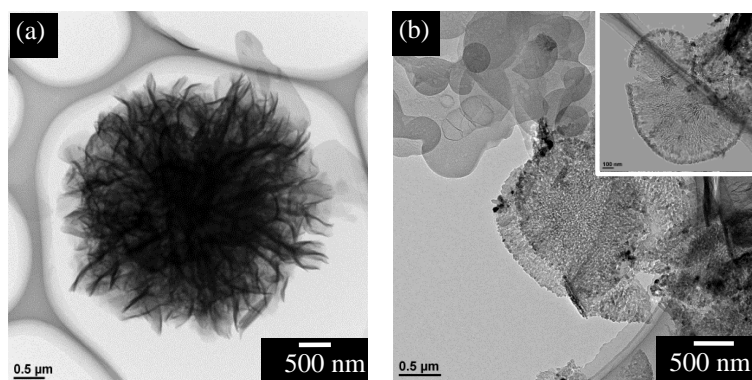


**Figure 4-3.** TEM images of nanomaterials synthesized by solvothermal treatments of (a)  $\text{Mg}(\text{NO}_3)_2$  in methanol at 400 °C and (b) a mixture of  $\text{Mg}(\text{NO}_3)_2$ , bis(2-aminoethyl)amine, and  $\text{Mg}(\text{NO}_3)_2$  in methanol at 400 °C.

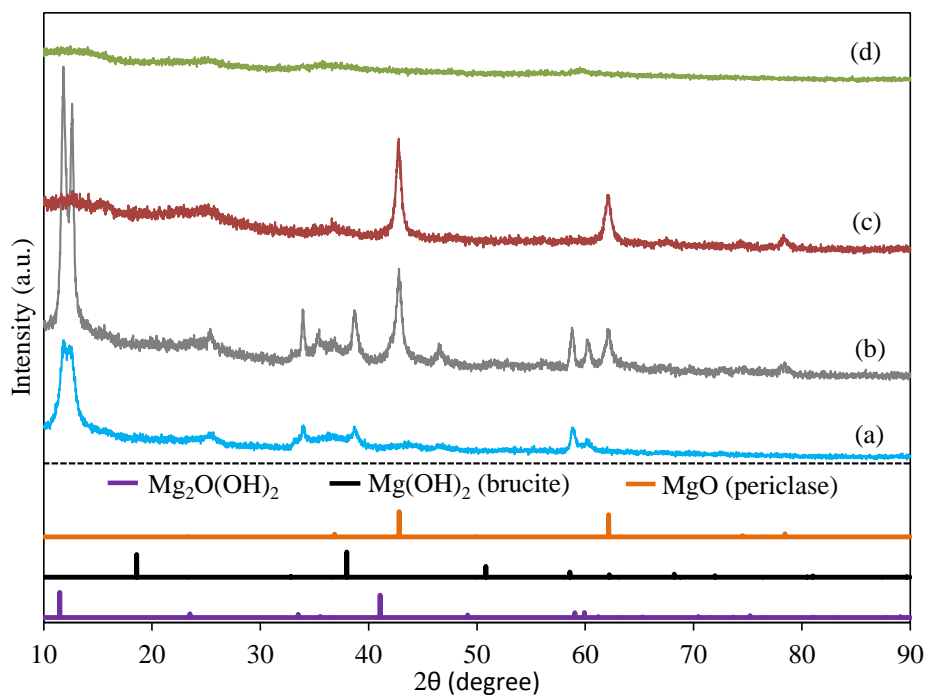


**Figure 4-4.** XRD patterns of nanomaterials synthesized by solvothermal treatments of (a)  $\text{Mg}(\text{NO}_3)_2$  in methanol at 400 °C; (b)  $\text{Mg}(\text{NO}_3)_2$ , bis(2-aminoethyl)amine, and  $\text{Mg}(\text{NO}_3)_2$  in methanol at 400 °C; (c)  $\text{Mg}(\text{NO}_3)_2$ , bis(2-aminoethyl)amine, and  $\text{Mg}(\text{NO}_3)_2$  in acetonitrile at 400 °C; and (d)  $\text{Mg}(\text{NO}_3)_2$  and triethylene glycol in acetonitrile at 400 °C.

Also, the coordination atmosphere of the  $\text{Mg}^{2+}$  ions can be adjusted by addition of neutral ligands.<sup>[24]</sup> Then, bis(2-aminoethyl)amine was selected as a suitable organic ligand. Solvothermal treatment of a mixture of  $\text{Mg}(\text{NO}_3)_2$  and bis(2-aminoethyl)amine in methanol at 400 °C afforded nanosheets, in which the formation of nanocrystals in some of nanosheets were observed (Figure 4-3b). A mixed profile of MgO (periclase : JCPDS 01-076-5381) and unidentified materials was observed on XRD patterns (Figure 4-4b), indicating that partial dehydration of  $\text{Mg}(\text{OH})_2$  occurred to give nanocrystals of MgO. The size of the crystalline nanoparticles formed at the edges of the nanosheets was larger than that of at the center (Figure 4-3b inset).

When solvothermal reactions in alcohols are performed at elevated temperature, water should be generated by condensation of alcohols, which would cause the incomplete dehydration of  $\text{Mg}(\text{OH})_2$  or  $\text{Mg}_2\text{O}(\text{OH})_2$ . Therefore, solvents which do not yield water at high-temperature conditions should be taken to yield MgO nanomaterials in the solvothermal conditions. In addition, solvent is another important parameter for coordination atmosphere tuning of the  $\text{Mg}^{2+}$  ions. Then, acetonitrile was chosen as an alternative solvent. A precursor solution containing  $\text{Mg}(\text{NO}_3)_2$  and bis(2-aminoethyl)amine in acetonitrile was solvothermally treated under high-temperature and high-pressure conditions at 400 °C for 10 min. The results were more than expected to yield desired MgO ultra-fine nanocrystals with the size of ca. 5 nm (Figures 4-4c and 4-5a). Moreover, the XRD patterns did not show any peak corresponding to that of either  $\text{Mg}(\text{OH})_2$  or  $\text{Mg}_2\text{O}(\text{OH})_2$ , clearly indicating that almost complete dehydration of  $\text{Mg}(\text{OH})_2$  or  $\text{Mg}_2\text{O}(\text{OH})_2$  affording MgO nanocrystals occurred. The similar treatment of  $\text{Mg}(\text{NO}_3)_2$  and triethylene glycol in acetonitrile surprisingly afforded nanoassemblies with hollow spherical morphology (Figures 4-5b). The XRD patterns (Figure 4-4c) did not show any clear peaks, while the EDX analysis on STEM showed that

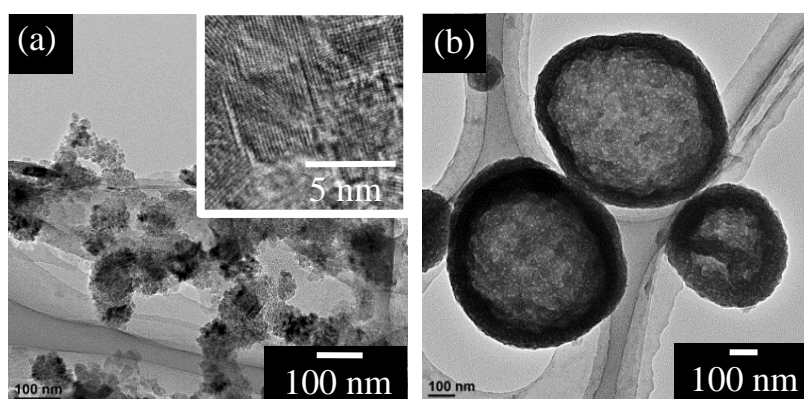


**Figure 4-5.** TEM images of nanomaterials obtained by solvothermal treatments of (a)  $\text{Mg}(\text{NO}_3)_2$ , bis(2-aminoethyl)amine, and  $\text{Mg}(\text{NO}_3)_2$  in acetonitrile at 400 °C and (b)  $\text{Mg}(\text{NO}_3)_2$  and triethylene glycol in acetonitrile at 400 °C.

the hollow spherical nanoassemblies contain Mg and O atoms. Thus, MgO ultra-fine nanocrystals were successfully synthesized through the tuning of coordination atmosphere of  $\text{Mg}^{2+}$  cation by changing the anion, ligand, reaction temperature, and solvent in the our simple solvothermal method.

### 4-3 Conclusions

MgO ultra-fine nanocrystals were obtained by the treatment of a precursor solution containing  $\text{Mg}(\text{NO}_3)_2$  and bis(2-aminoethyl)amine in acetonitrile at 400 °C. Similar treatment of a precursor solution containing  $\text{Mg}(\text{NO}_3)_2$  and triethylene glycol in acetonitrile resulted in hollow spherical amorphous nanoassemblies consisting of Mg and O atoms. On the other hand,  $\text{Mg}_2\text{O}(\text{OH})_2$  flower shape nanoassemblies were obtained by the solvothermal treatment of a solution of  $\text{Mg}(\text{NO}_3)_2$  in methanol at 300 °C, while beautiful hexagonal brucite  $\text{Mg}(\text{OH})_2$  nanosheets were afforded by the similar treatment of  $\text{Mg}(\text{acac})_2$  in methanol. Individual nanosheets plausibly consisting of  $\text{Mg}_2\text{O}(\text{OH})_2$  were yielded by the treatment of a precursor solution containing  $\text{Mg}(\text{NO}_3)_2$  and bis(2-aminoethyl)amine in methanol at 300 °C, and the

nanosheets with MgO nanocrystals were afforded under high-temperature reaction conditions at 400 °C. Thus, MgO ultra-fine nanocrystals were successfully synthesized by ultimately simple solvothermal method, which can be a key material for deep UV light emission.

## **4-4 Experimental section**

### **4-4-1 General information**

Methanol, acetonitrile, bis(2-aminoethyl)amine, magnesium nitrate hexahydrate, and magnesium acetylacetonate dihydrate were purchased from Wako pure Chemical Industries Co. Ltd. These were used as received without further purification.

### **4-4-2 Synthesis of MgO nanocrystals and nanoassemblies**

Precursor solutions containing 0.35 mmol of  $\text{Mg}(\text{NO}_3)_2 \cdot 6\text{H}_2\text{O}$  or  $\text{Mg}(\text{acac})_2 \cdot \text{H}_2\text{O}$  dissolved in 3.5 mL of methanol was transferred to an SUS-316 stainless steel tubular reactor of 10 mL inner volume. The reactor was sealed with a screw cap and slowly heated with a rate of 5.4 °C/min up to 300 °C or 400 °C and the final temperature was maintained for 10 minutes. The reaction was quenched by placing the reactor in an ice water bath. The obtained reaction mixture was centrifuged and the supernatant was decanted off. The crude particles were washed with methanol several times and dried under vacuum to give a powdery product. The precursor solutions containing 0.35 mmol of  $\text{Mg}(\text{NO}_3)_2 \cdot 6\text{H}_2\text{O}$  and 1.75 mmol of HCOOH in 3.5 mL of methanol; 0.35 mmol of  $\text{Mg}(\text{NO}_3)_2 \cdot 6\text{H}_2\text{O}$  and 1.75 mmol of bis(2-aminoethyl)amine in 3.5 mL of methanol; 0.35 mmol of  $\text{Mg}(\text{NO}_3)_2 \cdot 6\text{H}_2\text{O}$  and 1.75 mmol of bis(2-aminoethyl)amine in 3.5 mL of acetonitrile; and 0.35 mmol of  $\text{Mg}(\text{NO}_3)_2 \cdot 6\text{H}_2\text{O}$  and 11 mmol of triethylene glycol in 3.5 mL of acetonitrile were also treated by similar methods.

### 4-4-3 Characterization

XRD patterns were obtained using a Rigaku SmartLab diffractometer with graphite-monochromatized Cu  $K\alpha$  radiation (X-ray wavelength: 0.15418 nm) in steps of 0.02 ° over the 2 $\theta$  range of 20–90 °. TEM images and HRTEM images were measured on a JEOL JEM-2100F microscope. EDX spectra were obtained from Oxford INCA Energy TEM250.

### References

1. Y. -N. Xu, W. Y. Ching, Self-consistent band structures, charge distributions, and optical-absorption spectra in MgO,  $\gamma$ -Al<sub>2</sub>O<sub>3</sub>, and MgAl<sub>2</sub>O<sub>4</sub>, *Phys. Rev. B: Condens. Matter Mater. Phys.*, **1991**, *43*, 4461–4472.
2. Y. Ding, G. Zhang, H. Wu, B. Hai, L. Wang, Y. Qian, Nanoscale magnesium hydroxide and magnesium oxide powders: control over size, shape, and structure via hydrothermal synthesis, *Chem. Mater.* **2001**, *13*, 435–440.
3. N. Sutradhar, A. Sinhamahapatra, S. K. Pahari, P. Pal, H. C. Bajaj, I. Mukhopadhyay, A. B. Panda, Controlled synthesis of different morphologies of MgO and their use as solid base catalysts, *J. Phys. Chem. C* **2011**, *115*, 12308–12316.
4. B. Huang, H. Kobayashi, H. Kitagawa, Facile synthesis of small MgO nanoparticle/metal organic framework hybrid material, *Chem. Lett.* **2014**, *43*, 1459–1460.
5. T. K. Kim, K. J. Lee, J. Y. Cheon, J. H. Lee, S. H. Joo, H. R. Moon, Nanoporous metal oxides with tunable and nanocrystalline frameworks via conversion of metal–organic frameworks, *J. Am. Chem. Soc.* **2013**, *135*, 8940–8946.
6. A. Chandran, J. Prakash, K. K. Naik, A. K. Srivastava, R. Dabrowski, M. Czerwinski, A. M. Biradar, Preparation and characterization of MgO nanoparticles/ferroelectric liquid crystal composites for faster display devices with improved contrast, *J. Mater. Chem. C* **2014**, *2*, 1844–1853.

7. H. Minami, K. Kinoshita, T. Tsuji, H. Yanagimoto, Preparation of highly crystalline magnesium oxide and polystyrene/magnesium hydroxide composite particles by sol-gel processes in an ionic liquid, *J. Phys. Chem. C* **2012**, *116*, 14568–14574.
8. Y. Lv, Z. Zhang, Y. Lai, Y. Liu, Electrodeposition of porous Mg(OH)<sub>2</sub> thin films composed of single-crystal nanosheets, *J. Electrochem. Soc.* **2012**, *159*, D187–D189.
9. A. Subramania, G. V. Kumar, A. R. S. Priya, T. Vasudevan, Polyol-mediated thermolysis process for the synthesis of MgO nanoparticles and nanowires, *Nanotechnology* **2007**, *18*, 225601.
10. F. Liu, Q. Shen, Y. Su, S. Han, G. Xu, D. Wang, Transcriptive synthesis of Mg(OH)<sub>2</sub> hollow nanospheres and the non-equilibrium shell fusion assisted by catanionic vesicles, *J. Phys. Chem. B* **2009**, *113*, 11362–11366.
11. Q. Lia, Y. Dinga, G. Yua, C. Lia, F. Lib, Y. Qiana, Fabrication of light-emitting porous hydromagnesite with rosette-like architecture, *Solid State Commun.* **2003**, *125*, 117–120.
12. C. Yan, D. Xue, Novel self-assembled MgO nanosheet and its precursors, *J. Phys. Chem. B* **2005**, *109*, 12358–12361.
13. Z. Zhang, Y. Zheng, J. Zhang, Q. Zhang, J. Chen, Z. Liu, X. Liang, Synthesis and shape evolution of monodisperse basic magnesium carbonate microspheres, *Cryst. Growth Des.* **2007**, *7*, 339–342.
14. C. Gao, W. Zhang, H. Li, L. Lang, Z. Xu, Controllable fabrication of mesoporous MgO with various morphologies and Their absorption performance for toxic pollutants in water, *Cryst. Growth Des.* **2008**, *8*, 3785–3790.
15. Y. Li, J. Shi, Hollow-structured mesoporous materials: chemical synthesis, functionalization and applications, *Adv. Mater.* **2014**, *26*, 3176–3205.
16. P. Wang, K. Kobiro, Synthetic versatility of nanoparticles: a new, rapid, one-pot, single-step synthetic approach to spherical mesoporous (metal) oxide nanoparticles using supercritical alcohols, *Pure Appl. Chem.* **2014**, *86*, 785–800.
17. J. Lu, X. Jiao, D. Chen, W. Li, Solvothermal Synthesis and Characterization of Fe<sub>3</sub>O<sub>4</sub> and  $\gamma$ -Fe<sub>2</sub>O<sub>3</sub> Nanoplates, *J. Phys. Chem. C* **2009**, *113*, 4012–4017.

18. J. Ma, J. Zhang, S. Wang, T. Wang, J. Lian, X. Duan, W. Zheng, Topochemical preparation of  $\text{WO}_3$  nanoplates through precursor  $\text{H}_2\text{WO}_4$  and their gas-sensing performances, *J. Phys. Chem. C* **2011**, *115*, 18157–18163.
19. C. Aymonier, A. L. Serani, H. Reveron, Y. Garrabos, F. Cansell, Review of supercritical fluids in inorganic materials science, *J. Supercrit Fluids* **2006**, *38*, 242–251.
20. F. A.-Hazmi, A. Umar, G. N. Dar, A. A. A.-Ghamdi, S. A. A.-Sayari, A. A.-Hajry, S. H. Kim, Reem M. A.-Tuwirqi, F. Alnowaiserb, F. E.-Tantawy, Microwave assisted rapid growth of  $\text{Mg}(\text{OH})_2$  nanosheet networks for ethanol chemical sensor application, *J. Alloys Compd.*, **2012**, *519*, 4–8.
21. P. Wang, K. Ueno, H. Takigawa, K. Kobiuro, Versatility of one-pot, single-step synthetic approach for spherical porous(metal) oxide nanoparticles using supercritical alcohols, *J. Supercrit. Fluids* **2013**, *78*, 124–131.
22. N. Pinna, G. Garnweitner, M. Antonietti, M. Niederberger, A general nonaqueous route to binary metal oxide nanocrystals involving a C-C bond cleavage, *J. Am. Chem. Soc.* **2005**, *127*, 5608–5612.
23. J. M. Hanlon, L. B. Diaz, G. Balducci, B. A. Stobbs, M. Bielewski, P. Chung, I. MacLarend, D. H. Gregory, Rapid surfactant-free synthesis of  $\text{Mg}(\text{OH})_2$  nanoplates and pseudomorphic dehydration to  $\text{MgO}$ , *CrystEngComm* **2015**, *17*, 5672–5679.
24. L. Fabbrizzi, A. Poggi, Anion recognition by coordinative interactions: metal–amine complexes as receptors, *Chem. Soc. Rev.* **2013**, *42*, 1681–1699.

## Chapter 5.

### Conclusions

Versatility of solvothermal synthetic method was demonstrated *via* ultimately simple single-step synthesis of  $\text{Al}_2\text{O}_3\text{-TiO}_2$  and  $\text{ZnO-TiO}_2$  composite spherical nanoassemblies with hollow morphology.  $\text{Al}_2\text{O}_3\text{-TiO}_2$  hollow composite nanoassemblies consisting of anatase  $\text{TiO}_2$  primary nanoparticles mixed with amorphous  $\text{Al}_2\text{O}_3$  fine primary nanoparticles were obtained by one-pot simple solvothermal method with high-temperature and high-pressure methanol. The atomic compositions of the  $\text{Al}_2\text{O}_3\text{-TiO}_2$  hollow composite nanoassemblies were controlled by changing the Al/Ti alkoxides mixing ratio in the precursor solution.  $\text{Al}_2\text{O}_3\text{-TiO}_2$  hollow composite nanoassemblies with high Al content (Al = 50–75%) exhibited large surface area exceeding  $600 \text{ m}^2 \text{ g}^{-1}$ .  $\text{Al}_2\text{O}_3\text{-TiO}_2$  hollow composite nanoassemblies with high Al content (Al = 50%) did not show a phase transition from anatase to rutile even after high-temperature calcination at  $1000 \text{ }^\circ\text{C}$  for 1h.  $\text{ZnO-TiO}_2$  hollow composite nanoassemblies consisting of anatase  $\text{TiO}_2$  primary nanoparticles mixed with amorphous  $\text{ZnO}$  fine primary nanoparticles were obtained by one-pot simple solvothermal method with high-temperature and high-pressure methanol. The atomic compositions of the  $\text{ZnO-TiO}_2$  composite nanoassemblies were controlled by changing the Zn/Ti alkoxide/salt mixing ratio in the precursor solution. The band-gap energies of  $\text{ZnO-TiO}_2$  nanoassemblies were easily tuned by changing their  $\text{ZnO}$  content.

$\text{CeO}_2\text{-ZrO}_2$  which is one of the most promising mixed metal oxide composite catalysts for exhaust gas treatment was synthesized by simple solvothermal method. The nano-structures of spherical composite nanoassemblies were easily controlled to yield  $\text{Ce}_x\text{Zr}_{1-x}\text{O}_2$  homogeneous mixtures and  $\text{CeO}_2\text{-ZrO}_2$  with domain structure by simply changing heating rate. The atomic compositions of homogeneous  $\text{Ce}_x\text{Zr}_{1-x}\text{O}_2$  composite

nanoassemblies were easily tuned by adjusting the Ce/Zr salts mixing ratio in the precursor solutions. CeO<sub>2</sub>@ZrO<sub>2</sub> core-shell type spherical nanoassemblies were synthesized by step-wise approach.

Solvothermal treatment of a precursor solution containing Mg(NO<sub>3</sub>)<sub>2</sub> and bis(2-aminoethyl)amine in acetonitrile at 400 °C is a superior synthetic approach to MgO ultra-fine nanocrystals which can be a key material for deep UV light emitting devices. Amorphous hollow spherical nanoassemblies consisting of Mg and O atoms were obtained by the similar treatment of a precursor solution containing Mg(NO<sub>3</sub>)<sub>2</sub> and triethylene glycol in acetonitrile.

Thus, two frontiers of solvothermal methods in the field of metal oxide nanomaterial synthesis i.e., (i) ultimate simple solvothermal synthesis of mixed metal oxide composite nanoassemblies and (ii) single-step solvothermal synthesis of MgO ultra-fine nanoparticles were conquered through the rationally designed solvothermal methods. Morphologies and nano-structures of the nanomaterials were quite easily controlled by changing the metal salts and alkoxides, organic ligands as additives, solvents, heating rate, and reaction temperature demonstrating the versatility of my solvothermal method in the field of metal oxide nanomaterial synthesis. Given the importance of our solvothermal method as an ultimately simple synthetic approach to metal oxide nanomaterials as well as a highly suitable synthetic method for scaling up towards industrial level, I believe that my research will significantly contribute to the development of science and engineering.

## List of works

### Publications

1. **E. K. C. Pradeep**, T. Habu, H. Tooriyama, M. Ohtani, K. Kobiro, Ultra-simple synthetic approach to the fabrication of CeO<sub>2</sub>-ZrO<sub>2</sub> mixed nanoparticles into homogeneous, domain, and core-shell structures in mesoporous spherical morphologies using supercritical alcohols, *J. Supercrit. Fluids* **2015**, 97, 217–223.
2. **E. K. C. Pradeep**, M. Ohtani and, K. Kobiro, A simple synthetic approach to Al<sub>2</sub>O<sub>3</sub>-TiO<sub>2</sub> and ZnO-TiO<sub>2</sub> mesoporous hollow composite assemblies consisting of homogeneously mixed primary particles at the nano level, *Eur. J. Inorg. Chem.* **2015**, 5621–5627.

### Presentations

1. **E. K. C. Pradeep**, T. Habu, H. Tooriyama, M. Ohtani, K. Kobiro, Composition and morphology control of CeO<sub>2</sub>-ZrO<sub>2</sub> composites, 高知化学会第27回研究会講演会, 高知市, 8月, **2014**.
2. H. Tooriyama, **E. K. C. Pradeep**, P. Wang, K. Kobiro, Smart decoration of spherical mesoporous TiO<sub>2</sub> nanoparticles with core-shell alloy nanoparticles in supercritical methanol, *4th International Solvothermal and Hydrothermal Association Conference*, Boudreaux, France, October **2014**.
3. **E. K. C. Pradeep**, H. Tooriyama, P. Wang, K. Kobiro, Ultimately simple and smart synthesis of new mesoporous nanoparticles in supercritical methanol, *4th International Solvothermal and Hydrothermal Association Conference*, Boudreaux, France, October **2014**.
4. **E. K. C. Pradeep**, T. Habu, H. Tooriyama, M. Ohtani, K. Kobiro, Fabrication of CeO<sub>2</sub>-ZrO<sub>2</sub> mixed spherical mesoporous nanoparticles into homogeneous, domain, and core-shell structures, *4th International Solvothermal and Hydrothermal Association Conference*, Boudreaux, France, October **2014**.
5. **E. K. C. Pradeep**, M. Ohtani, K. Kobiro, One-pot Single-step Synthetic Approach to Morphology Controlled Binary Metal Oxide Nanospheres, *Kochi University-Kochi University of Technology Joint Seminar of Chemistry*, Kochi, Japan, June **2015**.
6. **E. K. C. Pradeep**, M. Ohtani, K. Kobiro, One-pot, single-step, and template free synthesis of mesoporous spherical composite metal oxide nanoparticles in

supercritical alcohols, *2nd Annual International Conference on Nanoscience and Nanotechnology–2015*, Colombo, Sri Lanka, September **2015**.

7. M. Ohtani, **E. K. C. Pradeep**, K. Kobiro, Single-step one-pot synthesis of metal oxide composite hollow assemblies, *IUPAC 11th International Conference on Novel Materials and their Synthesis*, Qinhuangdao, China, October **2015**.
8. M. Ohtani, **E. K. C. Pradeep**, K. Kobiro, Synthesis of novel spherical porous metal oxide composite nanoassemblies, *IUPAC 11th International Conference on Novel Materials and their Synthesis*, Qinhuangdao, China, October **2015**.
9. **E. K. C. Pradeep**, M. Ohtani, K. Kobiro, One-pot synthesis of hollow porous composite nanoassemblies based on binary metal oxides, *高知工科大学総合研究所 ナノテク研シンポジウム*, 11月, **2015**.

## Patent

1. 特願 2014-214856 号,  
メソポーラスナノ球状粒子製造方法,  
小廣和哉, 大谷政孝, エラワラ・カンカナムゲ・チャンディマ・プラディーブ.

## Awards

1. *Journal of Supercritical Fluids* “Editor-in-chief’s Featured Article” award, **E. K. C. Pradeep**, T. Habu, H. Tooriyama, M. Ohtani, K. Kobiro, Ultra-simple synthetic approach to the fabrication of CeO<sub>2</sub>–ZrO<sub>2</sub> mixed nanoparticles into homogeneous, domain, and core–shell structures in mesoporous spherical morphologies using supercritical alcohols, *J. Supercrit. Fluids* **2015**, 97, 217–223.
2. ポスター賞,  
**E. K. C. Pradeep**, M. Ohtani, K. Kobiro,  
One-pot synthesis of hollow porous composite nanoassemblies based on binary metal oxides, *高知工科大学総合研究所 ナノテク研シンポジウム*, 11月, **2015**.

## Miscellaneous

1. **E. K. C. Pradeep**, H. M. P. C. K. Herath, H. R. Perera, C. Li, D. P. Dissanayake, Comparison of polyaniline and polypyrrole based humidity sensors, *The 4th International Symposium on Frontier Technology*, Shenyang, China, August **2013**.
2. X. Li, **C. Pradeep**, D. Wang, T. Kawaharumura, N. Nitta, H. Furuta, A. Hatta, C. Li, Development of well-aligned ZnO nanorods as photo electrode for dye-sensitized solar cell application, *28th European Photovoltaic Solar Energy Conference and Exhibition*, Frankriech, France, October **2013**.
3. **E. K. C. Pradeep**, X. Li, T. Kawaharamura, D. Wang, A. Hatta, C. Li, Arrayed ZnO Nanorods Fabrication on ZnO Film by Self-catalyst Growth Method in Aqueous Solution, *MRS Online Proc. Libr.* **2014**, 1584, jsapmrs13-1584-6687.
4. C. Li, X. Li, **E. K. C. Pradeep**, T. Kawaharamura, ZnO thin film phosphor prepared on different substrates by novel multiple reducing annealing, *Dig. Tech. Pap.-Soc. Inf. Disp. Int. Symp.* **2014**, 45, 1305–1308.

## Acknowledgement

First, I am deeply indebted to my supervisor, Professor Kazuya Kobiro, not only for providing me the opportunity to carry on this research in the laboratory for Organic-inorganic hybrid materials chemistry, but also for his valuable help, suggestions, and comments during this research and writing this thesis. I would like to be thankful to the current and former members of “*Kobiro group*” including Assistant Professor Masataka Ohtani and Dr. Pengyu Wang for their kind help and guidance. Also, I would like to thank my co-supervisors; Professor Nagatoshi Nishiwaki, Professor Ryuichi Sugimoto, Professor Mamoru Furuta, and Professor Akimitsu Hatta for the guidance they provided.

Second, I would like to express my sincere gratitude to Professor Chaoyang Li and Associate Professor Hisao Makino for teaching of applied physics. Also, I am grateful to the faculty members of Institute of Nanotechnology; Associate Professor Toshiyuki Kawaharamura and lecturer Dr. Noriko Nitta, for their advices given for the nanomaterials characterization. Moreover, I would like to thank Emeritus Professor Laurence Hunter for teaching of English academic writing.

Third, I gratefully acknowledge Professor Shinichiro Sakikawa, the members of the international relation center, and Mr. Takashi Yoshida for their support not only in the University premises but also in our life at Tosayamada.

Specially, I would like to thank Special Scholarship Program (SSP) of Kochi University of Technology and Japan Student Services Organization (JASSO) for the scholarships I received for my doctoral studies.

Last, but not least I would like to appreciate the support, understanding, and the patience of my mother Mrs. Nandawathie, my father Mr. Abeypala, my sister Dr. Champika, and my loving wife Deshani.